

**ANALYSIS OF BACK-FEED CURVED REFLECTOR
ANTENNA USING RING FOCUS FEEDING**

Wanwisa Thaiwirot

**A Thesis Submitted in Partial Fulfillment of the Requirements for the
Degree of Doctor of Philosophy in Telecommunication Engineering**

Suranaree University of Technology

Academic Year 2011

การวิเคราะห์สายอากาศตัวสะท้อนแบบผิวโค้งด้านหลัง
โดยใช้การป้อนแบบโพกัสวงแหวน

นางสาววันวิสาข์ ไทยวิโรจน์

วิทยานิพนธ์นี้เป็นส่วนหนึ่งของการศึกษาตามหลักสูตรปริญญาวิศวกรรมศาสตรดุษฎีบัณฑิต
สาขาวิชาวิศวกรรมโทรคมนาคม
มหาวิทยาลัยเทคโนโลยีสุรนารี
ปีการศึกษา 2554

**ANALYSIS OF BACK-FEED CURVED REFLECTOR
ANTENNA USING RING FOCUS FEEDING**

Suranaree University of Technology has approved this thesis submitted in partial fulfillment of the requirements for the Degree of Doctor of Philosophy.

Thesis Examining Committee

(Asst. Prof. Dr. Peerapong Uthansakul)

Chairperson

(Assoc. Prof. Dr. Rangsan Wongsan)

Member (Thesis Advisor)

(Prof. Dr. Monai Krairiksh)

Member

(Assoc. Prof. Dr. Prayoot Akkaraekthalin)

Member

(Asst. Prof. Dr. Monthippa Uthansakul)

Member

(Prof. Dr. Sukit Limpijumnong)

Vice Rector for Academic Affairs

(Assoc. Prof. Dr. Vorapot Khompis)

Dean of Institute of Engineering

วันวิสาข ๒๕๖๓ : การวิเคราะห์สายอากาศตัวสะท้อนแบบผิวโค้งด้านหลัง
โดยใช้การป้อนแบบโฟกัสวงแหวน (ANALYSIS OF BACK-FEED CURVED
REFLECTOR ANTENNA USING RING FOCUS FEEDING) อาจารย์ที่ปรึกษา :
รองศาสตราจารย์ ดร.รังสรรค์ วงศ์สรรคค์, 169 หน้า.

ปัจจุบันเทคโนโลยีอวกาศและภูมิสารสนเทศได้เข้ามามีบทบาทสำคัญต่อการพัฒนา
ประเทศในหลาย ๆ ด้าน ทั้งทางตรงและทางอ้อม เช่น การสื่อสารข้อมูลผ่านดาวเทียม การศึกษา
ทางไกลผ่านดาวเทียม การสำรวจทรัพยากรธรรมชาติและพยากรณ์ภูมิอากาศ การพัฒนาทางด้าน
การแพทย์ การพัฒนาด้านเศรษฐกิจ รวมไปถึงการทดลองและทดสอบทางด้านวิทยาศาสตร์โดยนำ
อุปกรณ์การวัดติดตั้งบนตัวดาวเทียม เป็นต้น จึงทำให้สามารถนำมาใช้ในการเพิ่มขีดความสามารถ
ในการพัฒนาและแข่งขันกับประเทศคู่แข่งรวมทั้งประเทศเพื่อนบ้านได้ โดยดาวเทียมที่นิยมใช้ใน
เทคโนโลยีอวกาศในปัจจุบัน ได้แก่ ดาวเทียมวงโคจรค้างฟ้า (Geo-Stationary Orbit Satellite : GEO
Satellite) และดาวเทียมวงโคจรต่ำ (Low Earth Orbit Satellite : LEO Satellite) เป็นต้น เนื่องจาก
ดาวเทียมวงโคจรต่ำมีการเคลื่อนที่ด้วยความเร็วสูง จึงทำให้ระยะเวลาที่สถานีภาคพื้นดินติดต่อกับ
ดาวเทียมมีน้อยมาก ซึ่งสายอากาศที่นิยมใช้งานบนดาวเทียมวงโคจรต่ำโดยทั่วไปจะเป็นสายอากาศ
แบบตัวสะท้อนดัดรูป (shaped reflector antenna) อย่างไรก็ตามสายอากาศประเภทนี้มีข้อจำกัดคือ
กระบวนการในการหาสมการพื้นผิวของตัวสะท้อนมีความยุ่งยากซับซ้อน และพื้นผิวของ
ตัวสะท้อนที่สังเคราะห์ได้อาจจะมีความไม่ต่อเนื่องเกิดขึ้น ทำให้เกิดความยุ่งยากในการนำไปสร้าง
จริง ดังนั้นงานวิจัยนี้จึงได้นำเสนอการออกแบบสายอากาศตัวสะท้อนแบบผิวโค้งด้านหลังโดยใช้
การป้อนแบบโฟกัสวงแหวน โดยในส่วนของตัวสะท้อนหลักจะใช้สมการพื้นผิวแบบเรขาคณิตที่
สามารถสร้างได้ง่ายและใช้เทคนิคการกระเจิงคลื่นด้านหลังของตัวสะท้อน เพื่อทำให้เกิดความกว้าง
ลำคลื่นขนาดใหญ่ ซึ่งสามารถให้ลำคลื่นครอบคลุมกับพื้นโลก และยังสามารถเพิ่มระยะเวลาที่
สถานีภาคพื้นดินติดต่อกับดาวเทียมได้นานขึ้น นอกจากนี้สายอากาศดังกล่าวยังสามารถประยุกต์ใช้
งานกับการสื่อสารผ่านเครือข่ายท้องถิ่นแบบไร้สายได้ด้วย โดยวิธีการที่ใช้ในการวิเคราะห์คำนวณ
จะใช้การจำลองปัญหาสายอากาศด้วยทฤษฎีการเลี้ยวเบนเชิงกายภาพ (Physical Theory of
Diffraction : PTD) จากนั้นจะทำการสร้างสายอากาศต้นแบบ เพื่อนำไปวัดทดสอบคุณลักษณะ
เปรียบเทียบความแม่นยำตรงกับผลการจำลองผลที่ได้จากทฤษฎีการเลี้ยวเบนเชิงกายภาพต่อไป

สาขาวิชา วิศวกรรมโทรคมนาคม

ปีการศึกษา 2554

ลายมือชื่อนักศึกษา _____

ลายมือชื่ออาจารย์ที่ปรึกษา _____

ลายมือชื่ออาจารย์ที่ปรึกษาร่วม _____

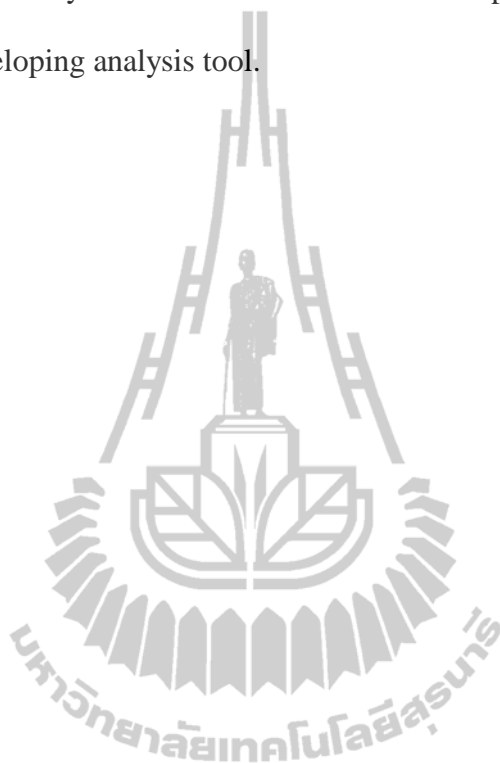
WANWISA THAIWIROT : ANALYSIS OF BACK-FEED CURVED
REFLECTOR ANTENNA USING RING FOCUS FEEDING.

THESIS ADVISOR : ASSOC. PROF. RANGSAN WONGSAN, D.Eng.,
169 PP.

PHYSICAL THEORY OF DIFFRACTION/BACK-FEED CURVED REFLECTOR
ANTENNA/RING FOCUS ANTENNA

Nowadays, space and geo-information technology and their applications have had a growing importance in many aspects of country development for both direct and indirect approaches such as satellite communication, distance learning via satellite, natural resource observation and climate forecasting, medical and economical development, demonstration and science experiments via satellite, etc. These can increase capability for development and to compete with the competitive countries and neighboring countries. The satellite has been widely used in space technology such as GEO satellite (Geo-Stationary Orbit Satellite) and LEO satellite (Low Earth Orbit Satellite). Since LEO satellite moves at a very high speed, therefore, the linkage time required for earth station-satellite communications is limited. It is well known that a shaped reflector antenna has been used in LEO satellite. However, shaping the reflector to the desired shaped-beam becomes complicated. This yields a discontinuous surface and more complicated manufacturing process. To overcome these limitations, this research proposes a back-feed curved reflector antenna using ring focus feeding. A backscattering technique is used with the main reflector to achieve broad-beamwidth for earth coverage. Moreover, this approach is fruitful for high-gain antenna applications, especially for Wireless Local Area Network (WLAN)

large-scale indoor base station. For analysis and design, a physical theory of diffraction (PTD) is utilized in this research. To validate the proposed concept, a back-feed curved reflector antenna using ring focus feeding will be designed based on the developed PTD analysis tool. The antenna will be implemented and experimented to validate the developing analysis tool.



School of Telecommunication Engineering Student's Signature _____

Academic Year 2011

Advisor's Signature _____

Co-advisor's Signature _____

ACKNOWLEDGEMENTS

I would like to thank the office of the higher education commission, Thailand for supporting by grant under the program strategic scholarships for frontier research network for the joint Ph.D. program Thai doctoral degree.

I am so grateful to my advisor, Assoc. Prof. Dr. Rangsan Wongsan, my co-advisor, Prof. Dr. Monai Kririksh and Prof. Dr. Makoto Ando for consistent thesis supervision and thoughtfully comment on several drafts and advice towards the completion of this study.

I would like to express my gratitude to the thesis examination committees, Asst. Prof. Dr. Peerapong Uthansakul, Assoc. Prof. Dr. Rangsan Wongsan, Prof. Dr. Monai Kririksh, Assoc. Prof. Dr. Prayoot Akkaraekthalin, Asst. Prof. Dr. Monthippa Uthansakul, for their invaluable advices and kind supports.

I would like to thank for the fellow members of the Wireless Communication Research and Laboratory, Suranaree University of Technology, for providing a pleasant and inspiring environment to work in.

Special thanks for the fellow members of the Ando and Hirokawa Laboratory, Tokyo Institute of Technology, Japan, for their best wishes and wonderful friendships throughout the research period.

Finally, I am greatly indebted to all of my teachers in the past and my family, who loves me and gives encouragement.

Wanwisa Thaiwirot

TABLE OF CONTENTS

	Page
ABSTRACT (THAI)	I
ABSTRACT (ENGLISH)	II
ACKNOWLEDGMENTS	IV
TABLE OF CONTENTS	V
LIST OF TABLES	X
LIST OF FIGURES	XI
CHAPTER	
I INTRODUCTION	1
1.1 Background of Problems and Significance of the Study	1
1.2 Research Objectives	4
1.3 Scope of the Study	5
1.4 Expected Benefits	5
1.5 Thesis Organization	5
II LITERATURE REVIEW	8
2.1 Introduction	8
2.2 Antenna for Wireless Communications	9
2.2.1 Reflector Antennas for Satellite Communications	9

TABLE OF CONTENTS (Continued)

	Page
2.2.2 Reflector Antennas for Indoor WLAN.....	13
2.3 Dual Reflector Antennas	14
2.4 Analysis Methods for Reflector Antenna.....	18
2.5 Chapter Summary.....	21
III BACKGROUND THEORY	22
3.1 Introduction	22
3.2 Physical Optics (PO).....	23
3.2.1 Equivalent Surface Currents.....	23
3.2.2 Scattering Field from Equivalent Surface Currents.....	27
3.3 Physical Theory of Diffraction (PTD).....	32
3.4 Radiation Characteristics of Antenna.....	36
3.4.1 Radiation Pattern	36
3.4.2 Beamwidth.....	36
3.4.3 Directivity.....	36
3.4.4 Antenna Efficiency.....	38
3.4.5 Gain	39
3.4.6 Polarization.....	40
3.5 Numerical Example for Reflector Antenna Analysis.....	41
3.6 Chapter Summary.....	56

TABLE OF CONTENTS (Continued)

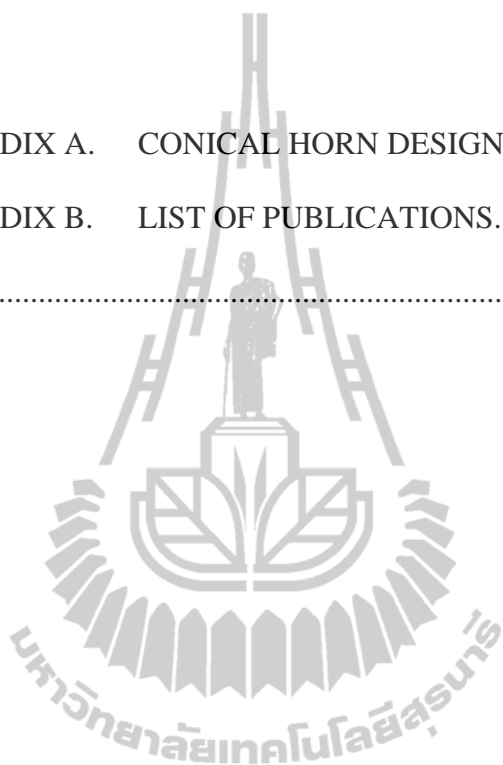
	Page
IV ANTENNA ANALYSIS AND DESIGN	58
4.1 Introduction	58
4.2 Conical (Corrugated) Horn Antenna	60
4.3 Axially Displaced Ellipse Reflector Antenna.....	66
4.4 Design Example of Axially Displaced Ellipse Reflector Antenna.....	67
4.5 Axially Displaced Ellipse Backscatter Antenna.....	79
4.5.1 Design of Axially Displaced Ellipse Backscatter Antenna.....	79
4.5.2 Calculation of Radiation Pattern by Using PO/PTD techniques.....	88
4.5.3 Analysis of Axially Displaced Ellipse Backscatter Antenna.....	91
4.5.4 Example of Axially Displaced Ellipse Backscatter Antenna when Input Parameters are Changed.....	104
4.5.5 Example of Axially Displaced Ellipse Backscatter Antenna when Equation of Main Reflector is Changed.....	109
4.6 Chapter Summary	112

TABLE OF CONTENTS (Continued)

	Page
V MEASUREMENT AND DISCUSSION	114
5.1 Introduction	114
5.2 ADE Backscatter Antenna Prototype.....	114
5.3 Antenna Measurement.....	117
5.3.1 Radiation Pattern	118
5.3.2 Gain	120
5.3.3 Bandwidth	121
5.3.4 Input Impedance, Standing Wave Ratio and Return Loss.....	122
5.4 Experimental Results.....	122
5.4.1 Conical Horn Antenna.....	122
5.4.2 ADE Backscatter Antenna.....	126
5.5 Chapter Summary.....	137
VI CONCLUSIONS	138
6.1 Thesis Concluding Remarks.....	138
6.2 Remark for Future Studies	139
REFERENCES	141

TABLE OF CONTENTS (Continued)

	Page
APPENDICES	
APPENDIX A. CONICAL HORN DESIGN	150
APPENDIX B. LIST OF PUBLICATIONS.....	166
BIOGRAPHY.....	169



LIST OF TABLES

Table	Page
3.1 Comparison of simulated and measured results for antenna characteristics.....	56
4.1 Eight cases where five input parameters are used	88
5.1 Dimensions of the ADE backscatter antenna.....	115
5.2 Measured characteristics for conical horn antenna.....	126
5.3 Comparison of simulated and measured results for antenna characteristics	137
A.1 Formulations for circular waveguide.....	151
A.2 Formulations for conical horn.....	152
A.3 Dimensions of the circular waveguide.....	155
A.4 Dimensions of the conical horn antenna.....	162

LIST OF FIGURES

Figure	Page
1.1 Back-feed curved reflector antenna for small LEO satellite application.....	2
1.2 Back-feed curved reflector antenna for WLAN large-scale indoor base station.....	3
1.3 Structure of a back-feed curved reflector antenna using ring focus feeding.....	4
2.1 The techniques to provide shaped beam.....	11
2.2 The shaped reflector surface discontinuity (Cherrette, 1989).....	12
2.3 Generalized classical axially symmetric dual reflector antennas (Fernando et al., 2001).....	15
3.1 Non-perfectly conducting surface.....	25
3.2 Equivalent currents radiating the scattered field.....	26
3.3 Three-dimensional geometry of a reflector ant its parameter.....	31
3.4 Reflector aperture and edge coordinate system.....	34
3.5 Wedge scattering geometry.....	35
3.6 Reflector antenna geometry and its prototype.....	42
3.7 Pyramidal horn and coordinate system.....	43
3.8 The sampling points in the x and y directions of feed aperture.....	46
3.9 Radiation pattern of standard X-band pyramidal horn.....	46

LIST OF FIGURES (Continued)

Figure	Page
3.10 PO/PTD for reflector antenna analysis	47
3.11 Analytical procedure for PTD	50
3.12 Far-field patterns of the quadratic reflector antenna by using PO/PTD	51
3.13 Close look at the rear pattern in E- and H-plane	52
3.14 Far-field patterns of the quadratic reflector antenna	54
4.1 Geometry of conical horn (Balanis, 2005)	61
4.2 Radiation pattern of corrugated conical horn	64
4.3 Radiation pattern of conical horn antenna	65
4.4 ADE reflector antenna geometry	67
4.5 A cross-section view of a the axially displaced ellipse antenna system	68
4.6 Cross-sectional view of the elliptical-subreflector coordinate system with its parameters	69
4.7 Distance relationship in an ellipse	69
4.8 The ADE antenna geometry, $D_m = 8$ m, $F = 4.7$ m, $L_m = 3.2506$ m, $D_s = 1.2$ m, $L_s = 2.1702$ m, $a = 1.554$ m, $f = 0.7843$ m, $\theta_e = 15^\circ$	73

LIST OF FIGURES (Continued)

Figure	Page
4.9 Radiation pattern of ADE reflector antenna compare with (Granet, 1999)	74
4.10 Geometry of front-feed single reflector antenna with $D_m = 8$ m and $F = 4.7$ m	75
4.11 Geometry of classical Cassegrain dual reflector antenna with $D_m = 8$ m, $D_s = 1.2$ m, and $F = 4.7$ m	75
4.12 Radiation pattern of front-feed single reflector antenna	76
4.13 Radiation pattern of classical Cassegrain dual reflector antenna.....	76
4.14 Radiation pattern of ADE reflector antenna.....	77
4.15 The ADE antenna geometry, $D_m = 70$ cm, $F = 18$ cm, $L_m = 12.1063$ cm, $D_s = 7$ cm, $L_s = 6.3625$ cm, $a = 4.9469$ cm, $f = 3.4273$ cm, $\theta_e = 25^\circ$	78
4.16 Photograph of the realized 70 cm diameter ADE antenna. Enlarged view of the subreflector is shown in the inset (Kumar et al., 2009)	78
4.17 Radiation pattern of ADE reflector antenna compare with (Kumar, 2009).....	79
4.18 A cross-section view of a the axially displaced ellipse backscatter antenna	81

LIST OF FIGURES (Continued)

Figure	Page
4.19 Cross-sectional view of the elliptical-subreflector coordinate system.....	81
4.20 PO/PTD techniques for ADE backscatter antenna.....	89
4.21 The ADE backscatter antenna geometry with set no.1 of input parameter: $D_m = 30$ cm, $D_s = 5.6$ cm, $A=8.2$ cm, $L=30$ cm, $a = 6.7370$ cm, $f = 1.4622$ cm, $L_s = 7.7293$ cm, $L_m = 37.3560$ cm, and $\theta_e = 25^\circ$	92
4.22 The subreflector surface and aperture coordinate	93
4.23 The current distributions over the subreflector surface at each radial samples for (a) plotting on xsr coordinate and (b) plotting on angle ϕ' in (degrees).....	94
4.24 The subreflector surface and sampling points on its aperture.....	95
4.25 The current distributions over the main reflector surface at each radial samples for (a) plotting on xmr coordinate and (b) plotting on angle ϕ' in (degrees).....	96
4.26 The fringe current along the edge of main reflector (solid line: Electrical equivalent fringe current, dashed line: magnetic equivalent fringe current	97

LIST OF FIGURES (Continued)

Figure	Page
4.27 Radiation pattern of ADE backscatter antenna by using PO-PTD	98
4.28 Radiation pattern of ADE backscatter antenna: comparison between PO-PO and PTD-PTD	99
4.29 Cross-polarized fields of ADE backscatter antenna: comparison between PO-PO and PTD-PTD	100
4.30 Radiation pattern of ADE backscatter antenna: comparison between PTD-PO and PTD-PTD	101
4.31 Cross-polarized fields of ADE backscatter antenna: comparison between PTD-PO and PTD-PTD	102
4.32 Radiation pattern of ADE backscatter antenna: comparison between PO-PTD and PTD-PTD	103
4.33 Cross-polarized fields of ADE backscatter antenna: comparison between PO-PTD and PTD-PTD	104
4.34 The ADE backscatter antenna geometry with set no.2 of input parameter: $D_m = 30$ cm, $A=8.2$ cm, $L_s=8$ cm, $L_m = 28$ cm, $D_s = 5.8487$ cm, $L = 28.9815$, $f = 1.5423$ cm, $a = 7.8017$ cm, and $\theta_e = 20^\circ$	106

LIST OF FIGURES (Continued)

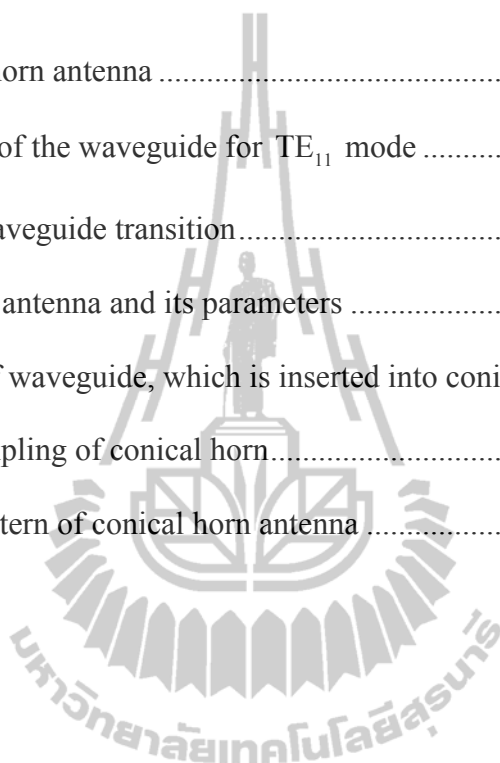
Figure	Page
4.35 Radiation pattern of ADE backscatter antenna when using set no.2 of input parameters.....	106
4.36 The ADE backscatter antenna geometry with set no.5 of input parameter: $D_s = 5.6$ cm, $L_s = 7.6$ cm, $L = 32$ cm, $A = 8.2$ cm, $L_m = 29.8284$ cm, $D_m = 38.6116$ cm, $f = 1.7717$ cm, $a = 6.8540$ cm, and $\theta_e = 20^\circ$	108
4.37 Radiation pattern of ADE backscatter antenna when using set no.5 of input parameters	108
4.38 The ADE quadratic backscatter antenna geometry with set no.1 of input parameters: $D_m = 30$ cm, $D_s = 5.6$ cm, $A = 5.8$ cm, $L = 30$ cm, $a = 6.7370$ cm, $f = 1.4622$ cm, $L_s = 7.7293$ cm, $L_m = 34.9560$ cm, and $\theta_e = 25^\circ$	111
4.39 Radiation pattern of ADE quadratic backscatter antenna when using set no.1 of input parameters	111
5.1 ADE backscatter antenna prototype.....	116
5.2 Near-field and far-field region of an antenna.....	117
5.3 Measurement set up of the radiation pattern	119
5.4 Measured return loss for the conical horn antenna	123
5.5 Measured impedance for the conical horn antenna.....	124

LIST OF FIGURES (Continued)

Figure	Page
5.6 Measured standing wave ratio for the conical horn antenna.....	124
5.7 Radiation pattern of conical horn antenna	125
5.8 Antenna prototype of the realized 30 cm diameter ADE antenna (a) subreflector is supported from the horn using stainless steel studs (b) subreflector is supported from the horn using cylindrical superlene cavity.....	127
5.9 Measured return loss for the ADE backscatter antenna (case 1).....	128
5.10 Measured impedance for the ADE backscatter antenna (case 1).....	128
5.11 Measured SWR for the ADE backscatter antenna (case 1).....	129
5.12 Co-polarized field patterns of a ADE backscatter antenna (case 1).....	130
5.13 Cross-polarized field patterns of a ADE backscatter antenna (case 1)	131
5.14 Measured return loss for the ADE backscatter antenna (case 2)	133
5.15 Measured impedance for the ADE backscatter antenna (case 2).....	133
5.16 Measured SWR for the ADE backscatter antenna (case 2).....	134
5.17 Co-polarized field patterns of a ADE backscatter antenna (case 2).....	135
5.18 Cross-polarized field patterns of a ADE backscatter antenna (case 2)	136

LIST OF FIGURES (Continued)

Figure	Page
A.1 The conical horn antenna	151
A.2 The exciting of the waveguide for TE_{11} mode	156
A.3 Coaxial to waveguide transition	156
A.4 Conical horn antenna and its parameters	157
A.5 The length of waveguide, which is inserted into conical horn.....	161
A.6 Aperture sampling of conical horn.....	164
A.7 Radiation pattern of conical horn antenna	165



CHAPTER I

INTRODUCTION

1.1 Background of Problems and Significance of the Study

Nowadays, space and geo-information technology and their applications have had a growing importance in many aspects of country development for both direct and indirect approaches such as satellite communication, distance learning via satellite, natural resource observation and climate forecasting, medical and economical development, demonstration and science experiments via satellite etc. These can increase capability for development and to compete with the competitive countries and neighbor countries. The satellite has been widely used in space technology such as GEO satellite (Geo-Stationary Orbit Satellite) and LEO satellite (Low Earth Orbit Satellite). Each of these has various strengths and weaknesses in its ability to provide particular communications services. For example, GEO systems have significantly greater available bandwidth than the LEO system. Because of their capacity and configuration, GEOs are often more cost-effective for carrying high-volume traffic, especially over long-term contract arrangements. GEO systems, like all other satellite systems, require line-of-sight communication paths between terrestrial antennas and the satellites. However, GEO systems have fewer satellites and these are in fixed locations over the earth. This is a significant disadvantage of GEO systems as compared to LEO systems, especially for mobile applications. The LEO systems are expected to cost less to implement than the other satellite systems. The LEO satellite communication systems are based on having multiple satellites orbiting in low earth

orbits. Since satellites in low earth orbit change their positions relative to the ground positions quickly, therefore, the linkage time requirement for ground station-satellite link is limited. Thus, to provide more time for ground station-satellite communication, an antenna on the satellite must have a wide beamwidth. The interested wide beamwidth antenna for small LEO satellite application in this research is shown in Figure 1.1.

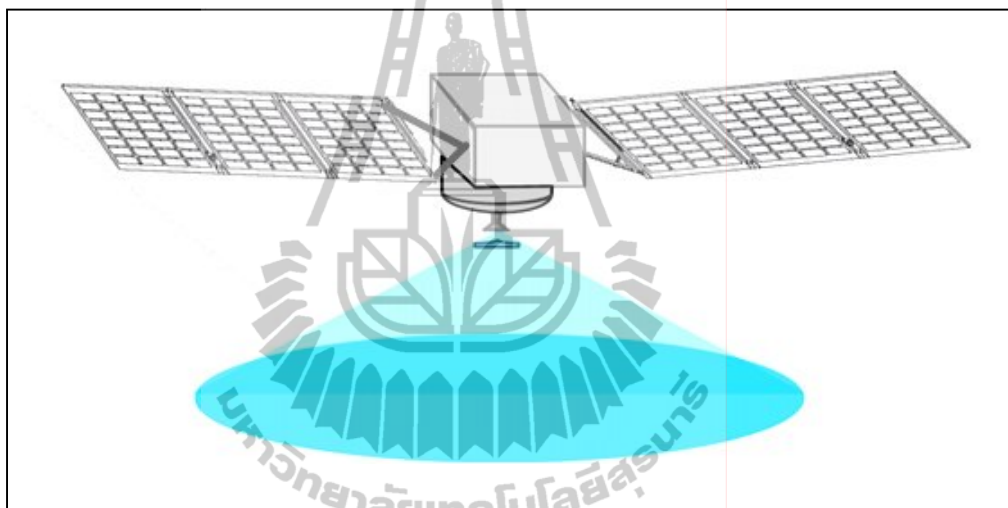


Figure 1.1 Back-fed curved reflector antenna for small LEO satellite application.

Moreover, this approach is fruitful for high-gain antenna applications, especially for wireless local area network (WLAN) large-scale indoor base station. The proposed antenna will be installed on the center point of ceiling in very large room and can illuminate a predefined circular coverage area. Consequently, the all client computers which are in this room will be connected to the access point of wireless LAN through the only one antenna as shown in Figure 1.2.

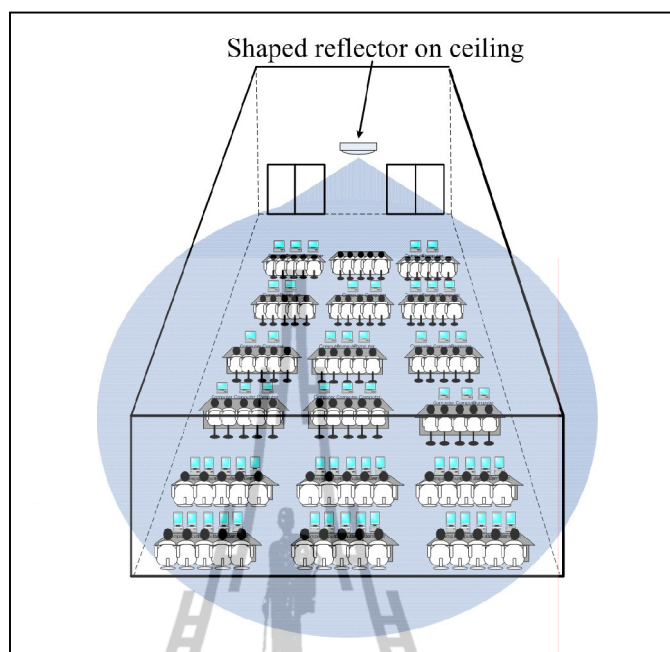


Figure 1.2 Back-feed curved reflector antenna for WLAN large-scale indoor base station.

This thesis concentrates on a back-feed curved reflector antenna using ring focus feeding. A backscattering technique is used with the main reflector to achieve wide beamwidth for earth coverage in LEO satellite. This antenna can be called the axis-displaced ellipse reflector antenna or ADE backscatter antenna, because subreflector of this antenna is a portion of an ellipse and it is displaced axis from main reflector. The structure of proposed antenna consists of a main reflector by using backscattering technique, a portion of an ellipse subreflector and a conical horn antenna as shown in Figure 1.3. For analysis, physical optics (PO) and a physical theory of diffraction (PTD) have been utilized in this research. To validate the proposed concept, a back-feed curved reflector antenna using ring focus feeding will be implemented and experimented at 18.75 GHz.

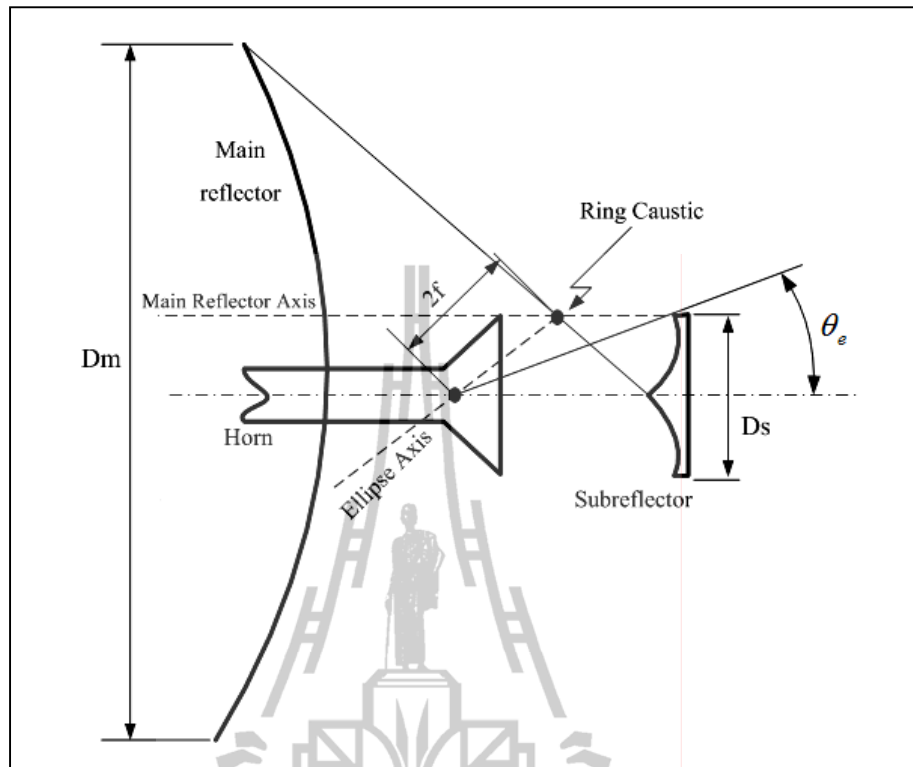


Figure 1.3 Structure of a back-feed curved reflector antenna using ring focus feeding.

1.2 Research Objectives

The objectives of this research are as follows:

1.2.1 To study the method to design and develop a reflector antenna for applying to small LEO satellite or WLAN large-scale indoor base station.

1.2.2 To validate the proposed concept, a back-feed curved reflector antenna using ring focus feeding will be designed based on the developed PO/PTD analysis tool.

1.2.3 To implement and experiment an antenna model to validate the developing analysis tool at 18.75 GHz.

1.3 Scope of the Study

The design of a back-feed curved reflector antenna using ring focus feeding or ADE backscatter antenna for applying to the small LEO satellite and WLAN large-scale indoor base station is presented. A simple procedure for the design of a back-feed curved reflector antenna using ring focus feeding is given. Using five input parameter parameters, a set of the equations is derived to find the remaining geometric parameters, fully defining the systems. The radiation fields of the proposed antenna are calculated by using physical optics (PO) and physical theory of diffraction (PTD). To verify the performance of the antenna discussed, a prototype has been fabricated at 18.75 GHz. This antenna is tested experimentally to validate the developing analysis tool.

1.4 Expected Benefits

1.4.1 To obtain a wide beamwidth of a back-feed curved reflector antenna using ring focus feeding for applying to the small LEO satellite or WLAN large-scale indoor base station.

1.4.2 To obtain the simulation program developed from PO/PTD which can be applied to use with the realized problem of a back-feed curved reflector antenna using ring focus feeding or axially displaced ellipse antenna (ADE antenna).

1.4.3 To obtain an antenna prototype at 18.75 GHz.

1.5 Thesis Organization

The remainder of this thesis is organized as follows. In chapter 2, we present a several types of the reflector antenna for applying to wireless communication system

such as antenna for satellite communication and indoor WLAN. In addition, a dual-reflector antenna and a generalized study of classical axially symmetric dual-reflector antenna are presented. Furthermore, an introduction to the high frequency diffraction techniques for reflector antenna analysis is presented in this chapter. The last section is chapter summary.

In chapter 3, we present the theory and formulation of the physical optics (PO) and physical theory of diffraction (PTD) techniques. The basic problems of physical optics method for analysis reflector antenna is obtaining the scattering fields produced by a source antenna, modeled as induce surface currents (source distribution) at every points on reflector surface (field surface). The currents induced on the reflector are obtained directly from the components of the incident fields tangential to the reflector at each point on its surface. These currents are then reradiated to be the far-field and produce the patterns. This process is illustrated in this chapter. However, the physical optics may not be accurately in the prediction of the radiated field in the far-angle regions, the cross-polarized field, or the near-field. The inaccuracy of the PO field can be effectively corrected by the PTD fringe fields. The approach of PTD is as follow (Michaeli, 1986); (Ufimtsev, 1991). The first step is calculation of the PO currents on the reflector surface and the fringe currents on the edge of reflector. The second step is calculation of the radiated fields due to the PO currents and the fringe fields due to the fringe currents. The total scattered field is constructed by adding a “fringe” field to the physical optics field. The PTD analytical procedure is given in this chapter. This chapter gives numerical example for reflector antenna analysis by using PO/PTD combination. In the last section of this chapter, the radiation characteristics and chapter summary will be presented.

In chapter 4, the ring focus antenna or axially displaced ellipse antenna (ADE antenna) is introduced. The antenna system consists of the main reflector, portion of an ellipse subreflector and horn antenna. The features and advantages of the ring focus antenna are described in this section. The design examples of ADE reflector antenna based on Granet (1999) will be presented. In order to justify the validity of the analysis tool, this analysis is compared with Granet (1999) and Kumar et al. (1999). In addition, the design procedure for back-feed curved reflector antenna by using ring focus feeding or ADE backscatter antenna is presented. The several sets of input parameters of the proposed antenna for representing the ADE backscatter antenna are derived in closed form. The radiation fields of the ADE backscatter antenna are simulated by using PO/PTD techniques and then compared with the back-feed curved single reflector antenna. The last section is chapter summary.

To verify the performance of the proposed antenna discussed, a prototype has been designed and developed, which are given in chapter 5 and the manufacturing process is described. Furthermore, the experimental process was carried out, followed by a completed description of the results obtained in the anechoic chamber. Performance comparison between the simulated and measured results is also conducted.

The last chapter, chapter 6, provides conclusions of the research work and suggestion for future studies.

CHAPTER II

LITERATURE REVIEW

2.1 Introduction

Classical axially symmetry Cassegrain and Gregorian reflectors have been used for many years in high gain antenna applications (Hannan, 1961); (Rusch, 1963). The main disadvantage of these configurations is the blockage of the main reflector by the feed/subreflector and its support structure, which causes a number of deleterious effects such as the decrease of the antenna aperture efficiency. However, this problem can be minimized by reducing the main-reflector radiation toward the subreflector. This may be accomplished by either shaping both reflector or using alternative classical configurations, where the generating curve of the axially symmetric reflectors are described by conic section (Yerukhimovich and Miroshinichenko, 1975); (Rotman and Lee, 1984). In this thesis, the second option has been considered by focusing on axially symmetric dual reflector antenna. The comparison of these antenna geometries has been studied by the authors during the last nine years (Moreira and Prata, 2001). It has been found that the axially displaced ellipse (ADE) reflector antenna provides an excellent choice for compact high gain spacecraft antenna applications. Moreover, the ADE configuration, without any shaping of the reflectors, can provide high efficiency using a feed of low to moderate gain. The main aim of this thesis is the design and developing a wide beamwidth back-feed curved reflector antenna using ring focus feeding for applying to small LEO satellite or WLAN large-scale indoor base station. However, the proposed antenna is based on axially

displaced ellipse reflector antenna studied by Popov and Milligan (1997) and Granet (1999) but our main reflector shape is different. The backscattering technique is used with the main reflector achieving wide beamwidth for earth coverage in LEO satellite application.

In this chapter, we will present several types of the reflector antenna for applying to the satellite communication and indoor WLAN. In addition, a dual-reflector antenna and a generalized study of classical axially symmetric dual-reflector antenna are presented. Furthermore, an introduction to the high frequency diffraction techniques for reflector antenna analysis is presented. The last section is chapter summary.

2.2 Antenna for Wireless Communications

2.2.1 Reflector Antennas for Satellite Communications

A variety of antenna types are used in satellite communications. Shaped beam reflector antenna has become key element of communication satellites having requirement of irregular shaped coverage area. The shaped beam can be generated mainly by three techniques viz. direct radiating planar array with beam forming network (Cherrette and Chang, 1985), array fed with parabolic reflector antenna (Rush, 1984) and shaped reflector antenna as shown in Figure 2.1. First two techniques have more RF loss in beam forming network. The shaped reflector antennas are interested because of the fact that only one horn feeding a single shaped reflector can produce a shaped beam. Since the shaped reflector antenna requires no feed network, the expense, weight and RF losses of the antenna system are reduced. Also, elimination of the feed network will simplify construction of the antenna. The

example of shaped reflector antennas for satellite communication such as Cherrette (1989) research presented a method for producing a shaped contour radiation pattern using a single reflector and a single feed. In this case, the far-field radiation pattern is configured to the desired shape by properly shaping the reflector surface. The synthesis method procedure for producing a shaped contour radiation pattern will be started by the phase distribution in the near field aperture plane, which is first optimized with a set of constraint gains in the far-field and then the reflector is shaped according to the optimized phase distribution. However, the major problems from this method are the surface discontinuities that can be generated and the lack of control in edge shape as illustrated in Figure 2.2. Later, Shogen, Nishida, and Toyama (1992) presented shaped reflector for broadcasting satellites. Authors improved the phase optimization method proposed in Cherrette (1989), so that the problem of the discontinuity on the reflector surface is avoided. However, a drawback in this method for phase optimization is the computation time. Chen and Chuang (1997) presented a shaped offset reflector antenna synthesizing a contoured beam and an elliptical offset reflector antenna to generate an elliptical beam in order to cover the Taiwan island region. They compared and discussed of the antenna coverage performance of the two designs. In the case of shaped reflector antenna, the reflector shaping technique of their research was based on Cherrette (1989); Shogen et al. (1992). It was found that shaped reflector antenna to provide the contoured beam can reduce gain level in the unnecessary antenna radiation power over undesired nearby region. While for the elliptical reflector antenna (unshaped reflector), the elliptical beam can achieve the desired Taiwan region coverage requirement.

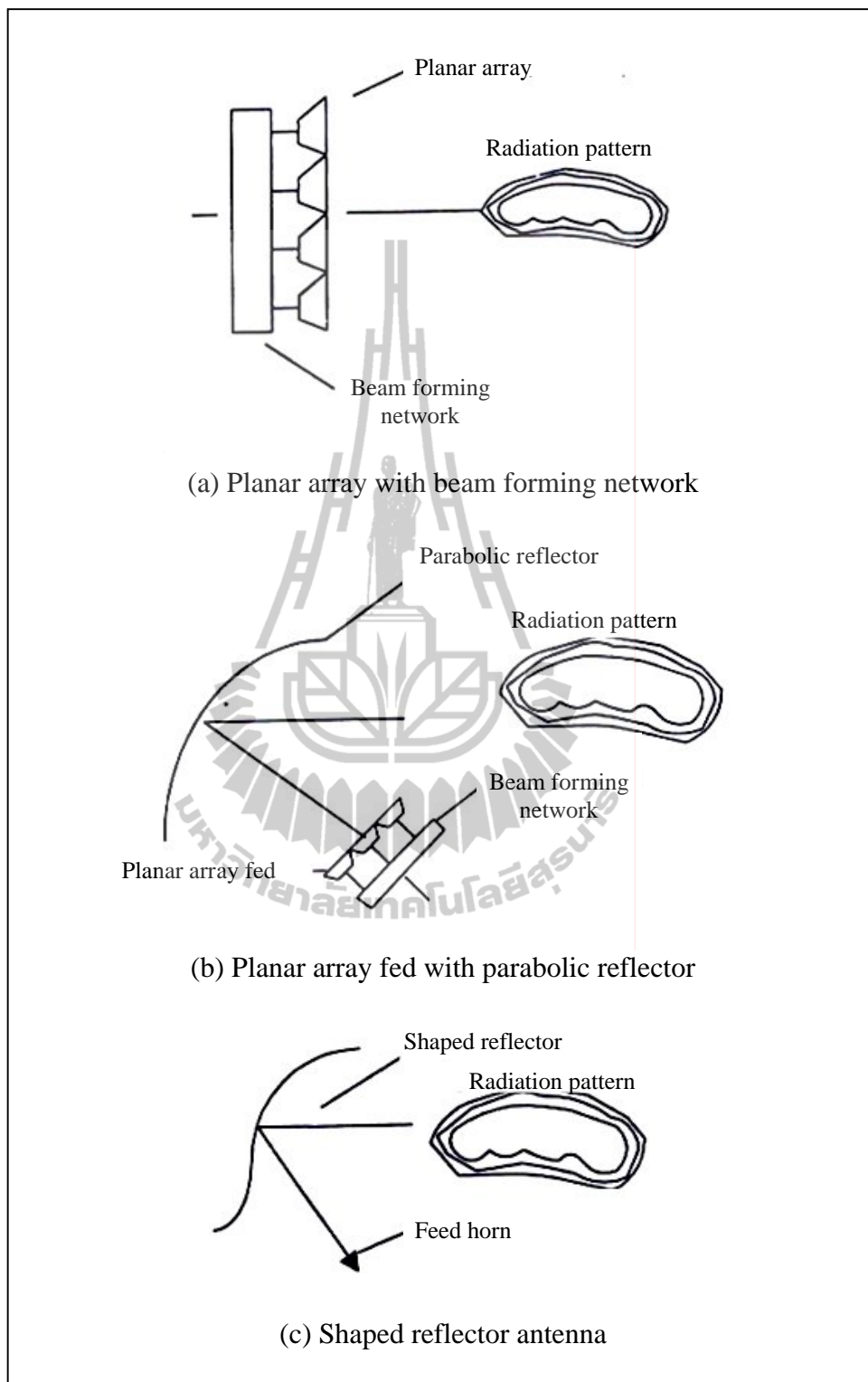


Figure 2.1 The techniques to provide shaped beam.

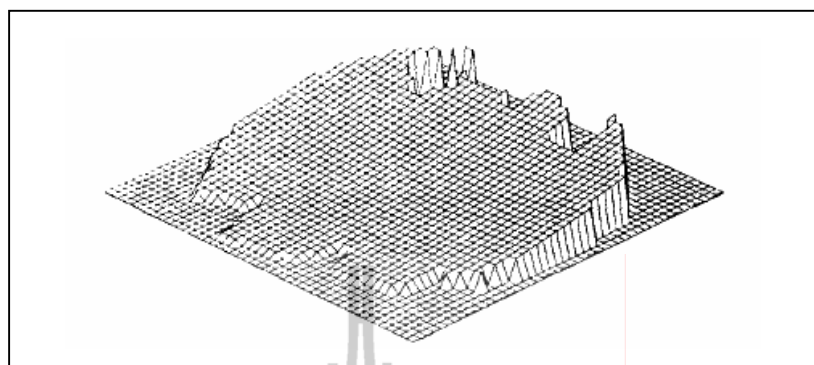


Figure 2.2 The shaped reflector surface discontinuity (Cherrette, 1989).

The shaped contour radiation patterns, as described above, are obtained by using a single feed with a shaped main reflector. The main reflector surface is shaped to produce a desired radiation pattern. A primary disadvantage associated with shaped reflectors such as the position of feed and the shape of reflector, which are designed for a given fixed radiation pattern to cover only desired region. Changing the shaped contour radiation patterns, the shape of reflector surface is needed to be changed. Moreover, shaping the reflector to obtain desired shaped beam, the construction of the surface is more complex and this yields more complicated manufacturing. If the shape of the desired coverage region is very close to an elliptical or circular zone, then the reflector antennas providing elliptical or circular beam will be alternative choice for satellite communication. Furthermore, if we can synthesize a variety of reflector shapes for variety of different coverage region, it will be convenient to choose these reflectors for using in varied region. Thavivrot et al. (2008) presented the synthesis of radiation pattern of variety of the shape backscatter antennas viz. triangular, quadratic, circular, Gaussian, cosine, squared cosine, parabolic, and hyperbolic shape for wide variety of different coverage area. Each of shape single backscatter antenna

is easy to realize and manufacture because the shape of backscatters are elementary geometrical functions. Moreover, these single backscatter antennas can provide wide beamwidth for applying to small LEO satellite and WLAN large-scale indoor base station.

2.2.2 Reflector Antennas for Indoor WLAN

The highly shaped-beam antenna was first developed to give approximately uniform coverage of the earth from satellite antenna (Kishk, 1989); (Hay et al., 1999); (Olver, 1994). Recently, the similar requirement but different application that is, the indoor high speed data transmission: wireless LAN operating in the millimeter wave, again attracts considerable attentions (Bird et al., 1994); Smulders et al., 2001); (Kumar, 2003). Due to the critical specification in link budget, the transmitted power has to be efficiently distributed over the coverage; the spatial fluctuation of the field strength has to be as small as possible within the defined coverage area, whereas outside the coverage the field strength has to fall off rapidly. A shaped reflector antenna for 60-GHz indoor wireless LAN access point was developed (Smulders, 2001). A circular footprint having the deviation from the average field strength less than 2.5 dB in the far-field was reported (Smulders, 2001). They commented that the practical imperfections such as axial and lateral feed displacement and mispointing of the feed on top of effects due to blockage by the feed-horn may contribute to spatial field variations. Moreover, compact shaped reflector antennas comprise an interesting alternative to usual base station arrays due to their ability in providing customized coverage pattern (Bergmann et al., 1998); (Bergmann et al., 2002). However, the synthesis the shaped reflector antenna to obtain shaped beam for service coverage in WLAN application may yield the

construction of the surface more complex. This provides complicated manufacturing and increase the fabrication cost. This research interests the reflector antenna by using backscattering technique to achieve the completely wide beam radiation pattern for service coverage. The shape of the reflector must be convenient to realize and manufacture.

2.3 Dual Reflector Antennas

Axially symmetrical dual reflector antennas such as Cassegrain and Gregorian, reflectors are of interest in radio astronomy and in earth station antenna technology. However, the main disadvantage of these configurations is the subreflector blockage, which causes a number of deleterious effects such as the decrease of the antenna aperture efficiency. However, this problem can be minimized by reducing the main-reflector radiation toward the subreflector. This may be accomplished by either shaping both reflector or using alternative classical configurations, where the generating curves of the axially symmetric reflectors are described by conic section (Yerukhimovich and Miroschinchenko, 1975); (Rotman and Lee, 1984). In this thesis, the second option is considered by focusing on an axially displaced dual reflector antenna. There are four different types of classical axially symmetric dual reflector antennas that avoid field scattering from the main reflector scattering toward the subreflector (Moreira and Prata, 2001). Their generating curves and relevant parameters are expressed in Figure 2.3. The four classical configurations are basically characterized by the location of the two subreflector caustic regions. One caustic (a ring caustic) is located by the rotation of the parabolic focal point around the symmetry axis. The second caustic (a line

caustic) corresponds to the portion of the symmetry axis intersected by subreflector reflected rays. The first geometry has a virtual ring and line caustics classified here are an axially displaced Cassegrain (ADC). This geometry was previously studied in Yerukhimovich (1972) and named an axially tilted hyperbola (ATH). The second geometry has real ring and line caustics defined as an axially displaced Gregorian (ADG). The third geometry has real ring caustic and a virtual line caustic named an axially displaced ellipse (ADE) section (Yerukhimovich and Miroshinichenko, 1975); (Rotman and Lee, 1984). It was previously studied in Yerukhimovich (1972) under the denomination axially tilted ellipse (ATE) and is also known as the Yerukhimovichian configuration. Finally, the last configuration has a virtual ring caustic and real line caustic denominated axially displaced hyperbola (ADH). In all these configurations, the main reflector is generated by a parabola, while the curve of subreflector generated can be either a hyperbola (ADC and ADH) or an ellipse (ADG and ADE).

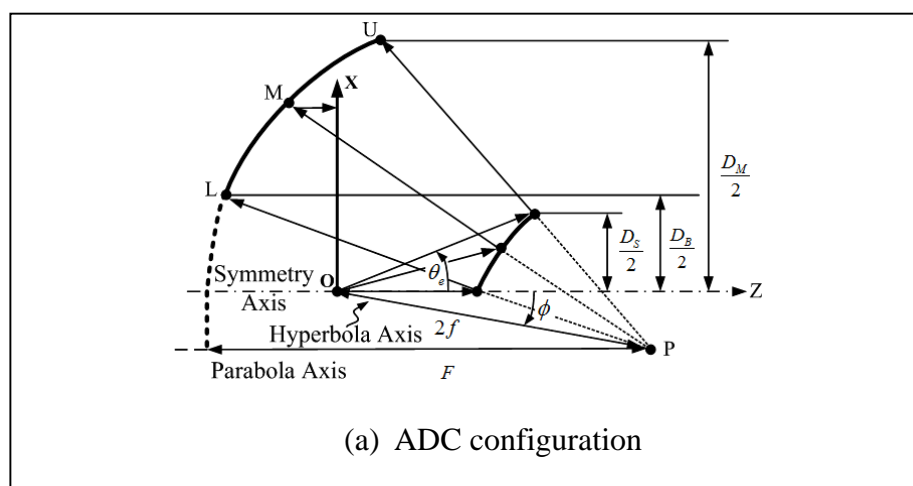


Figure 2.3 Generalized classical axially symmetric dual reflector antennas

(Fernando et al., 2001).

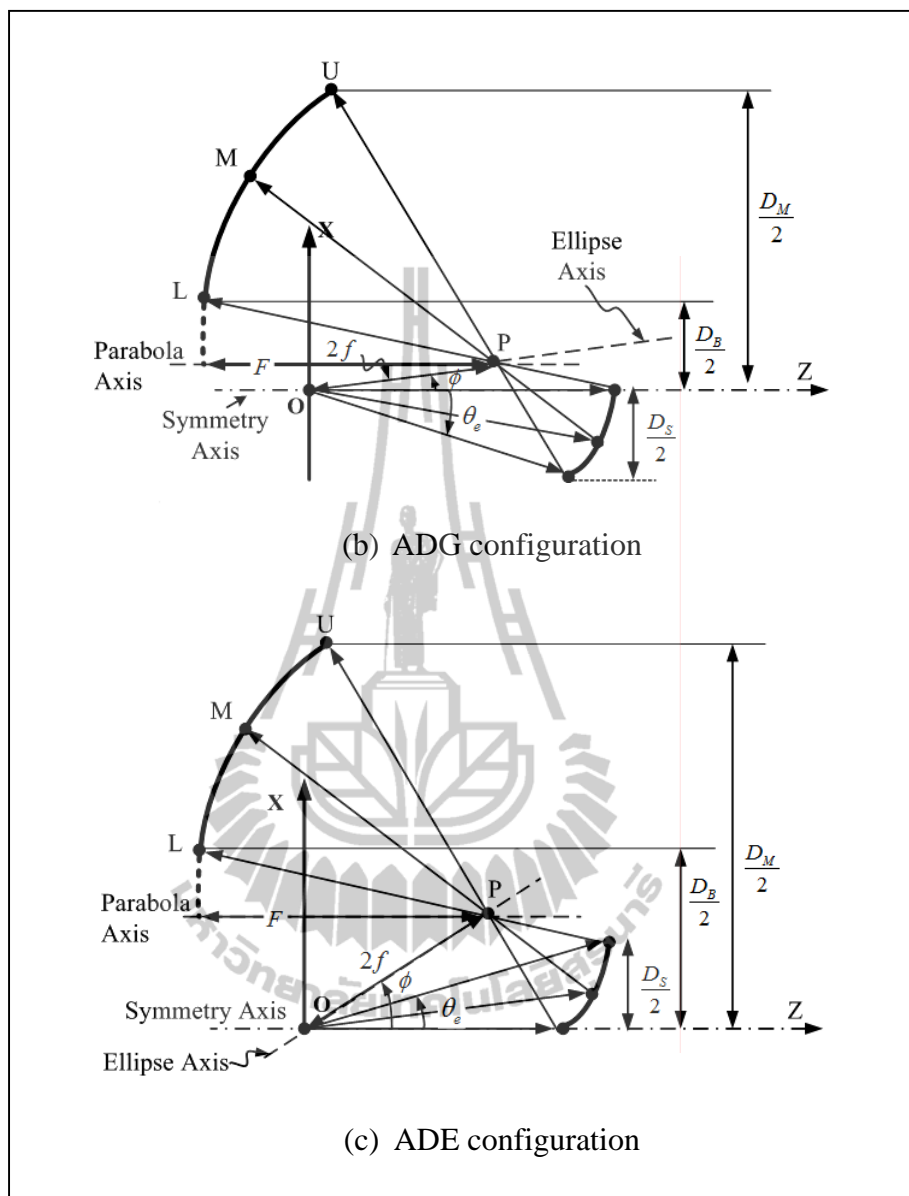


Figure 2.3 Generalized classical axially symmetric dual reflector antennas

(Fernando et al., 2001) (Continued).

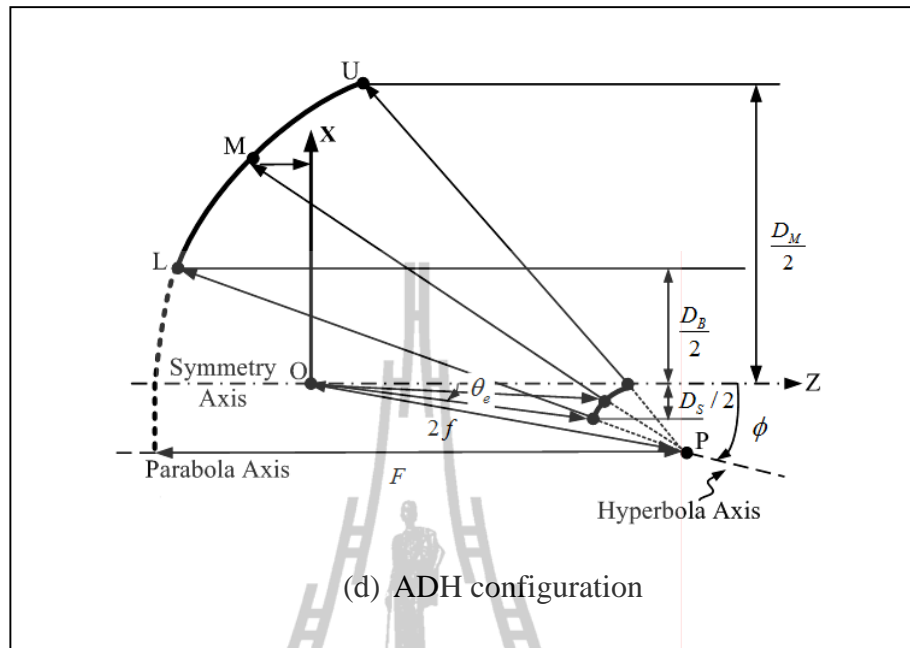


Figure 2.3 Generalized classical axially symmetric dual reflector antennas
(Fernando et al., 2001) (Continued).

Later, Moreira and Prata (2001) regard the dual reflector antenna blockage effects. For the dual reflector antenna geometries as shown in Figure 2.3, three blockage mechanisms such as subreflector, feed and self blockages are presented. The subreflector blockage is characterized by the incidence of main reflector reflected rays upon the subreflector. It is avoided when $D_s \leq D_B < D_M$ (see Figure 2.3). The feed blockage occurs when part of the subreflector reflected rays impinges upon the feed structure, depending on the feed physical dimensions. If assuming a feed illumination provided by point source, the feed blockage never occurs for the ADC and ADE. The self blockage refers to the intersection of rays reflected by the subreflector lower (upper) half with the subreflector upper (lower) half surface, which can only occur for the ADG and ADH configuration. The study of Moreira and

Prata (2001) found that, the ADC and ADG can provide, without considering any diffraction effects, efficiency up to 84%, while the ADE and ADH can yield efficiency beyond 90% by decreasing feed spillovers and relatively smaller subreflector diameters. In addition, Moreira and Bergmann (2005) studied the synthesis and performance of classical dual-reflector antennas suited for an omnidirectional coverage. The study was found that the omnidirectional ADE configuration provides the most compact arrangements and capable of yielding the high efficient antennas. Latterly, Granet (1999) presented a simple procedure for the design of classical displaced axis dual reflector antennas. Author used four input parameters, a set of equations is derived to find the remaining geometric parameters and fully defining the system. This initial geometry provides a good starting point for any optimization process. Recently, Kumar et al. (2009) reported the performance of the ADE antenna with an electrically small aperture. The diameter of the antenna is about 20λ , which is considerably smaller than the ADE antennas already reported. Their antenna design has been successfully implemented in India's first mission to the moon, Chandrayann-1. The results of this research provide the confidence for using the ADE configuration on small aperture and high efficiency antenna application.

2.4 Analysis Methods for Reflector Antenna

In order to design and correctly predict the performance of a reflector antenna, different analysis and synthesis techniques have been developed (Samii, 1993); (Samii, 1995). Physical optics (PO) is one of widely used techniques to analytically determine the radiation patterns of reflector antennas. It is popular because of its simplicity in algorithm, its ability to accurately predict the far field pattern near the

main beam, and the availability efficient numerical techniques to perform the surface integration (Samii, 1988). However, PO may be not accurate in the prediction of the radiated field in the far-angle regions, the cross polarized field, or the near field. It may therefore be necessary to use other techniques to accurately compute these quantities.

One of the techniques that can be used to accurately predict the fields in far angle regions is Geometrical Theory of Diffraction (GTD) originated by Keller (1952). This simple and accurate algorithm has been further enhanced by the development of the Uniform Geometrical Theory of Diffraction (UTD) (Kouyoumjian and Pathak, 1974) and the Uniform Asymptotic Theory (UAT) (Ahluwalia et al, 1968); (Lee and Deschamps, 1976), which remedy the deficiencies of GTD at the shadow boundary and the reflection boundary. However, the caustic singularity of GTD, which causes difficulty in the antenna directivity calculation, cannot be removed by the uniform versions. If one uses GTD and PO jointly to overcome this limitation in the reflector analysis, it is usually difficult to determine an observation angle at which a changeover between these two methods should take place. Furthermore, when applied to scatterers with curved surfaces and edges, the computation efficiency of the GTD techniques degrades if the reflection and diffraction points on the scatterers were determined numerically. Due to these facts, it is desirable to have a diffraction technique by which both of the co-polarized and the cross-polarized fields can be predicted accurately and uniformly over the whole angular regions.

Another technique developed at same time as GTD is the physical theory of diffraction (PTD) pioneered by Umfimtsev (1962). Two important modifications to the original PTD have been achieved. The first one is the application of the concept of equivalent edge current (EEC), which eliminates the caustic singularities in the original ray tracing PTD. The second one is an extension for observation angles, which are not on the positions of angle of Keller's cone. Ando's modified PTD is one modification that uses the concept of EEC (Ando, 1985). A theoretical examination of this method can be found in Breinbjerg et al. (1987). Mitzner, on the other hand, did not use EEC explicitly but rather expressed the PTD correction fields in terms of incremental length diffraction coefficients (ILDC) (Mitzner, 1974). The third modified PTD will be studied in this thesis is Michaeli's work. He derived the GTD equivalent edge currents by asymptotically reducing the surface to edge integral (Michaeli, 1984). These currents were then written in terms of diffraction coefficients. It has been pointed out in (Knott, 1985) that if the PO components are subtracted from Michaeli's total scattered field, then the fringe fields constructed by Mitzner's ILDC are recovered. The equivalence of the total scattered field to the sum of the PO and fringe fields has also been observed in the spectral domain (Samii and Mittra, 1977). Later, Michaeli evaluated the fringe current radiation integral over the "ray coordinate" instead of over the "normal coordinate". This improvement using such techniques corrected many of the singularities in Mitzner's ILDC (Michaeli, 1986).

2.5 Chapter Summary

This chapter gives a detail and literature surveys of the reflector antenna for wireless communication such as WLAN and satellite communication. It was found

that the single shaped reflector to provide shaped beam has been interested for satellite communication. However, the synthesis of the shaped reflector antenna to obtain shaped beam for service coverage may yields the construction of the surface is more complex. This provides complicated manufacturing and increase the fabrication cost. Therefore, if the shape of the desired coverage region is very close to an elliptical or circular zone, then the shape of reflector antennas providing elliptical or circular beam and easy to realize and manufacture are alternative choice for satellite communication. In order to improve efficiency of the antenna, the dual reflector antennas avoiding the subreflector blockage are studied. The study was found that the ADE configuration provides the compact antenna and yielding the high efficient antenna by avoiding subreflector blockage. In addition, the literature survey of analysis method for reflector antenna was presented in the last section. This thesis focuses on the PTD technique studied by Michaeli for reflector antenna analysis. The formulations and the numerical example of reflector antenna analysis by using PO and PTD method will be detailed in following chapter.

CHAPTER III

BACKGROUND THEORY

3.1 Introduction

Efficient and accurate high frequency diffraction analysis techniques for reflector antenna have been interested for many years. Physical Optics (PO) is one of the techniques that has been widely used in analytical determination of the radiation patterns of reflector antennas. It is popular because of its simplicity in the algorithm, able to accurately predict the far-field pattern near the main beam and can use efficient numerical techniques to perform the surface integration (Samii, 1988; Ando, 2005). However, physical optics may not be accurate in the prediction of the radiated field in the far-angle regions, the cross polarized field, or the near-field. Therefore, it may be necessary to use other techniques to accurately compute these quantities as described in chapter 2. To overcome these limitations, the Physical Theory of Diffraction (PTD) technique studied by Michaeli is presented in this chapter. For Michaeli's method, the total scattered field is constructed by adding the fringe field to the physical optics field. In this chapter, the formulations of the PO and PTD techniques and radiation characteristics of antenna are presented in sections 3.2 to 3.4. The numerical example for reflector antenna analysis will be presented in section 3.5 to demonstrate the effectiveness of the PTD fringe field in improving the PO field.

3.2 Physical Optics (PO)

Physical optics is a simple method that gives an approximation to the surface currents valid for perfectly conducting scatterers, which are large in terms of wavelengths. The scattered fields are calculated by either finding the induced equivalent currents on the scatterer surface and these currents are then reradiated to the far-field to produce the patterns. To calculate the radiated fields due to the equivalent surface currents involve no further approximations since the radiation integral of the surface currents can be computed by numerical integration with high precision. If the surfaces of the scatterer are not perfectly conducting, but reflection and transmission coefficients are known, the physical optics method can be modified to give an approximation to the equivalent electric and magnetic surface currents.

3.2.1 Equivalent Surface Currents

In the physical optics approximation, it is assumed that the surface current in a specific point on a curve, but perfectly conducting scatterer is the same as the surface current on an infinite planar surface, which is tangential to the scattering surface at this point. The equivalent currents on a perfectly electric conducting (PEC) infinite plane surface illuminated by an arbitrary incoming field are given by the well-known formula (Collin and Zucker, 1969)

$$\bar{J} \approx \bar{J}^{PO} = \begin{cases} 2\hat{n} \times \bar{H}^i, & \text{Illumination region} \\ 0 & \text{, Shadow region} \end{cases}, \quad (3.1)$$

which constitutes the physical optics approximation. Here \bar{J} is the equivalent electric current, \hat{n} is the unit surface normal vector (pointing outward on the illuminated side

of the surface) and \vec{H}^i is the incident magnetic field. At points on the scatterer which, are not directly illuminated by the incident field, the surface currents are approximated with zero.

The equation (3.1) is simple to derive for an incident plane wave but it is valid for any kind of incident field as explained below. A curved surface is a good approximation to the actual current if the dimensions of the scattering surface and its radius of curvature are sufficiently large measured in wavelengths. For simple surface shapes, physical optics is often used for scatterers down to five wavelengths in diameter.

In order to show that (3.1) is valid for a general incident field, we consider two plane waves with different amplitudes and direction of propagation incident on an infinite planar surface. They will induce the currents \vec{J}_1 and \vec{J}_2 , respectively, given by

$$\vec{J}_1 = 2\hat{n} \times \vec{H}_1^i \quad (3.2a)$$

$$\vec{J}_2 = 2\hat{n} \times \vec{H}_2^i, \quad (3.2b)$$

where \vec{H}_1^i and \vec{H}_2^i are the magnetic fields of two incident plane waves. The total surface current is found by adding the two equations in (3.2a) and (3.2b) which gives

$$\vec{J} = \vec{J}_1 + \vec{J}_2 = 2\hat{n} \times (\vec{H}_1^i + \vec{H}_2^i) = 2\hat{n} \times \vec{H}^i, \quad (3.3)$$

where \vec{H}^i is now the total incident field. It is seen that this equation has the same form of (3.1). An incident field consisting of an arbitrary number of incident plane

waves can be treated in the same way, which shows that (3.1) is valid for a general incident field.

If the scattering surface is not perfectly conducting, but the reflection and transmission coefficients are known, a method that is similar to physical optics can be used to compute a set of equivalent electric and magnetic currents, which approximates the exact equivalent currents radiating the scattered field. For derivation of this approximation, we consider that an infinite planar surface has finite thickness with known incident field and reflection and transmission coefficients as shown in Figure 3.1. The incident, reflected and transmitted electric and magnetic fields are marked by superscripts i , r and t , respectively.

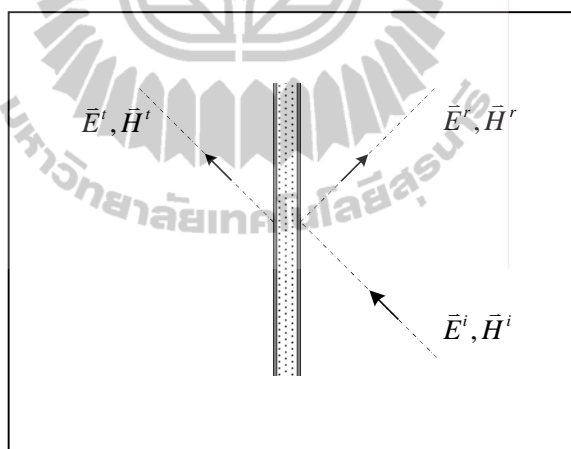


Figure 3.1 Non-perfectly conducting surface.

If the incident field is subtracted from the fields on both sides of the surface the equivalence principle may be applied so that the surface can be replaced by two current sheets as shown in Figure 3.2.

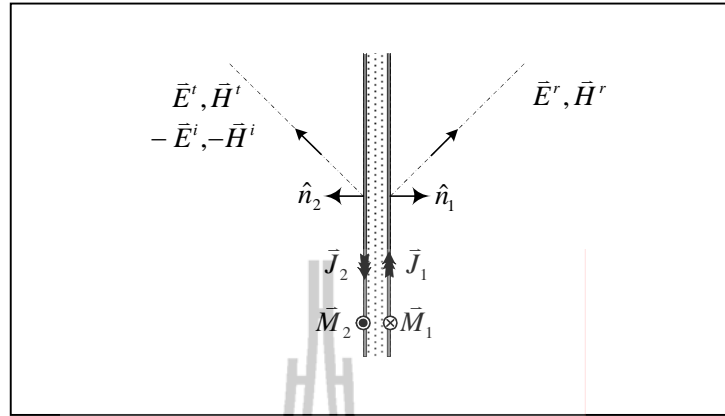


Figure 3.2 Equivalent currents radiating the scattered field.

From the reflection and transmission coefficients, the reflected and transmitted fields can be computed and then equivalent currents can be found from the electromagnetic boundary conditions, which give

$$\bar{J}_1 = \hat{n}_1 \times \bar{H}^r, \quad \bar{M}_1 = -\hat{n}_1 \times \bar{E}^r \quad (3.4a)$$

$$\bar{J}_2 = \hat{n}_2 \times (\bar{H}^t - \bar{H}^i), \quad \bar{M}_2 = -\hat{n}_2 \times (\bar{E}^t - \bar{E}^i), \quad (3.4b)$$

where \bar{J}_1 and \bar{J}_2 denote electric currents in media 1 and 2, respectively,

\bar{M}_1 and \bar{M}_2 denote magnetic currents in media 1 and 2, respectively,

\hat{n}_1 and \hat{n}_2 denote the unit surface normal vector in media 1 and 2, respectively.

Due to the plane wave assumption, the phase of the transmitted field may be referred to the front surface such that only one sheet of equivalent currents is needed. Using $\hat{n}_2 = -\hat{n}_1$, we obtain

$$\vec{J} = \vec{J}_1 + \vec{J}_2 = \hat{n}_1 \times (\vec{H}^i + \vec{H}^r - \vec{H}^t), \quad (3.5a)$$

$$\vec{M} = \vec{M}_1 + \vec{M}_2 = -\hat{n}_1 \times (\vec{E}^i + \vec{E}^r - \vec{E}^t). \quad (3.5b)$$

When the scattering surface is curved and of finite extent the currents (3.5) are an approximation to the exact equivalent currents. For perfectly conducting surface, the transmitted field is zero and the tangential components of the incident and reflected field are either equal (H-field) or opposite (E-field) such that \vec{J} in (3.5a) reduces to (3.1) and \vec{M} becomes zero. An important complication for the non-perfectly conducting surface is that the reflection and transmission coefficients usually depends on the angle of incidence, which means that it is necessary to know the direction of propagation of the incident field. This direction is only well-defined if the incident field is locally a plane wave. As explained above this restriction is not necessary for the physical optics approximation (3.1) on a perfectly conducting surface.

3.2.2 Scattering Field from Equivalent Surface Currents

According to Collin and Zucker (1969) the radiated field from a set of equivalent surface currents can be computed from

$$\vec{A} = \frac{\mu}{4\pi} \iint_S \vec{J}(\vec{r}') \frac{e^{-jkR}}{R} ds', \quad (3.6a)$$

$$\vec{F} = \frac{\varepsilon}{4\pi} \iint_S \vec{M}(\vec{r}') \frac{e^{-jkR}}{R} ds', \quad (3.6b)$$

$$\vec{E} = -j\omega \left(\vec{A} + \frac{1}{k^2} \nabla(\nabla \cdot \vec{A}) \right) - \frac{1}{\epsilon} \nabla \times \vec{F}, \quad (3.7a)$$

$$\vec{H} = \frac{1}{\mu} \nabla \times \vec{A} - j\omega \left(\vec{F} + \frac{1}{k^2} \nabla(\nabla \cdot \vec{F}) \right). \quad (3.7b)$$

Here \vec{A} is the electric vector potential, \vec{F} is the magnetic vector potential and ϵ and μ are the permittivity and permeability, respectively. The parameter ω is the angular frequency and k is the wavenumber, which is related to the wavelength λ by $k = 2\pi / \lambda$. The distance R is given by $R = |\vec{r} - \vec{r}'|$, where \vec{r} is the observation point and \vec{r}' is the source point over the reflector surface. In (3.6), the subscript S denotes integration over the scatterer surface. From (3.7), the radiated electric and magnetic field is found by applying the various differential operators on \vec{A} and \vec{F} . The result becomes

$$\begin{aligned} \vec{E}(\vec{r}) = & \frac{Z_0}{4\pi} \iint_S (\vec{J} \left(-\frac{j}{kR} - \frac{1}{k^2 R^2} + \frac{j}{k^3 R^3} \right) \\ & + (\vec{J} \cdot \hat{R}) \hat{R} \left(\frac{j}{kR} + \frac{3}{k^2 R^2} - \frac{3j}{k^3 R^3} \right)) e^{-jkR} k^2 ds' \\ & - \frac{1}{4\pi} \iint_S \vec{M} \times \hat{R} \frac{1}{k^2 R^2} (1 + jkR) e^{-jkR} k^2 ds', \end{aligned} \quad (3.8a)$$

$$\begin{aligned} \vec{H}(\vec{r}) = & \frac{1}{4\pi} \iint_S \vec{J} \times \hat{R} \frac{1}{k^2 R^2} (1 + jkR) e^{-jkR} k^2 ds' \\ & + \frac{1}{4\pi Z_0} \iint_S (\vec{M} \left(-\frac{j}{kR} - \frac{1}{k^2 R^2} + \frac{j}{k^3 R^3} \right) \\ & + (\vec{M} \cdot \hat{R}) \hat{R} \left(\frac{j}{kR} + \frac{3}{k^2 R^2} - \frac{3j}{k^3 R^3} \right)) e^{-jkR} k^2 ds', \end{aligned} \quad (3.8b)$$

where

$$\hat{R} = \frac{\bar{R}}{R} = \frac{\bar{r} - \bar{r}'}{|\bar{r} - \bar{r}'|}, \quad (3.9)$$

and Z_0 is the free-space impedance, $Z_0 = \sqrt{\mu/\varepsilon}$. Notice that (3.8a) and (3.8b) are exact radiation integrals and are applicable to observation points both in the near-field zone and in the far-field zone. By using far-field approximation,

$$R \approx r = |\bar{r}| \text{ for the magnitude factor,} \quad (3.10a)$$

$$R \approx r - \frac{\bar{r}}{|\bar{r}|} \cdot \bar{r}' = r - \hat{r} \cdot \bar{r}' \text{ for the phase factor.} \quad (3.10b)$$

The definitions in (3.10a) and (3.10b) are substituted into (3.8a) and (3.8b), then

$$\begin{aligned} \vec{E}^{far}(\bar{r}) = & -\frac{jkZ_0}{4\pi} \iint_S (\bar{J} - (\bar{J} \cdot \hat{r})\hat{r}) e^{jk\bar{r}' \cdot \hat{r}} ds' \\ & + \frac{jk}{4\pi} \hat{r} \times \iint_S \bar{M} e^{jk\bar{r}' \cdot \hat{r}} ds', \end{aligned} \quad (3.11a)$$

$$\begin{aligned} \vec{H}^{far}(\bar{r}) = & -\frac{jk}{4\pi} \hat{r} \times \iint_S \bar{J} e^{jk\bar{r}' \cdot \hat{r}} ds' \\ & - \frac{jk}{4\pi Z_0} \iint_S (\bar{M} - (\bar{M} \cdot \hat{r})\hat{r}) e^{jk\bar{r}' \cdot \hat{r}} ds'. \end{aligned} \quad (3.11b)$$

If the current distributions are induced by electric and magnetic fields incident on a perfect electric conducting surface, the fields created by these currents are referred to

as scattered fields. Therefore, the far-fields are obtained by (3.11a) and (3.11b) by letting \vec{J} as in (3.1) and $\vec{M} = 0$. Thus

$$\vec{E}^s(\vec{r}) = -\frac{jZ_0k}{4\pi} \iint_S (\vec{J} - (\vec{J} \cdot \hat{r})\hat{r}) e^{jk\vec{r}' \cdot \hat{r}} ds', \quad (3.12a)$$

$$\vec{H}^s(\vec{r}) = -\frac{jk}{4\pi} \hat{r} \times \iint_S \vec{J} e^{jk\vec{r}' \cdot \hat{r}} ds', \quad (3.12b)$$

where \hat{r} is the far-field direction $\hat{r} = \vec{r} / |\vec{r}|$.

It is seen that (3.12a) and (3.12b) satisfy the relations

$$\vec{E}^{far} = Z_0 \vec{H}^{far} \times \hat{r}, \quad (3.13a)$$

$$\vec{H}^{far} = \frac{1}{Z_0} \hat{r} \times \vec{E}^{far}, \quad (3.13b)$$

which expresses the well-known connection between the E- and H-field for a plane wave propagation in the direction \hat{r} .

The near-field and far-field are calculated by numerical integration of (3.8) and (3.11) for exact solution or using integral of (3.12) for PO approximation. The integral in (3.12) can be transformed into standard two-dimensional (polar coordinate) to have an efficient procedure (Pontoppidan, 2005) as

$$\bar{E}^s(\bar{r}) \approx -\frac{jZ_0k}{4\pi} \iint_S (\bar{J} - (\bar{J} \cdot \hat{r})\hat{r}) e^{jk\bar{r} \cdot \hat{r}} \mathbf{J}_A \rho' d\rho' d\phi', \quad (3.14a)$$

$$\bar{H}^s(\bar{r}) \approx -\frac{jk}{4\pi} \hat{r} \times \iint_A \bar{J} e^{jk\bar{r} \cdot \hat{r}} \mathbf{J}_A \rho' d\rho' d\phi', \quad (3.14b)$$

where \mathbf{J}_A is the surface Jacobian transformation given by

$$\mathbf{J}_A = \sqrt{1 + \left(\frac{\partial f}{\partial x}\right)^2 + \left(\frac{\partial f}{\partial y}\right)^2}. \quad (3.15)$$

$z = f(x, y)$ gives the description of the reflector surface and A defines the area of the projected aperture as shown in figure 3.3. Note that, although integration in (3.14) is performed over the planar aperture, the current still be defined on the curved reflector surface.

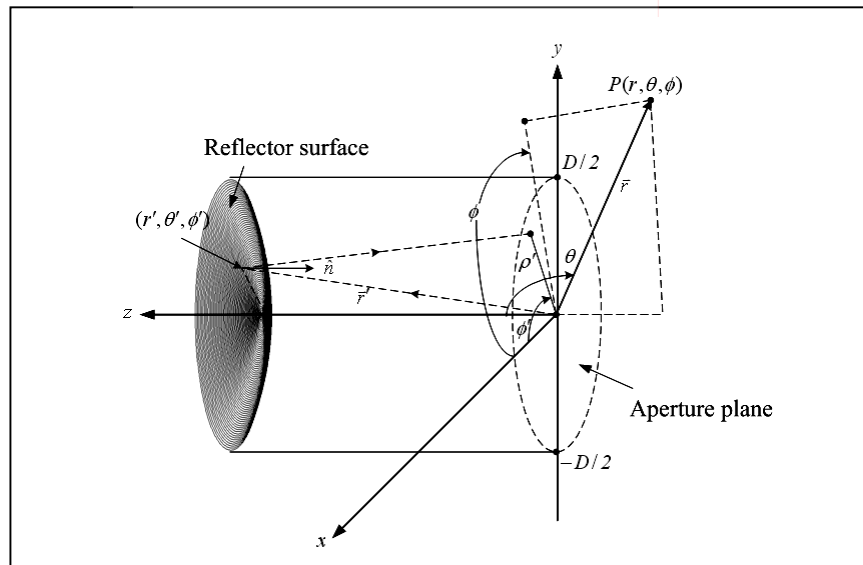


Figure 3.3 Three-dimensional geometry of a reflector antenna and its parameters.

3.3 Physical Theory of Diffraction (PTD)

As explained in section 3.2, physical optics gives an approximation to the scattered field

$$\bar{E}^s \simeq \bar{E}^{PO}. \quad (3.16)$$

The physical optics currents approximate the equivalent currents on a scatterer derived from scattering by an infinite planar surface. Therefore, the radiated field of a reflector predicted by the physical optics technique is accurate in the main beam region and for the first few sidelobes. However, for observations in the far-angular regions or for prediction of the cross-polarized fields, the PO solution may not be accurate due to the ignorance of the effect of edge diffraction. Physical theory of diffraction (PTD) is an integrative technique in which the total scattered field is refined by the adding a fringe field to physical optics field as expressed in (3.17).

$$\bar{E}^{PTD} \simeq \bar{E}^{PO} + \bar{E}^{FW}, \quad (3.17)$$

where \bar{E}^{PTD} is total scattered field from physical theory of diffraction technique, \bar{E}^{PO} is scattered field due to physical optics current, and \bar{E}^{FW} is scattered field due to fringe current (nonuniform current) at the edge of reflector.

The PTD method in this research is based on Michaeli (1986). In Michaeli's work, he derived the GTD equivalent edge current by asymptotically reducing the surface to edge integral for an arbitrary aspect of observation. Later, Michaeli evaluated the fringe current radiation integral over the ray coordinate instead of over the normal coordinate. This improvement corrected many of the singularities in

Mitzner's ILDC (Michaeli, 1986). The fringe field due to nonuniform current along the edge of reflector can be calculated by

$$\vec{E}^{FW} \cong jk \int_C \left[ZI^{FW}(\vec{r}'_{rim}) \hat{s} \times (\hat{s} \times \hat{e}) + M^{FW}(\vec{r}'_{rim}) \hat{s} \times \hat{e} \right] G(\vec{r}'_{rim}, \vec{r}) dl, \quad (3.18)$$

where k is the wavenumber of incident wave, Z is the impedance of medium, \vec{r} is the position vectors of the observation point, $dl = |d\vec{r}'_{rim}|$ is the increment of arc length l along the edge C , and \vec{r}'_{rim} is the position vectors of a point on edge C (see Figure 3.4), which can be obtained by

$$\vec{r}'_{rim} = r^a(v') \cos v' \vec{a}_x + r^a(v') \sin v' \vec{a}_y + z_{rim} (r^a(v') \cos v', r^a(v') \sin v') \vec{a}_z. \quad (3.19)$$

\hat{e} is the unit vector tangential to the point on edge $Q_{rim}(x_{rim}, y_{rim}, z_{rim})$, which is obtained by

$$\hat{e} = \frac{\partial \vec{r}'_{rim}}{\partial l} = \frac{\frac{\partial \vec{r}'_{rim}}{\partial x} \vec{a}_x + \frac{\partial \vec{r}'_{rim}}{\partial y} \vec{a}_y + \frac{\partial \vec{r}'_{rim}}{\partial z} \vec{a}_z}{\sqrt{\left(\frac{\partial \vec{r}'_{rim}}{\partial x}\right)^2 + \left(\frac{\partial \vec{r}'_{rim}}{\partial y}\right)^2 + \left(\frac{\partial \vec{r}'_{rim}}{\partial z}\right)^2}}. \quad (3.20)$$

\hat{s}' is the unit vector from the feed (x_f, y_f, z_f) to the edge $(x_{rim}, y_{rim}, z_{rim})$ as expressed by

$$\hat{s}' = \frac{\vec{s}'}{|\vec{s}'|} = \frac{\vec{r}'_{rim} - \vec{r}_f}{|\vec{r}'_{rim} - \vec{r}_f|} = \frac{(x_{rim} - x_f) \vec{a}_x + (y_{rim} - y_f) \vec{a}_y + (z_{rim} - z_f) \vec{a}_z}{\sqrt{(x_{rim} - x_f)^2 + (y_{rim} - y_f)^2 + (z_{rim} - z_f)^2}}. \quad (3.21)$$

\hat{s} is the unit vector from the edge $(x_{rim}, y_{rim}, z_{rim})$ to the observation point (x, y, z) , which can be obtained by

$$\hat{s} = \frac{\vec{s}}{|\vec{s}|} = \frac{\vec{r} - \vec{r}'_{rim}}{|\vec{r} - \vec{r}'_{rim}|} = \frac{(x - x_{rim})\vec{a}_x + (y - y_{rim})\vec{a}_y + (z - z_{rim})\vec{a}_z}{\sqrt{(x - x_{rim})^2 + (y - y_{rim})^2 + (z - z_{rim})^2}}. \quad (3.22)$$

$G(\vec{r}'_{rim}, \vec{r})$ is the three-dimensional Green's function which is given by

$$G(\vec{r}'_{rim}, \vec{r}) = \frac{e^{-jks}}{4\pi s}. \quad (3.23)$$

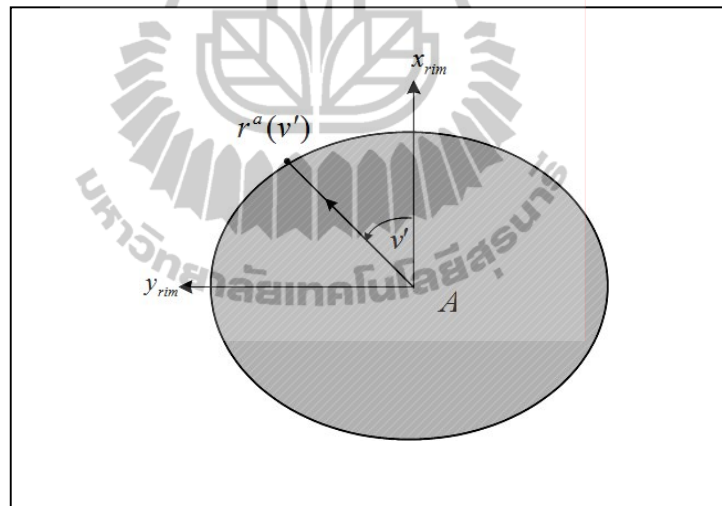


Figure 3.4 Reflector aperture and edge coordinate system.

In Michaeli's equivalent edge currents (Michaeli, 1986), the final expressions for the electrical equivalent fringe current (I^{FW}) and the magnetic equivalent fringe current (M^{FW}) are obtained by

$$\begin{aligned}
I^{FW} = & (E_o^i \cdot \hat{e}) \frac{2j}{Zk \sin^2 \beta'} \frac{\sqrt{2} \sin(\frac{\phi'}{2})}{\cos \phi' + \mu} \left[\sqrt{1-\mu} - \sqrt{2} \cos(\frac{\phi'}{2}) \right] \\
& + (H_o^i \cdot \hat{e}) \frac{2j}{k \sin \beta' \cos \phi' + \mu} \cdot [\cot \beta' \cos \phi' + \cot \beta \cos \phi \\
& + \sqrt{2} \cos(\frac{\phi'}{2}) (\mu \cot \beta' - \cot \beta \cos \phi) (1-\mu)^{-\frac{1}{2}}],
\end{aligned} \tag{3.24a}$$

$$\begin{aligned}
M^{FW} = & (H_o^i \cdot \hat{e}) \frac{2jZ \sin \phi}{k \sin \beta \sin \beta' \cos \phi' + \mu} \\
& \times \left[1 - \sqrt{2} \cos(\frac{\phi'}{2}) (1-\mu)^{-\frac{1}{2}} \right],
\end{aligned} \tag{3.24b}$$

where $\mu = \frac{\cos \gamma - \cos^2 \beta'}{\sin^2 \beta'}$ and $\cos \gamma = \sin \beta' \sin \beta \cos \phi + \cos \beta' \cos \beta$. Defining (β', ϕ') is the incident wave coordinate system and (β, ϕ) is the fringe wave coordinate system. \vec{E}_o^i and \vec{H}_o^i denote the incident electric and magnetic field vector, respectively, as shown in Figure 3.5. The radiated fields of the reflector antenna can be obtained by the summation of physical optics fields of (3.14) and the fringe field of (3.18).

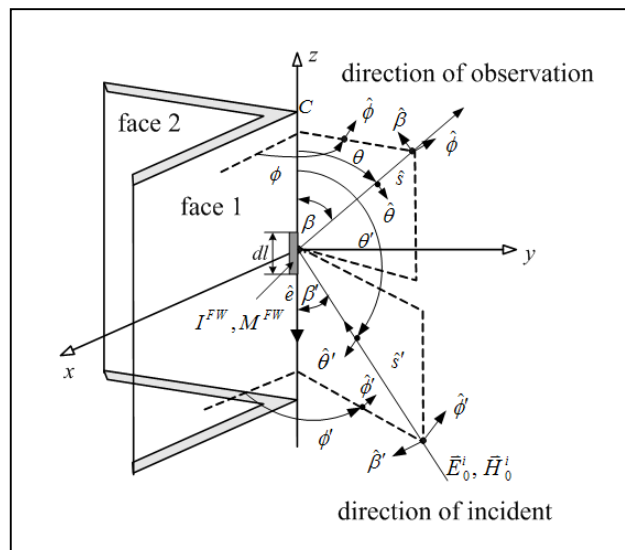


Figure 3.5 Wedge scattering geometry.

3.4 Radiation Characteristics of Antenna

3.4.1 Radiation Pattern

The radiation pattern can be expressed as a mathematical function or a graphical presentation of the radiation properties of the antenna as a function of space coordinates (Balanis, 2005). In most cases, the radiation pattern is determined in the far-field region and is represented as a function of the directional coordinates. Radiation properties include power flux density, radiation intensity, field strength, directivity, phase or polarization. The far-field pattern is the angular distribution (θ, ϕ) of the field quantity on constant radius sphere. A trace of the received electric (magnetic) field at constant radius is called the amplitude field pattern. On the other hand, a graph of the spatial variation of the power density along a constant radius is called an amplitude power pattern. The power pattern is usually plotted on a logarithmic scale or more commonly in decibels (dB).

3.4.2 Beamwidth

The beamwidth of a pattern is defined as the angular separation between two identical points on opposite side of the pattern maximum. In an antenna pattern, one of the most widely used beamwidths is the Half-Power Beamwidth (HPBW), which is defined by IEEE as: In a plane containing the direction of the maximum of a beam, the angle between the two directions in which the radiation intensity is one-half value of the beam (Balanis, 2005).

3.4.3 Directivity

Directivity of an antenna is ratio of the power radiated in a given direction to the power averaged over all directions (Thomus, 1985). The average power is equal to the total power radiated by the antenna divided by 4π , which gives

$$D(\theta, \phi) = \frac{dP / d\Omega}{P_{total} / 4\pi} = 4\pi \frac{dP / d\Omega}{P_{total}}, \quad (3.25)$$

where P_{total} is the total power

$$P_{total} = \int P(\theta, \phi) d\Omega = \int_0^{2\pi} \int_0^{\pi} P(\theta, \phi) \sin \theta d\theta d\phi. \quad (3.26)$$

The maximum value of directivity $D(\theta, \phi)$ is often called the directivity of the antenna and it is a measure of the ability of an antenna to concentrate the radiated power to a certain direction. An isotropic radiator radiates uniformly to all directions. Directivity is often expressed in reference to an isotropic radiator in decibels denoted with dBi.

The directivity of the antenna can be estimated to any convenient level. The most accurate estimate is based on measurements at equal angle increments over the whole radiation sphere (Thomus, 1985). Estimating directivity of antenna when the E-and H-plane pattern beamwidths are known, the directivity can be obtained by

$$D \approx \frac{4\pi(180 / \pi)^2}{\Theta_E \Theta_H} = \frac{41,253}{\Theta_E \Theta_H}, \quad (3.27)$$

where Θ_E is half-power beamwidth in E-plane (degree),

Θ_H is half-power beamwidth in H-plane (rad).

Many times, it is desirable to express the directivity in decibels (dB) instead of dimensionless quantities. The expression for converting the dimensionless quantities of directivity to decibels (dB) is calculated by

$$D(\text{dB}) = 10 \log_{10} [D(\text{dimensionless})]. \quad (3.28)$$

3.4.4 Antenna Efficiency

The total antenna efficiency e_0 is used to take into account losses at the input terminals and within the structure of the antenna. Such losses may be due to

- 1) reflections because of the mismatch between the transmission line and the antenna
- 2) I^2R losses (conduction and dielectric)

In general, the overall efficiency can be written as (Balanis, 1985)

$$e_0 = e_r e_c e_d, \quad (3.29)$$

where e_0 is total efficiency (dimensionless),

e_r is reflection (mismatch) efficiency $= (1 - |\Gamma|^2)$ (dimensionless),

e_c is conduction efficiency (dimensionless),

e_d is dielectric efficiency (dimensionless),

Γ is voltage reflection coefficient at the input terminals of the antenna, $[\Gamma = (Z_{in} - Z_0) / (Z_{in} + Z_0)]$ where Z_{in} is antenna input impedance, Z_0 is characteristic impedance of the transmission line],

$$\text{VSWR} = \text{voltage standing wave ratio} = \frac{1+|\Gamma|}{1-|\Gamma|}. \quad (3.30)$$

Usually e_c and e_d are very difficult to compare, but they can be determined experimentally. Even by measurements, they cannot be separated, and it is usually more convenient to write as

$$e_0 = e_r e_{cd} = e_{cd} (1 - |\Gamma|^2), \quad (3.31)$$

where $e_{cd} = e_c e_d$ is antenna radiation efficiency, which is used to related the gain and directivity.

In the case of aperture antennas, antenna radiation efficiency can be obtained by

$$e_{cd} = G_0 (\lambda_0 / \pi D_m)^2, \quad (3.32)$$

where G_0 is the antenna gain, λ_0 is free space wavelength and D_m is aperture diameter.

3.4.5 Gain

When the antennas are used in any system such as communication systems, the primary interested characteristic of an antenna is the gain. It is a measure of how much of the input power is concentrated in a particular direction. Gain of an antenna (in a given direction) is defined as the ratio of the intensity, in a given direction, to the radiation intensity that would be obtained if the power accepted by the antenna were radiated isotropically. The radiation intensity corresponding to the

isotropically radiated power is equal to the power accepted (input) by the antenna divided by 4π (Balanis, 2005). The gain equation can be expressed as

$$Gain = 4\pi \frac{\text{radiated intensity}}{\text{total input (accepted) power}} = 4\pi \frac{U(\theta, \phi)}{P_{in}}. \quad (3.33)$$

The radiation intensity can be represented by

$$U(\theta, \phi) = \frac{1}{2} \text{Re}(E \times H^*) \cdot r^2 \hat{r} = \frac{|E(\theta, \phi)|^2 r^2}{2Z}. \quad (3.34)$$

The antenna gain is related to the directivity by

$$G(\theta, \phi) = e_{cd} D(\theta, \phi), \quad (3.35)$$

where e_{cd} is the antenna radiation efficiency, which includes the losses within the antenna. Impedance and polarization mismatch losses are not included.

3.4.6 Polarization

Polarization of an antenna in a given gain is defined as the polarization of the wave transmitted (radiated) by the antenna. Polarization is classified as linear, circular and elliptical based on the shape of figure that the electric field vector end point draws as the function of time. In general, the polarization characteristics of an antenna can be represented by its polarization pattern whose one definition is the spatial distribution of the polarizations of a field vector excited (radiated) by an antenna taken over its radiation sphere. At each point on the radiation sphere the polarization is usually resolved into a pair of orthogonal polarizations, the

co-polarization and cross-polarization. Co-polarization is the polarization that the antenna is intended to radiate or to receive. The orthogonal polarization to the co-polarization is called cross-polarization.

3.5 Numerical Example for Reflector Antenna Analysis

It is well known that the radiated field of a reflector antenna predicted by using PO is accurate in the main beam region and for the first few sidelobes. However, for observations in the far angular regions, the PO solution may not be accurate due to the ignorance of the edge diffraction effect. Therefore, it is desirable to apply the PTD fringe field in reflector antenna analysis as a complement to the PO field, and investigate the improvement in field prediction. For this purpose, the numerical example for reflector antenna will be presented in this section to demonstrate the effectiveness of the PTD fringe field to improve the PO field. As shown in Figure 3.6, the antenna under consideration contains a reflector by using backscattering technique to achieve wide beamwidth, and feed horn. A standard X-band pyramidal horn is used to be feed of the antenna. The geometry of pyramidal horn is shown in Figure 3.7. The horn dimensions are $\rho_1 = \rho_2 = 2.3\lambda$ (6.9 cm), $a_1 = 1.5\lambda$ (4.5 cm), $b_1 = 1.6\lambda$ (4.8 cm), $a = 0.76\lambda$ (2.28 cm), and $b = 0.34\lambda$ (1.02 cm). The feed horn is placed at a position that estimates illumination the reflector edge with -10 dB when compared with the illumination at the center of reflector. The figure of merit of -10 dB edge illumination may be considered as a compromise between the amount of spillover, on the one hand, and the efficient illumination of reflector surface on the other.

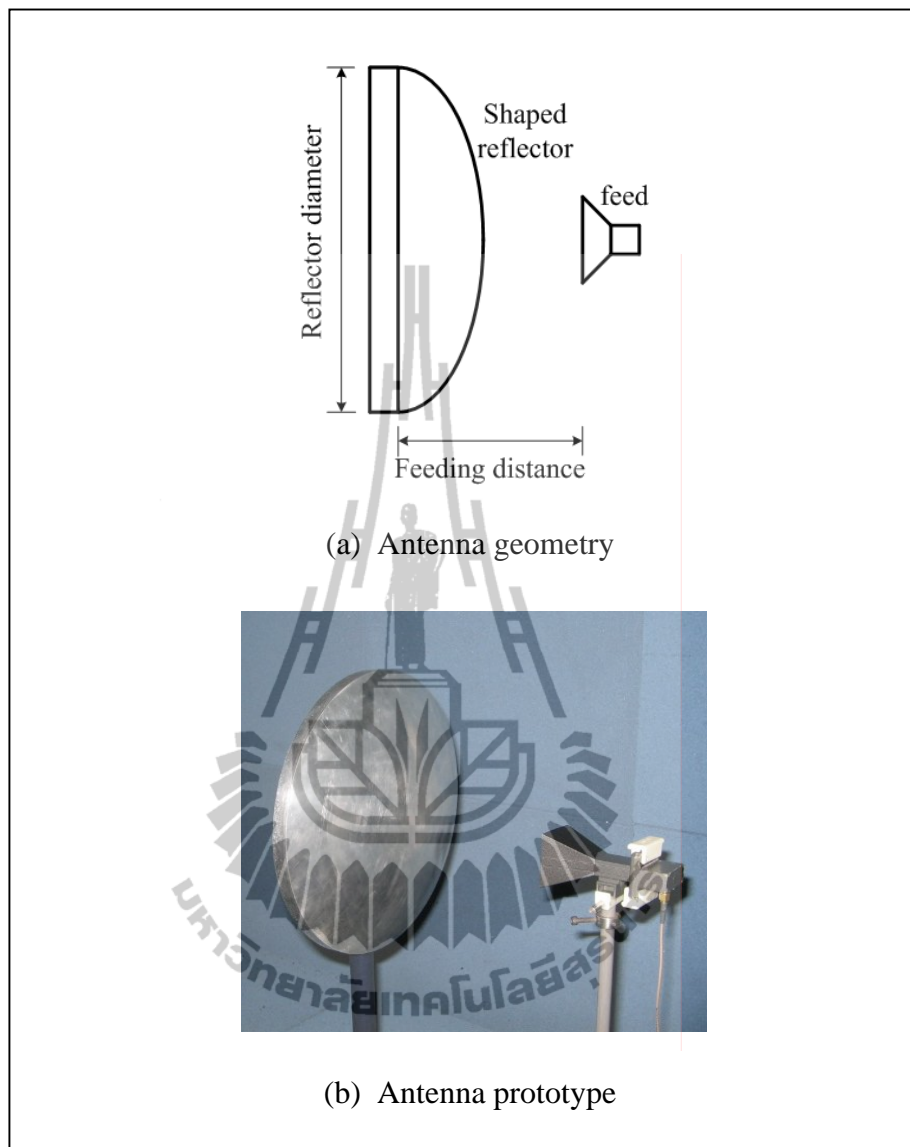


Figure 3.6 Reflector antenna geometry and its prototype.

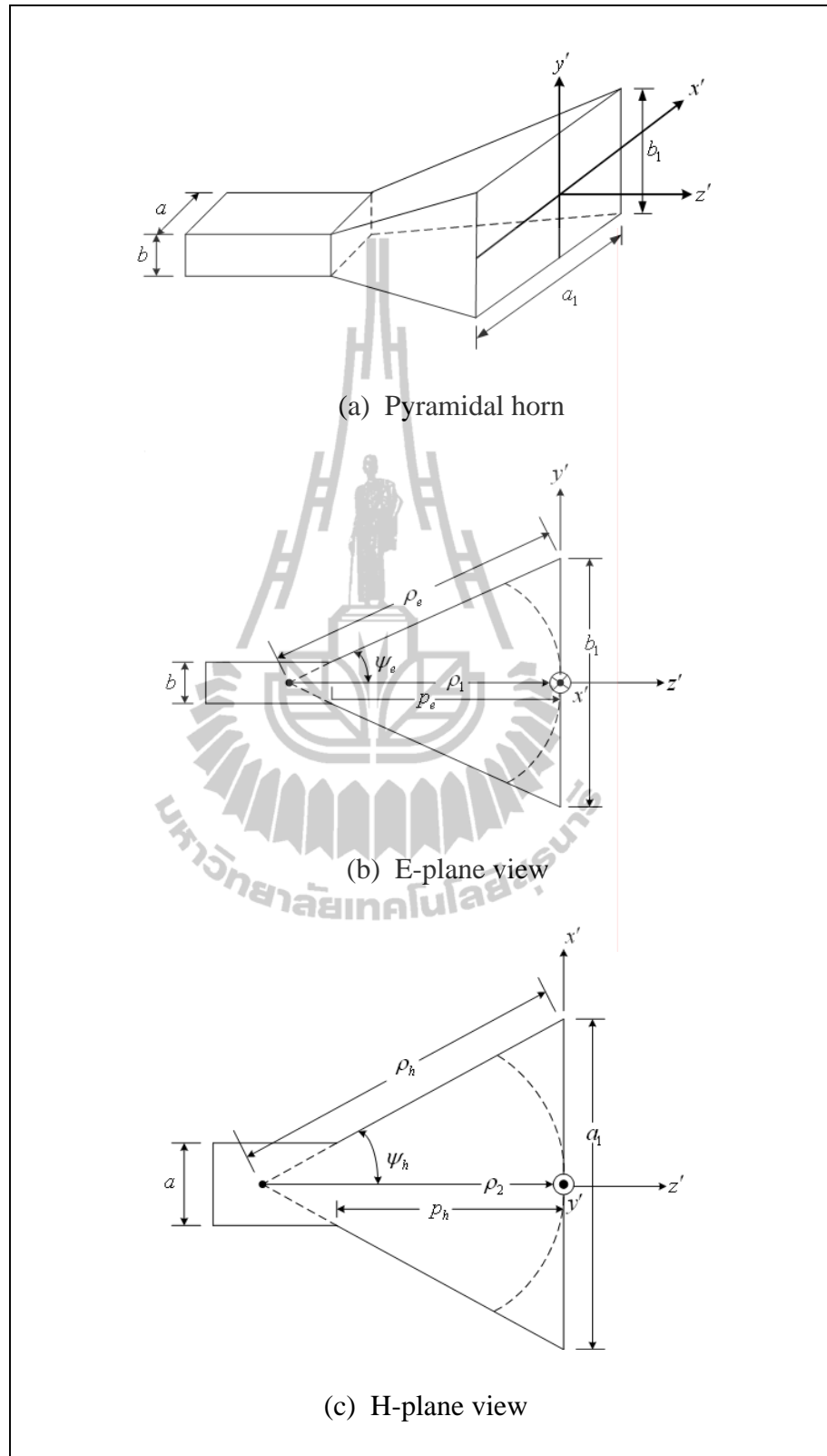


Figure 3.7 Pyramidal horn and coordinate system.

The procedure for analysis the radiation pattern of reflector antenna by using PO/PTD is described in the following.

(1) To define the inputs of geometrical and electrical parameters such as frequency of operation, reflector geometry (diameter, position and its equation) and feed characteristics (feed type and position). In this example, we have analyzed the radiation pattern of reflector antenna at frequency 10 GHz. The reflector curve is quadratic equation that depends on the parameters D_m , A and L . The equation of a quadratic is of the form

$$z_{mr}(x_{mr}) = A \left(1 - \left(\frac{2}{D_m} x_{mr} \right)^2 \right) - L, \quad (3.36)$$

with $-\frac{D_m}{2} \leq x_{mr} \leq \frac{D_m}{2}$.

D_m is defined to be the diameter of quadratic reflector (30 cm) and A is the convexity of quadratic reflector (3.5 cm) and L is feeding distance (17 cm). The 10 GHz standard X-band pyramidal horn is used to be a feed of the antenna.

(2) To calculate the horn aperture surface and current: Defining a coordinate system centered on the horn aperture with the x axis parallel to the broad dimension of the horn and the z axis pointing out along the normal of the aperture, x and y coordinate of feed aperture sampling is illustrated in Figure 3.8. For a pyramidal horn, the aperture electric (\vec{E}^a) fields and magnetic fields (\vec{H}^a) in the aperture plane are approximated by Balanis, (2005)

$$E_x^a = E_0 \cos\left(\frac{\pi x'}{a_1}\right) e^{-jk\left(\frac{x'^2}{2\rho_2} + \frac{y'^2}{2\rho_1}\right)}, \quad (3.37a)$$

$$H_x^a = -\frac{E_0}{\eta} \cos\left(\frac{\pi x'}{a_1}\right) e^{-jk\left(\frac{x'^2}{2\rho_2} + \frac{y'^2}{2\rho_1}\right)}, \quad (3.37b)$$

where η is the intrinsic impedance of the medium ($\approx 120\pi$ ohms for a free space medium). The electric and magnetic currents at the aperture of feed horn are given by

$$\vec{J}_a = \hat{n} \times \vec{H}^a, \quad (3.38a)$$

$$\vec{M}_a = -\hat{n} \times \vec{E}^a, \quad (3.38b)$$

where $\hat{n} = \hat{z}$ is normal unit vector pointing out along the normal of the horn aperture. The far-field of pyramidal horn can be predicted by using the aperture field integration method. With the equivalent electric and magnetic currents, the electric and magnetic fields can be obtained by using (3.8). The integration is performed over the horn aperture,

$$\int_{\Sigma'} ds'_a = \int_{-b_1/2}^{b_1/2} \int_{-a_1/2}^{a_1/2} dx' dy'. \quad (3.39)$$

The far-field radiation pattern of the pyramidal horn is shown in Figure 3.9. The relative power of this horn at the angle $\pm 28^\circ$ in E-plane and the angle $\pm 41^\circ$ in H-plane provide -10 dB edge illumination on reflector and provides feeding distance about 28 cm in E-plane and 17 cm in H-plane.

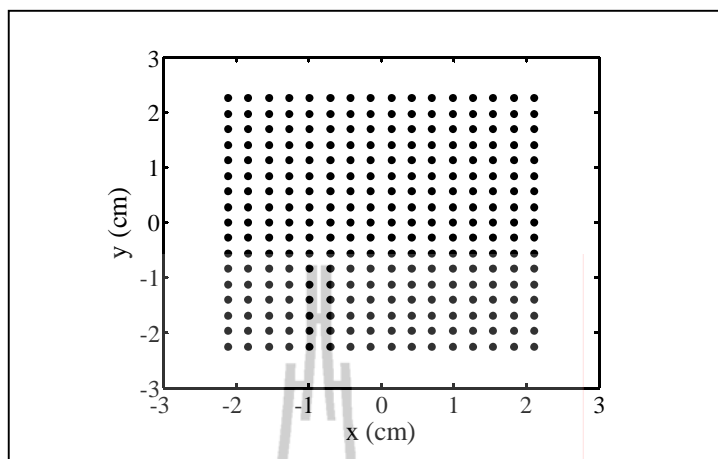


Figure 3.8 The sampling points in the x and y directions of feed aperture.

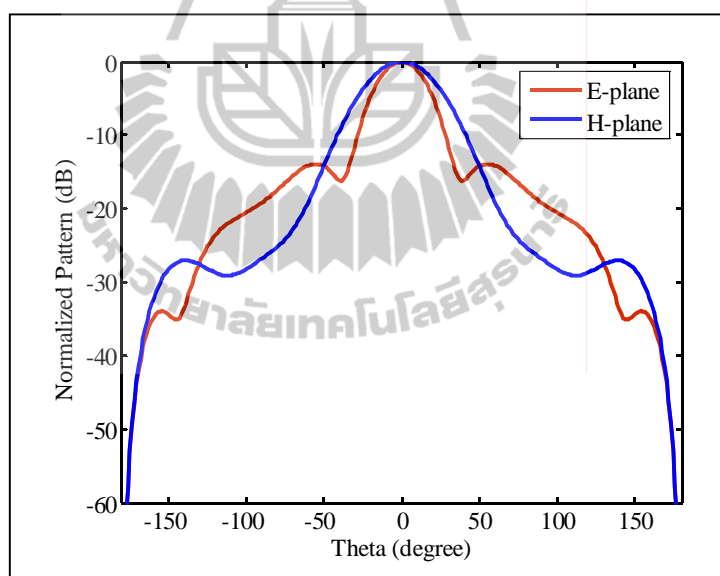


Figure 3.9 Radiation patterns of standard X-band pyramidal horn.

(3) To calculate the physical optics currents on the reflector surface: The physical optics currents on reflector surface can be obtained directly from the components of the incident field tangential to the reflector at each point on its surface as shown in Figure 3.10.

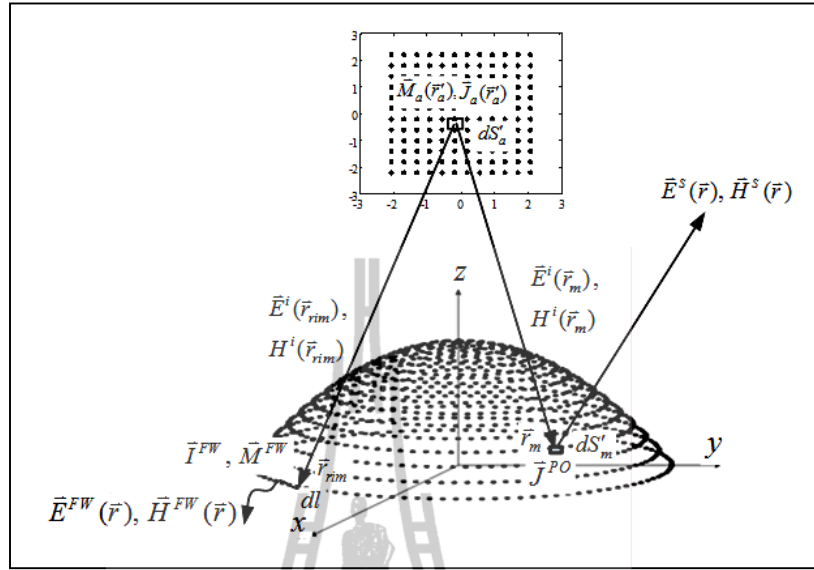


Figure 3.10 PO/PTD for reflector antenna analysis.

The incident magnetic fields (\vec{H}^i) can be obtained by (3.8b) and replace electric current (\vec{J}) by $\vec{J}_a(\vec{r}'_a)$ and (\vec{M}) by $\vec{M}_a(\vec{r}'_a)$ as expressed in (3.40).

$$\begin{aligned} \vec{H}^i(\vec{r}_m) = & \frac{1}{4\pi} \iint_S \vec{J}_a(\vec{r}'_a) \times \hat{R} \frac{1}{k^2 R^2} (1 + jkR) e^{-jkR} k^2 ds'_a \\ & + \frac{1}{4\pi Z_0} \iint_S (\vec{M}_a(\vec{r}'_a)) \left(-\frac{j}{kR} - \frac{1}{k^2 R^2} + \frac{j}{k^3 R^3} \right) \\ & + (\vec{M}_a(\vec{r}'_a) \cdot \hat{R}) \hat{R} \left(\frac{j}{kR} + \frac{3}{k^2 R^2} + \frac{j}{k^3 R^3} \right) e^{-jkR} k^2 ds'_a. \end{aligned} \quad (3.40)$$

Where $\vec{J}_a(\vec{r}'_a)$ and $\vec{M}_a(\vec{r}'_a)$ is the electric and magnetic currents on horn aperture at \vec{r}'_a , respectively. \vec{r}'_a and \vec{r}_m are the position vectors of source points on horn aperture and observation points on the reflector surface, respectively. $R = |\vec{r}_m - \vec{r}'_a|$ is distance between source points on horn aperture and observation points on the reflector surface and $\hat{R} = \vec{r}_m - \vec{r}'_a / |\vec{r}_m - \vec{r}'_a|$. s'_a is the surface areas of the samples on the horn aperture.

The integration is performed over the horn aperture as expressed in (3.39). When we know the incident fields from feed, the physical optics current on reflector surface can be obtained by $\bar{J}^{PO} = 2\hat{n} \times \bar{H}^i$ as expressed in (3.1). \hat{n} is the normal unit vector pointing out along the normal of the reflector surface.

(4) To calculate the fringe currents on the edge of reflector: The electrical equivalent fringe current (I^{FW}) and the magnetic equivalent fringe current (M^{FW}) on the edge of reflector can obtain by (3.24a) and (3.24b), respectively. \bar{E}_o^i and \bar{H}_o^i in (3.24a) and (3.24b) denote the vectors of incident electric and magnetic fields, respectively, which impinge upon the edge of reflector, respectively. \bar{E}_o^i and \bar{H}_o^i can be obtained by

$$\begin{aligned} \bar{E}^i(\bar{r}_{rim}) = & \frac{Z_0}{4\pi} \iint_S (\bar{J}_a(\bar{r}'_a) \left(-\frac{j}{kR} - \frac{1}{k^2 R^2} + \frac{j}{k^3 R^3} \right) \\ & + (\bar{J}_a(\bar{r}'_a) \cdot \hat{R}) \hat{R} \left(\frac{j}{kR} + \frac{3}{k^2 R^2} - \frac{3j}{k^3 R^3} \right)) e^{-jkR} k^2 ds'_a \\ & - \frac{1}{4\pi} \iint_S \bar{M}_a(\bar{r}'_a) \times \hat{R} \frac{1}{k^2 R^2} (1 + jkR) e^{-jkR} k^2 ds'_a, \end{aligned} \quad (3.41a)$$

$$\begin{aligned} \bar{H}^i(\bar{r}_{rim}) = & \frac{1}{4\pi} \iint_S \bar{J}_a(\bar{r}'_a) \times \hat{R} \frac{1}{k^2 R^2} (1 + jkR) e^{-jkR} k^2 ds'_a \\ & + \frac{1}{4\pi Z_0} \iint_S (\bar{M}_a(\bar{r}'_a) \left(-\frac{j}{kR} - \frac{1}{k^2 R^2} + \frac{j}{k^3 R^3} \right) \\ & + (\bar{M}_a(\bar{r}'_a) \cdot \hat{R}) \hat{R} \left(\frac{j}{kR} + \frac{3}{k^2 R^2} - \frac{3j}{k^3 R^3} \right)) e^{-jkR} k^2 ds'_a, \end{aligned} \quad (3.41b)$$

where $\bar{J}_a(\bar{r}'_a)$ and $\bar{M}_a(\bar{r}'_a)$ are the electric and magnetic currents on horn aperture at \bar{r}'_a , respectively. \bar{r}'_a and \bar{r}_{rim} are the position vectors of source points on horn aperture and observation points on edge of reflector, respectively. $R = |\bar{r}_{rim} - \bar{r}'_a|$ is the distance

between source points on horn aperture and observation points on edge of reflector and $\hat{R} = \vec{r}_{rim} - \vec{r}'_a / |\vec{r}_{rim} - \vec{r}'_a|$. s'_a is the surface areas of the samples on the horn aperture.

(5) To calculate the scattered fields due to the physical optics currents: The scattered field due to the physical optics current can be obtained by (3.8) or (3.12) for far-field and then replaced electric current (\vec{J}) by $\vec{J}^{PO}(\vec{r}'_m)$ as expressed in (3.42)

$$\vec{E}^s(\vec{r}) = -\frac{jZ_0k}{4\pi} \iint_S (\vec{J}^{PO}(\vec{r}'_m) - (\vec{J}^{PO}(\vec{r}'_m) \cdot \hat{r})\hat{r}) e^{jk\vec{r}'_m \cdot \vec{r}} ds'_m, \quad (3.42a)$$

$$\vec{H}^s(\vec{r}) = -\frac{jk}{4\pi} \hat{r} \times \iint_S \vec{J}^{PO}(\vec{r}'_m) e^{jk\vec{r}'_m \cdot \vec{r}} ds'_m, \quad (3.42b)$$

where $\vec{J}^{PO}(\vec{r}'_m)$ is the physical optics currents on reflector surface at \vec{r}'_m . \vec{r}'_m and \vec{r} are the position vectors of the source points on reflector surface and observation points in far-field zone, respectively. \hat{r} is the far-field direction where $\hat{r} = \vec{r} / |\vec{r}|$. s'_m is the surface areas of the samples on the reflector surface.

(6) To calculate the fringe fields due to the fringe currents: The fringe fields due to the fringe currents can be obtained by (3.18).

(7) To calculate total scattered field: The approximation of physical optics current in (3.1) ignores the fact that the scatterer may be of finite size and may have sharp edge. This problem is considered more carefully in PTD where a “fringe field” is added to the PO field for constructing the total scattered field,

$$\vec{E}^{PTD} \simeq \vec{E}^{PO} + \vec{E}^{FW}. \quad (3.43)$$

The PTD procedure for analysis the radiation pattern of reflector antenna as described above can be summarized in Figure 3.11.

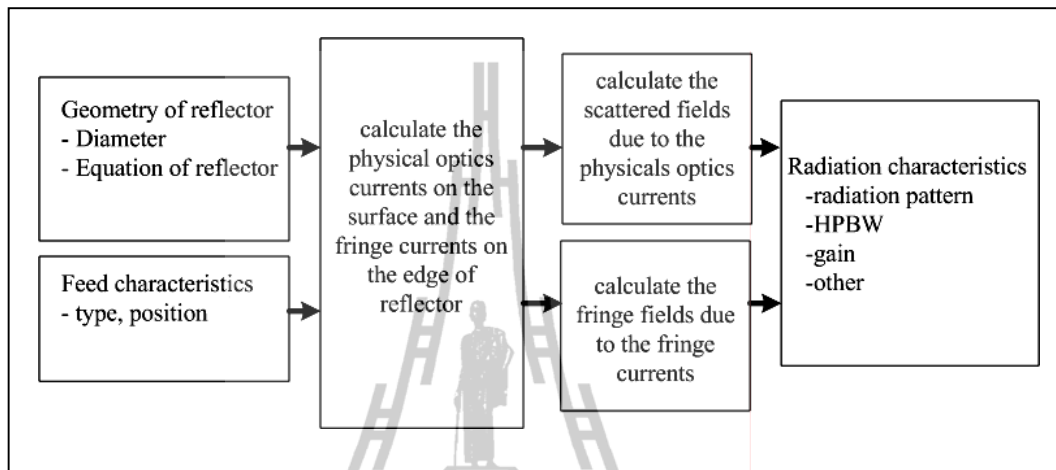


Figure 3.11 Analytical procedure for PTD.

For numerical example, we have analyzed the radiation pattern of quadratic reflector antenna with diameter 30 cm, the convexity of a quadratic reflector 3.5 cm and feeding distance 17 cm. The PO and PTD procedure as described above, the far-field patterns of the quadratic reflector antenna in E-and H-plane are illustrated in Figure 3.12. It is found that in the near-in angular region, the PO and PTD are in perfect agreement. This is because the PO currents are set to zero in the shadowed region, creating shadow boundary on the reflector surface. In addition, the discontinuity of the current density over the rim of reflector is neglected. These approximations lead to accurate results for the radiated fields on the near-in angular region.

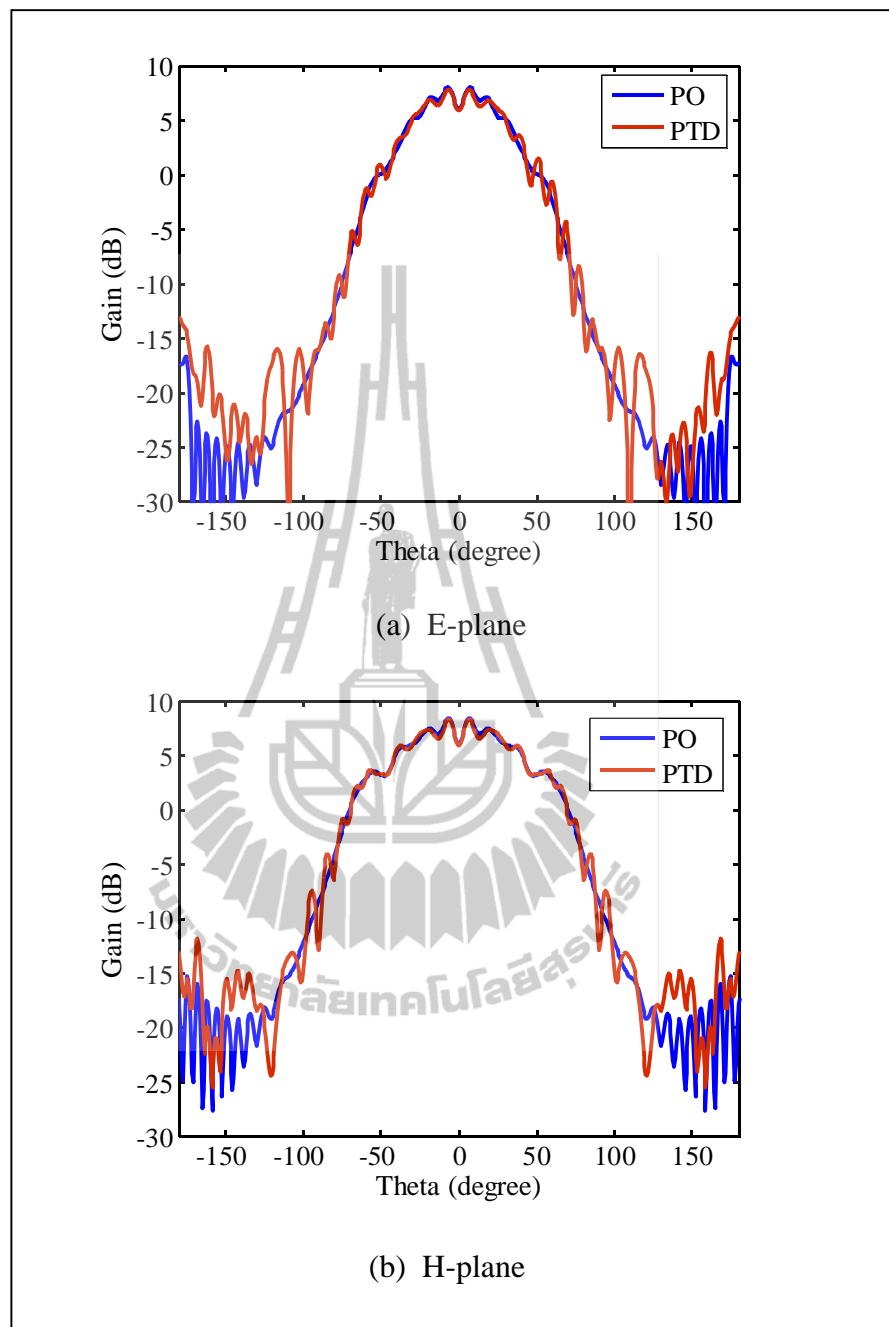


Figure 3.12 Far-field patterns of the quadratic reflector antenna by using PO/PTD.

It is observed that the envelope errors at $0^\circ \leq \theta \leq 10^\circ$ of E- and H-plane patterns are lower than 0.5 dB. To predict the pattern more accurately in all regions, especially the far angle region, diffraction techniques are applied. It is commonly argued that the field pattern results by PTD yield the accuracy more than by PO method, especially, in the far angular region. It is also observed that, the field patterns in the E- and H-plane, which are predicted by PTD, yielding the far-field envelope higher than by PO method.

Although the patterns in Figure 3.12 at first sight look identical but there are in fact discrepancies in the region behind the reflector, i.e. for $70^\circ \leq \theta \leq 180^\circ$. In Figure 3.13, the discrepant region is zoomed to illustrate the difference of calculated results by PO and PTD. It is found that the results by using this two methods clearly disagree by as much 10 dB on some of the lobes for E- plane and as much 5 dB for H-plane.

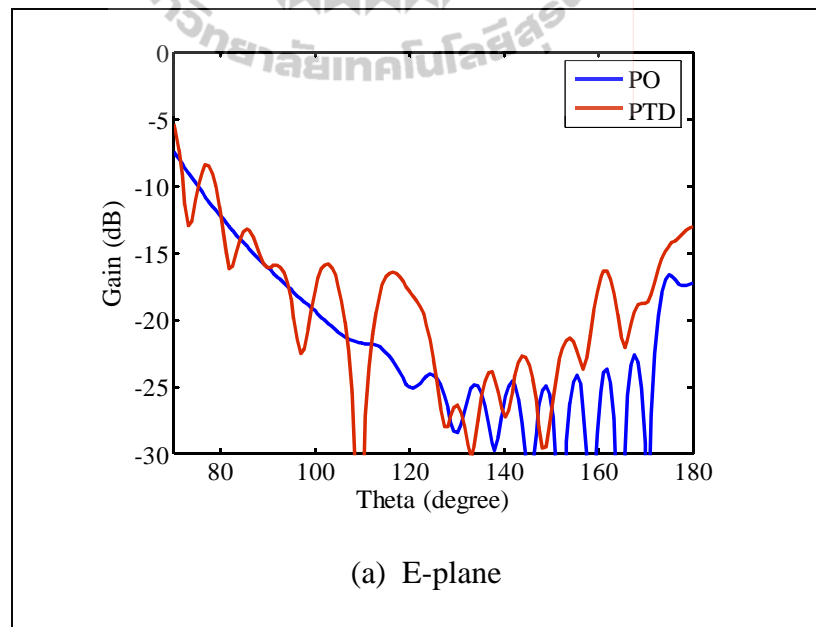


Figure 3.13 Close look at the rear pattern in E-and H-plane.

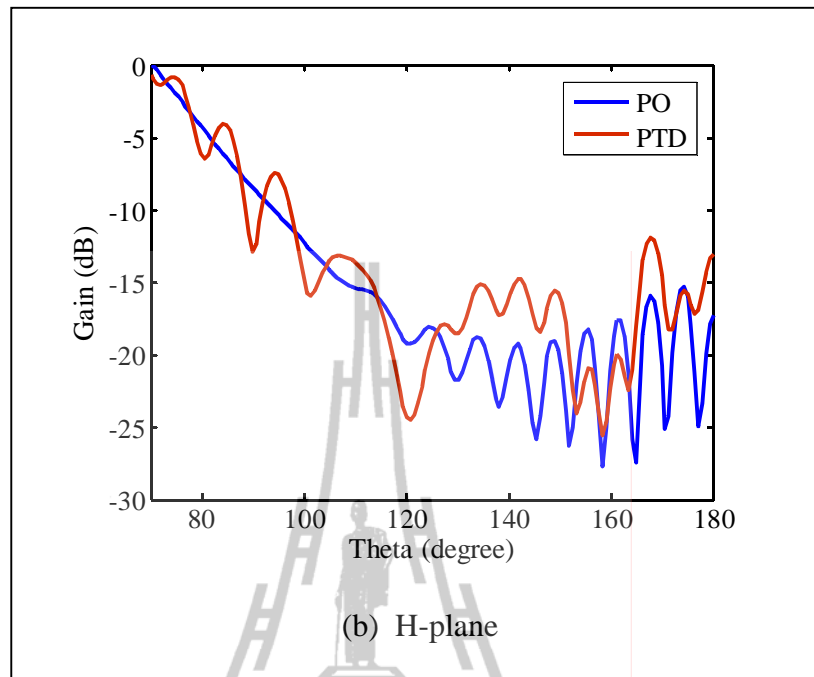


Figure 3.13 Close look at the rear pattern in E-and H-plane (Continued).

To verify the radiation characteristics, the experiment was set up at the frequency of 10 GHz to measure the E-and H-plane radiation patterns of quadratic reflector antenna. The quadratic reflector is duplicated to the curve surface by using the computer numerically controlled (CNC) machine. The prototype of a quadratic reflector antenna is shown in Figure 3.6(b). The far-field patterns of quadratic reflector antenna in the E-plane and H-plane pattern are compared with the simulated results, which are calculated by using PO and PTD as shown in Figure 3.14(a) and 3.14(b), respectively.

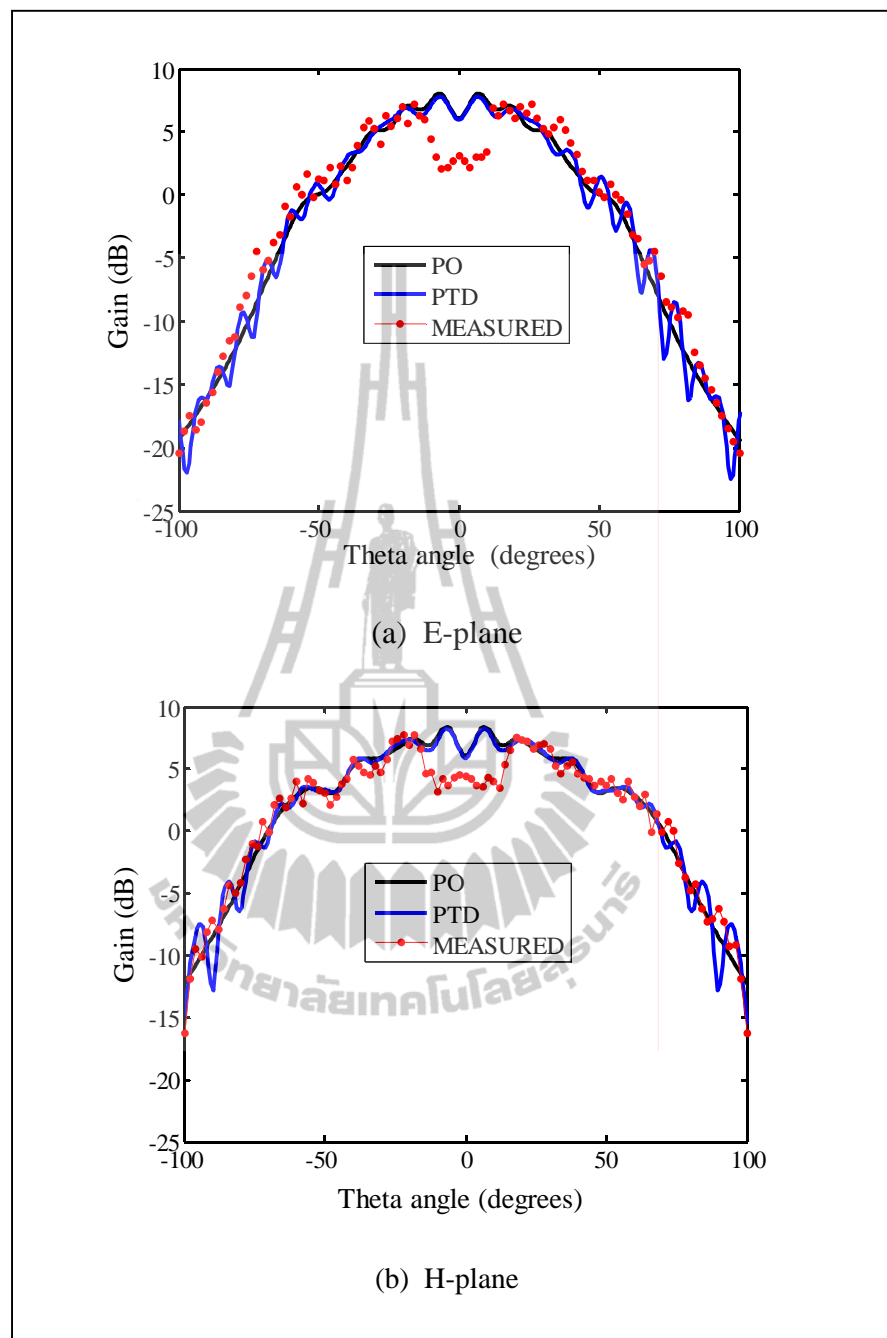


Figure 3.14 Far-field patterns of the quadratic reflector antenna.

Because of the feed blocking effect by simulation is neglected, therefore, the dip in pattern boresight from measurement of around 4 dB are occurred. Nevertheless, we found that the small ripple appears on the envelope of measured patterns, which are caused from some multipath effect that provided by construction of feed horn and metallic masts. Furthermore, if we compare the average levels on the all curves of each plane in far-angle region, it will be observed that a difference from measured pattern on the order of 1 dB approximately for PO and 0.3 dB for PTD. It is seen that PO predicts the field error more than PTD when compared its calculated results with measured results. This is attributed that no including the effects of edge diffraction into the field calculation by PO method. However, the agreement between simulated and measured results is satisfactory. In Table 3.1, the verification between simulation and experiment has been presented in the parameters of maximum gain and HPBW. The maximum gain of simulated results by using PO in the E-and H-planes pattern are higher than the measured results around 0.18 dB and 0.02 dB, respectively, while the maximum gains of simulation by using PTD are higher than the measured results around 0.13 dB and 0.01 dB, respectively. Besides that the measured results of HPBW are wider than the simulated results around 4° in E-plane and 2° in H-plane for PO and around 2° in E-plane and 1° in H-plane for PTD. Therefore, it can be summarized that the maximum gain and HPBW between simulated and measured results can show some minor differences both in the E- and H-plane patterns. An additional cause of asymmetry observed in the measured patterns is (the combination of) the small defocusing and mispointing of the feed, i.e., feed displacements and tilts.

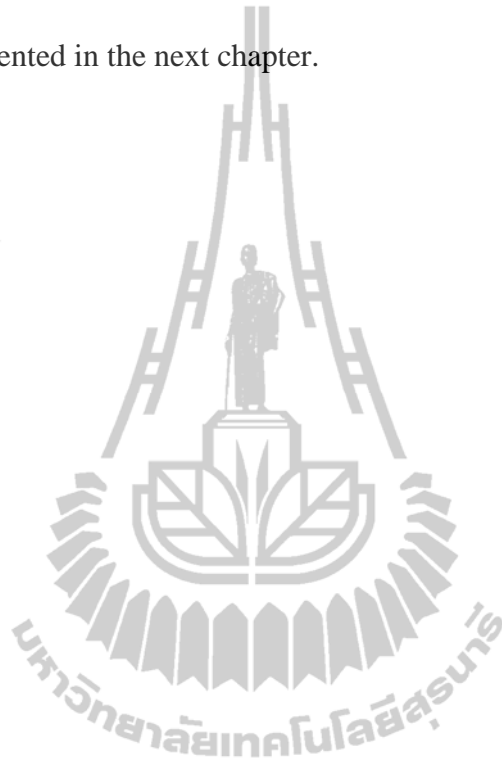
Table 3.1 Comparison of simulated and measured results for antenna characteristics.

Antenna characteristics	E-plane	H-plane
Maximum gain (PO)	8.20 dB	7.76 dB
Maximum gain (PTD)	8.05 dB	7.75 dB
Maximum gain (measured)	7.92 dB	7.74 dB
HPBW (PO)	66°	98°
HPBW (PTD)	68°	99°
HPBW (measured)	70°	100°

3.6 Chapter Summary

PO and PTD formulations are presented in this chapter. For the PO technique, the electric and magnetic fields can be obtained by the integration of a current distribution. The currents induced on the reflector surface are obtained directly from the components of incident fields tangential to the reflector at each point on its surface. These currents are then reradiated to the far-field to produce the patterns. PO is extended by PTD to include the diffraction field leading to more accurate calculation. These augmentations to cover diffraction effects from the rim of reflector increase the accuracy of the pattern beyond the main beam and in the far-angular region since the pattern in this region is dominated by diffraction effects. In addition, the numerical example for antenna analysis by using PO and PTD techniques were developed to solve the problems of single reflector antenna. The PO field was compared to the solution obtained from the PTD. It was found that the effect of PTD fringe field is important in the far-angular regions. It was cleared that the far-field

envelope predicted by PTD is higher than by PO. In the analysis of dual reflector antennas, electromagnetic energy emitted from the feed reflects on the subreflector and it advances toward the main reflector where it reflects again toward the out going field. The details of dual reflector antenna analysis, which focus on axially displaced ellipse will be presented in the next chapter.



CHAPTER IV

ANTENNA ANALYSIS AND DESIGN

4.1 Introduction

Reflector antennas are used in terrestrial and satellite communications, radar applications, and radio astronomy. Typically uses reflector antennas include radio links, satellite broadcasting and reception antennas, and radio telescopes. Reflector antennas are especially suitable for high gain narrow beam antennas with low side lobes. Reflector antennas can also be used for multiple beams and shape beams. The reflector surfaces used in reflector antennas are usually based on conic section such as parabolic, hyperbolic, elliptical, and spherical surfaces. Usually, parabolic antennas are used in applications where high gain is desired. The simplest antenna structure uses a front-fed parabolic with feed in the parabolic focus. It has the disadvantage that the feed and its support structure block antenna aperture. This blockage reduces the aperture efficiency and antenna gain. In addition, scattering from the feed structure increases sidelobe in the radiation pattern. Aperture blockage can be avoided by using an offset feed. However, the offset structure is mechanically more complicated and the asymmetrical structure causes cross polarization. To improve the performance of antenna radiation, the dual reflector antenna has been used in order to reduce spillover and sidelobe level and improve antenna gain. The basic dual reflector antennas are based on Cassegrain and Gregorian. However, the main disadvantage of these configurations is the subreflector blockage. This problem can be minimized by reduce the incidence of main reflector reflected rays upon subreflector. As describe in chapter

2, the axially symmetric dual reflector antennas that avoid the main reflector radiation toward the subreflector are considered. These antennas are characterized into four distinct types of axially symmetric dual reflector antenna i.e. axially displaced Crassegrain (ADC), axially displaced hyperbolic (ADH), axially displaced Gregorian (ADG), and axially displaced ellipse (ADE). It was found that the ADE provides high efficiency and a compact geometry, suitable for compact high gain spacecraft antenna applications (Prata et al., 2003). In the available literature, the main reflector of ADE antenna is parabolic and subreflector is portion of an ellipse. However, little information is available on the performance of the ADE configuration when the main reflector is not parabolic and backscattering technique to achieve wide beamwidth is used with main reflector. In this thesis, geometry of proposed antenna consists of a main reflector by using backscattering technique, portion of an ellipse subreflector and a conical horn antenna. The shape of main reflector is simple elementary geometrical equation such as quadratic and Gaussian (Thaiviroet et al., 2008).

This chapter presents analysis and design of ADE antenna. In the first section, the conical horn antenna which is used to be a feed of the ADE antenna is presented. Next section gives the details of the ADE reflector antenna such as antenna geometry and its advantages. The design and numerical examples of ADE reflector antenna, which are compared with both computational and experimental data published in the literature, have been conducted to justify the validity of the computer program. In section 4.4, the design and analysis of ADE backscatter antenna which is proposed antenna in this thesis will be presented. To represent the ADE backscatter antenna, several sets of input parameters representing various solutions have been considered. The radiation patterns of ADE backscatter antenna for the subreflector and the main

reflector are calculated by employing PO and PTD techniques. Representative examples will be presented to demonstrate the effectiveness of the PTD fringe field in the improving the PO field.

4.2 Conical (Corrugated) Horn Antenna

In this thesis, a conical horn has been used to be a feed of the antenna. The geometry of conical horn is shown in Figure 4.1. The first rigorous treatment of the fields radiated by a conical horn is that of Schorr and Beck (Schorr and Beck, 1950); (Balanis, 2005). The conical horn is a flared circular guide aperture, illuminated by the incident circular guide modes. The modes within the horn are found by introducing a spherical coordinate system and are in terms of spherical Bessel functions and Legendre polynomials. When the flare angle is small (less than 90 deg), the aperture fields can be approximated by the circular guide fields modified by the phase curvature introduced by the flare. In the case of the circular conical horn, the phase distortion is spherical, centered on the single apex of the cone (Diaz and Milligan, 1996).

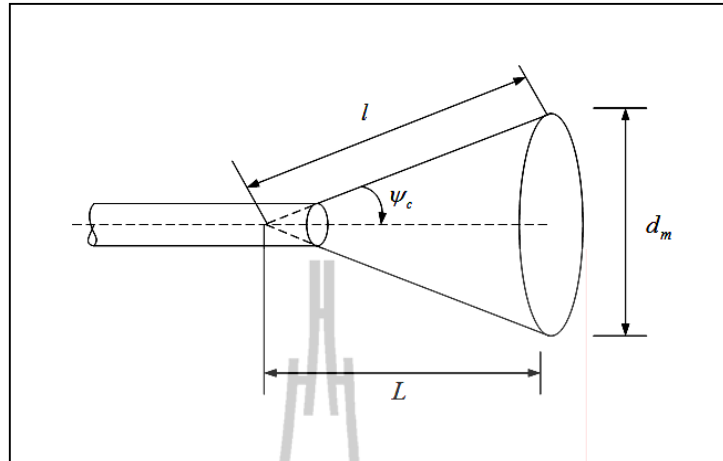


Figure 4.1 Geometry of conical horn (Balanis, 2005).

The incident modes are the TE and TM circular guide modes supported in the waveguide. Hybrid modes occur in dielectric-loaded or corrugated cylindrical region, along with TE, TM and hybrid EH modes. The HE_{11} mode consists of degenerate TE_{11} and TM_{11} modes in phase, and has symmetrical E- and H-plane pattern without sidelobes and excellent polarization purity. For a corrugated or dielectric-loaded circular horn with a reasonable flare angle, the aperture TM fields are given by Diaz and Milligan (1996) and Clarricoats and Olver (1984)

$$E_z = Z_0 \gamma J_n(k_{\rho nm} \rho) (A_p \cos(n\phi) + B_p \sin(n\phi)), \quad (4.1a)$$

$$E_\rho = -jZ_0 \gamma \frac{k_{znm}}{k_{\rho nm}} J'_n(k_{\rho nm} \rho) (A_p \cos(n\phi) + B_p \sin(n\phi)), \quad (4.1b)$$

$$E_\phi = -jZ_0 \gamma \frac{k_{znm}}{k_{\rho nm}^2} \frac{n}{\rho} J_n(k_{\rho nm} \rho) (B_p \cos(n\phi) - A_p \sin(n\phi)). \quad (4.1c)$$

The TE fields are

$$E_z = 0, \quad (4.2a)$$

$$E_\rho = -j \frac{\omega\mu}{k_{\rho nm}^2} \frac{n}{\rho} J_n(k_{\rho nm} \rho) (A_p \cos(n\phi) + B_p \sin(n\phi)), \quad (4.2b)$$

$$E_\phi = j \frac{\omega\mu}{k_{\rho nm}} J_n'(k_{\rho nm} \rho) (-B_p \cos(n\phi) + A_p \sin(n\phi)). \quad (4.2c)$$

The Bessel function of the first kind of order n and its derivative with respect to its argument are given by $J_n(u)$ and $J_n'(u)$, respectively. The order n is the circumferential mode number and represents the number of half-wavelength field variations around the circumference of the circular waveguide. The radial wavenumber $k_{\rho nm}$ is the m th root of the characteristic equation for hybrid modes,

$$F = \frac{k_\rho R \omega\mu}{k_z n Z_0} \frac{J_n'(k_\rho R)}{J_n(k_\rho R)} + \frac{X_s \frac{k_z}{k_\rho^2} \frac{n}{R} J_n(k_\rho R)}{Z_0 J_n(k_\rho R) - X_s \frac{k_0}{k_\rho} J_n'(k_\rho R)} = 0, \quad (4.3)$$

which is function of the reactance of the corrugated horn or dielectric-coated walls X_s and the radius of the circular waveguide aperture, R . Since the corrugated surface is assumed to be lossless, the surface impedance is purely imaginary. The reactance is

$$X_s = Z_0 \tan(k_0 d), \quad (4.4)$$

where Z_0 is impedance of free space, k_0 is wavenumber, and d is dielectric thickness.

Once (4.4) is solved for the appropriate $k_{\rho nm}$, the hybrid mode ratio γ is obtained with

$$\gamma = \mp \frac{k_\rho k_0 R J'_n(k_{\rho nm} R)}{k_z n J_n(k_{\rho nm} R)}, \quad (4.5)$$

where the minus sign corresponds to the HE modes and the plus sign corresponds to EH modes. The axial wavenumber is given by

$$k_{znm} = \sqrt{k_0^2 - k_{\rho nm}^2}. \quad (4.6)$$

The coefficients A_p and B_p specify the relative amplitudes of the sinusoidal and cosinusoidal circumferentially varying fields.

The radiation pattern of a 3.175λ , 28.43° flare angle corrugated horn is shown in Figure 4.2. The corrugations are assumed to be a quarter wavelength deep, presenting an infinite surface reactance to the conical region fields. The radiation pattern of corrugated conical horn has symmetrical E- and H-plane without sidelobes.

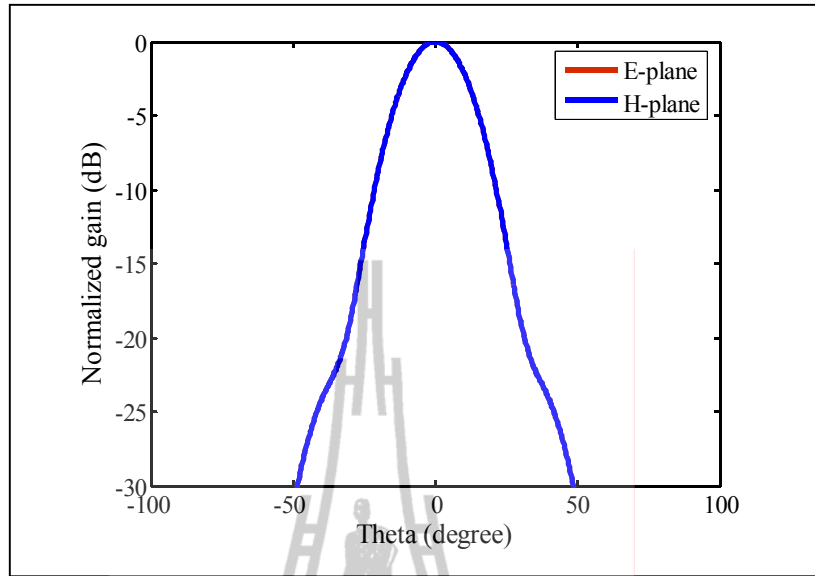


Figure 4.2 Radiation pattern of corrugated conical horn.

The case of conical horn (smooth wall horn) provides the zero of the Bessel function associated with the mode is known. The radial propagation constant is (Bessel function zero)/radius. The aperture fields are given by

$$E_{\rho} = \left[-V_M \frac{jZ_0}{k_{\rho nm}} (k_{z nm} J'_n(k_{\rho nm} \rho)) + V_E \frac{k_0 n}{k_{\rho nm} \rho} J_n(k_{\rho nm} \rho) \right] \times (A_p \cos(n\phi) + B_p \sin(n\phi)) \quad (4.7a)$$

$$E_{\phi} = \left[-V_M \frac{jZ_0}{k_{\rho nm}} \left(\frac{k_{z nm} n}{k_{\rho nm} \rho} J_n(k_{\rho nm} \rho) \right) + V_E k_{z nm} J'_n(k_{\rho nm} \rho) \right] \times (B_p \cos(n\phi) - A_p \sin(n\phi)) \quad (4.7b)$$

The TE mode currents for a smooth wall conical horn can be found by setting $V_E = 1$ and $V_M = 0$ and by using the zero of the derivative of the Bessel function $J'_n(k_{\rho nm}R)$ to find the radial propagation constant,

$$k_{\rho nm} = x'_{nm} / \text{Radius}. \quad (4.8)$$

The TM mode can be entered in a similar manner by using $V_E = 0$ and $V_M = 1$ and using the zero of the Bessel function for the radial propagation constant. In this thesis has used conical horn for TE₁₁ mode to be feed of the antenna. The details of the design procedure for a conical horn antenna are described in appendix A. The radiation pattern of a 3.175λ , 28.43° flare angle conical horn is shown in Figure 4.3.

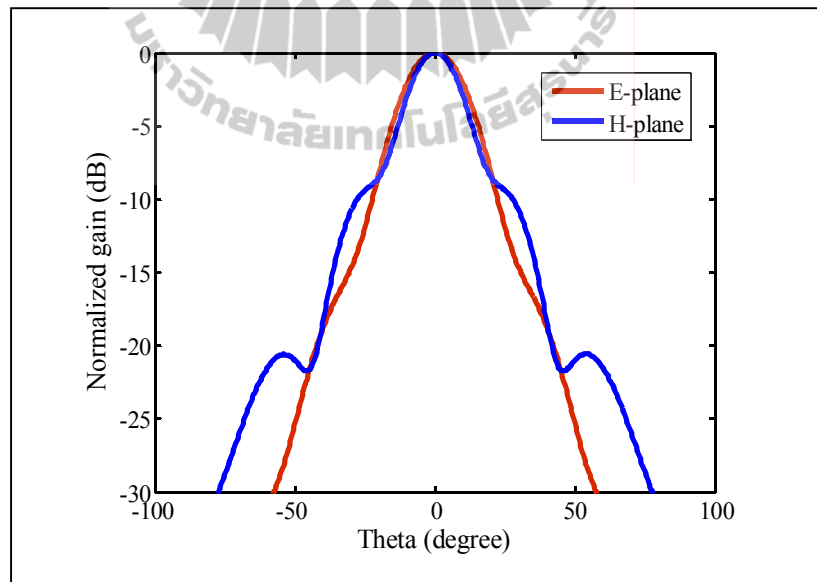


Figure 4.3 Radiation pattern of conical horn antenna.

4.3 Axially Displaced Ellipse Reflector Antenna

An alternative dual reflector antenna design that minimizes several of the problems described above is the axially displaced ellipse reflector antenna or ADE reflector antenna geometry. ADE reflector antenna may be considered as a special case of the generalized Gregorian system, in which the focal axis of the main parabolic is displaced from the axis of symmetry, which contains the prime focus of the ellipse subreflector. The locus of the secondary foci of the subreflector forms a ring through which all the ray pass, which coincides with that of the main reflector as shown in Figure 4.4. The parameters of the ellipse and the parabolic are chosen so that the central ray from the prime focus reaches the outer edge of the main reflector while the inner ray clears the outer edge of the subreflector after reflection from the main reflector. Advantages of the ADE antenna are:

- (1) The rays are not reflected into the feed horn from the subreflector nor back into the subreflector from the main reflector. Also, the aperture illumination for the radiated wave is more uniform than in the standard Cassegrain or Gregorian configuration: all emitted rays miss the subreflector, leading to the higher aperture efficiency.

- (2) Because of the displaced axis geometry, there is no blockage by the subreflector, and this property also improves the feed mismatch caused by the reflection from the subreflector. It also permits the use of a smaller subreflector in close proximity to the feed, reducing rear radiation.

- (3) The main reflector can be made considerably smaller than the conventional design, leading the compact antenna design with reduction in far-out sidelobes.

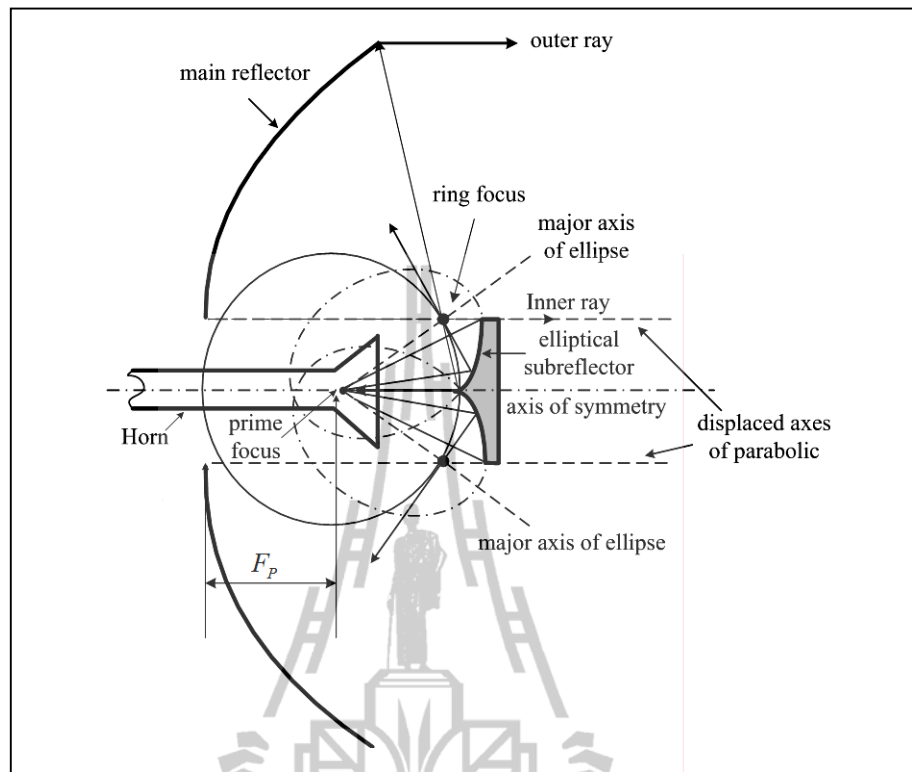


Figure 4.4 ADE reflector antenna geometry.

4.4 Design Examples of Axially Displaced Ellipse Reflector Antenna

In dual reflector geometry, it is customary to define the main reflector in $(O_{MR}, X_{MR}, Y_{MR}, Z_{MR})$ coordinate system and subreflector in $(O_{SR}, X_{SR}, Y_{SR}, Z_{SR})$ coordinate system and to have a symmetry antenna coordinate system (G, X, Y, Z) in which the main reflector and subreflector are finally expressed. Note that the antenna arrangements are proposed, $O_{MR} \equiv O_{SR} \equiv O$.

The design procedure of ADE reflector antenna in this section is based on (Granet, 1999). The cross section view of ADE reflector antenna as shown in Figure 4.5, the main reflector is parabolic and subreflector is a portion of an ellipse.

Antenna geometry is defined with a system of eight input parameters, namely:

$D_m, F, D_s, \theta_e, L_m, L_s, a$, and f , where (see Figures. 4.5 to 4.7):

D_m : diameter of the main parabolic reflector,

F : focal distance of the main reflector,

D_s : diameter of the elliptical subreflector,

θ_e : angle between the Z axis and the ray emanating from the focus, F_0 , of the antenna in the direction of the subreflector edge,

L_m : distance between the focus, F_0 , of the antenna and the projection of the bottom-edge of the half-main-reflector onto the Z axis,

L_s : distance between the focus, F_0 , of the antenna and the apex of the subreflector,

a and f : parameters defining the geometry of the subreflector.

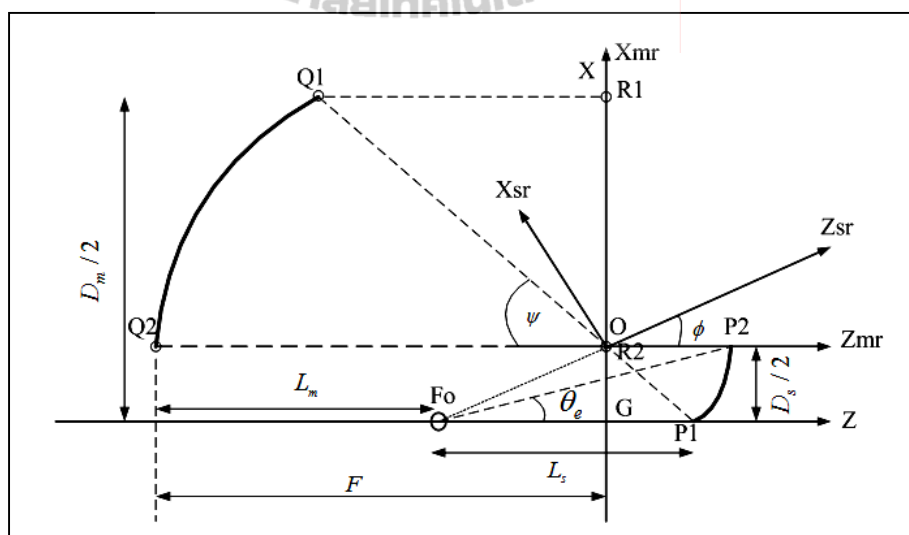


Figure 4.5 A cross-section view of a the axially displaced ellipse antenna system.

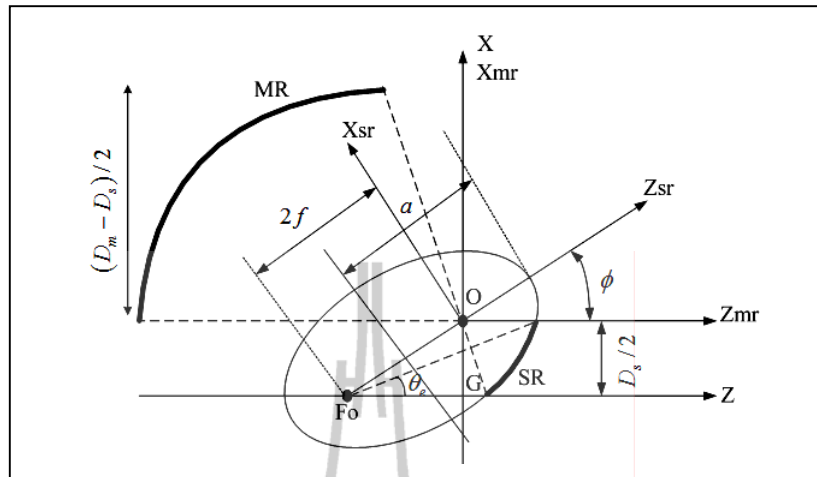


Figure 4.6 Cross-sectional view of the elliptical-subreflector coordinate system with its parameters.

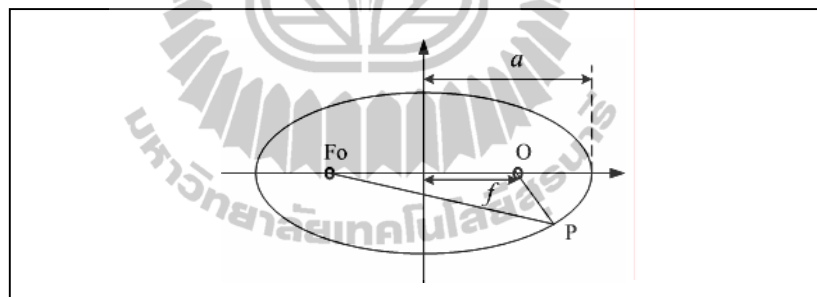


Figure 4.7 Distance relationship in an ellipse.

For the definition of the main reflector geometry, only the upper part of the (O_{MR}, X_{MR}, Z_{MR}) plane is considered. The parabolic main reflector profile, $z_{mr}(x_{mr})$, depends on the real parameter F and its equation is expressed by

$$z_{mr}(x_{mr}) = \frac{(x_{mr})^2}{4F} - F, \quad (4.9)$$

$$0 \leq x_{mr} \leq \frac{D_m - D_s}{2}. \quad (4.10)$$

The elliptical subreflector profile, $z_{sr}(x_{sr})$, is defined in the (O_{SR}, X_{SR}, Z_{SR}) plane and depends on the two real parameters a and f . The equation of elliptical subreflector is of the form

$$z_{sr}(x_{sr}) = a \sqrt{1 + \frac{(x_{sr})^2}{f^2 - a^2}} - f. \quad (4.11)$$

In the case of ellipsoid, we have possibilities $a > f > 0$. The parameter f is the half distance between the foci, and a is the half major axis of the ellipse. The eccentricity is $e = \frac{f}{a}$. x_{sr} is expressed in the main reflector coordinate system as

$$\frac{-D_s}{2} \leq [x_{sr}]_{\text{Expressed in the MR coordinate system}} \leq 0. \quad (4.12)$$

The subreflector can express in the main reflector coordinate system by using the angle ϕ and then express both main reflector and subreflector in the antenna coordinate system (G, X, Y, Z) . The antenna has a circularly symmetric shape and spinning this geometry around the antenna axis of symmetry produces three-dimensional of ADE reflector antenna. In designing the antennas, there are two main properties of the Gregorian system:

(1) The path length is the same for any ray from the focus, F_0 , to the aperture, i.e., using the extreme rays, thus

$$\|F_0P_1\| + \|P_1Q_1\| + \|Q_1R_1\| = \|F_0P_2\| + \|P_2Q_2\| + \|Q_2R_2\|. \quad (4.13)$$

(2) The distance relationship in an ellipse gives (Brown and Prata, 1994)

$$\|F_0P\| + \|OP\| = 2a. \quad (4.14)$$

To design the ADE reflector antenna, we have to know the parameters i.e. $D_m, F, D_s, \theta_e, L_m, L_s, a$, and f . Because these parameters can not be specified arbitrarily, therefore, five input parameters i.e. D_m, A, D_s, L and θ_e are chosen to define the antenna. Then, using the fact that the path length is the same for any ray from the focus to aperture, along with formulas related to paraboloid and ellipsoid, the remaining design parameters in terms of these input parameters can obtain by

$$L_m = \frac{FD_m}{D_m - D_s} - \frac{D_s}{4} \left[\frac{\cos(\theta_e) + 1}{\sin(\theta_e)} \right], \quad (4.15)$$

$$\tan(\phi) = \frac{2}{\frac{\cos(\theta_e) + 1}{\sin(\theta_e)} - \frac{4F}{D_m - D_s}}, \quad (4.16)$$

$$f = \frac{D_s}{4\sin(\phi)}, \quad (4.17)$$

$$\tan(\psi) = \frac{8F(D_m - D_s)}{(D_m - D_s)^2 - 16F^2}, \quad (4.18)$$

$$L_s = 2f \cos(\phi) + \frac{D_s}{2 \tan(\psi)}, \quad (4.19)$$

$$a = \frac{D_s}{8} \left[\frac{\cos(\theta_e) + 1}{\sin(\theta_e)} \right] + \frac{FD_s}{2(D_m - D_s)}. \quad (4.20)$$

Now, all the parameters necessary for representing the ADE reflector antenna system are defined. The numerical example of the ADE reflector antenna is presented in this section. A computer program by using Matlab is developed to perform analysis radiation pattern of ADE reflector antenna. The numerical simulation, which is compared with computational data published in the literature such as Granet (1999) and Kumar (2009), has been conducted to justify the validity of the program. Representative examples are presented in the following.

In the first example, the geometry of ADE reflector antenna system is shown in Figure 4.8, where a parabolic main reflector is used in conjunction with a portion of an ellipse subreflector. To justify the validity of the program, this analysis is compared with Granet (1999) with the same input parameters of ADE reflector antenna. Granet analyzed and designed antenna at 3.8 GHz (using physical optics on both reflectors, and assuming a theoretical Gaussian feed). The antenna has been designed by using input parameters i.e. $D_m = 8$ m, $F = 4.7$ m, $D_s = 1.2$ m and $\theta_e = 15^\circ$. The remaining design parameters in terms of these input parameters can be obtained by using (4.15)-(4.20), thus $L_m = 3.2506$ m, $L_s = 2.1702$ m, $a = 1.554$ m and

$f = 0.7843$ m. A corrugated conical horn as described in section 4.2 has been used to be feed of the antenna. Physical optics is used to analyze radiation pattern of ADE antenna on both reflectors and compared with Granet work.

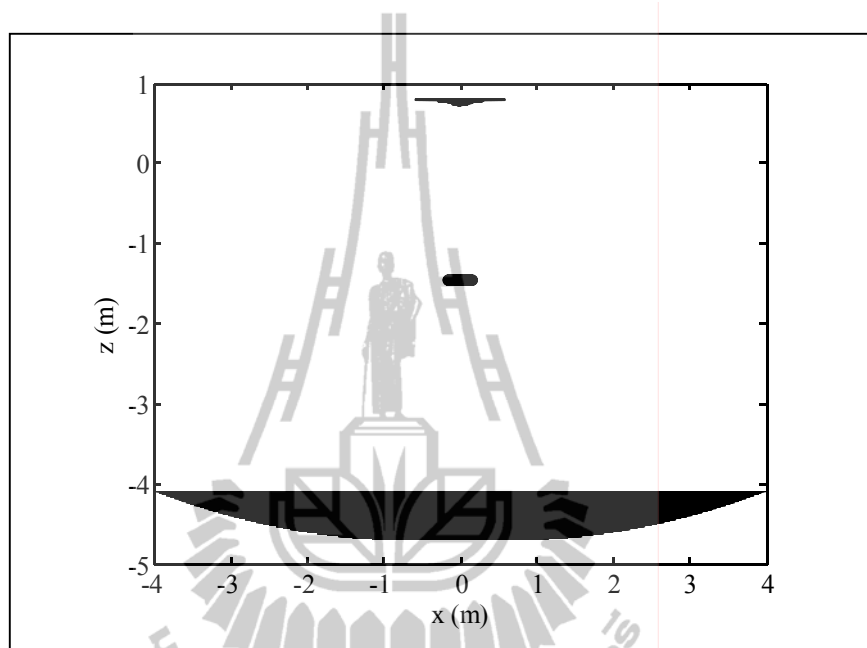


Figure 4.8 The ADE antenna geometry, $D_m = 8$ m, $F = 4.7$ m, $L_m = 3.2506$ m,

$$D_s = 1.2 \text{ m}, L_s = 2.1702 \text{ m}, a = 1.554 \text{ m}, f = 0.7843 \text{ m}, \theta_e = 15^\circ.$$

The simulated radiation pattern of ADE reflector antenna, which based on the developed PO analysis tool by using Matlab is plotted together with the simulated pattern, which was developed by Granet (1999) as expressed in Figure 4.9. This plot shows good agreement between both simulated radiation patterns. However, small different in the radiation pattern is cause of the different in the feed system, which is used in simulation.

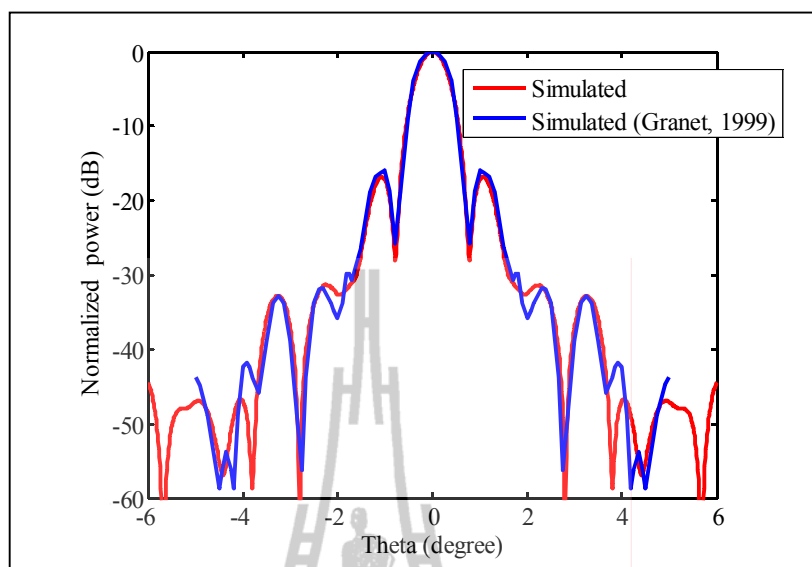


Figure 4.9 Radiation pattern of ADE reflector antenna compare with Granet (1999).

The example of ADE reflector antenna as described above has been analyzed by using PO at the frequency of 3.8 GHz. In order to consider ADE reflector antenna performance, we will compare radiation pattern of ADE reflector antenna with the front-feed single reflector antenna and classical Cassegrain dual reflector antenna as shown in Figures 4.10 and 4.11. The radiation patterns of front-feed single reflector antenna, classical Cassegrain dual reflector antenna and ADE reflector are shown in Figures 4.12 to 4.14, respectively. It was found that the antenna gain of single reflector antenna, classical Cassegrain dual reflector antenna and ADE reflector antenna are around 41 dB, 48 dB, and 49 dB, respectively, corresponding to the antenna radiation efficiency of 12%, 62%, and 78%, respectively. The main conclusion of this analysis is that the ADE reflector antenna offers better gain and radiation efficiency. On the other hand, the radiation pattern first sidelobe for the ADE reflector antenna is higher than for the classical Cassegrain systems.

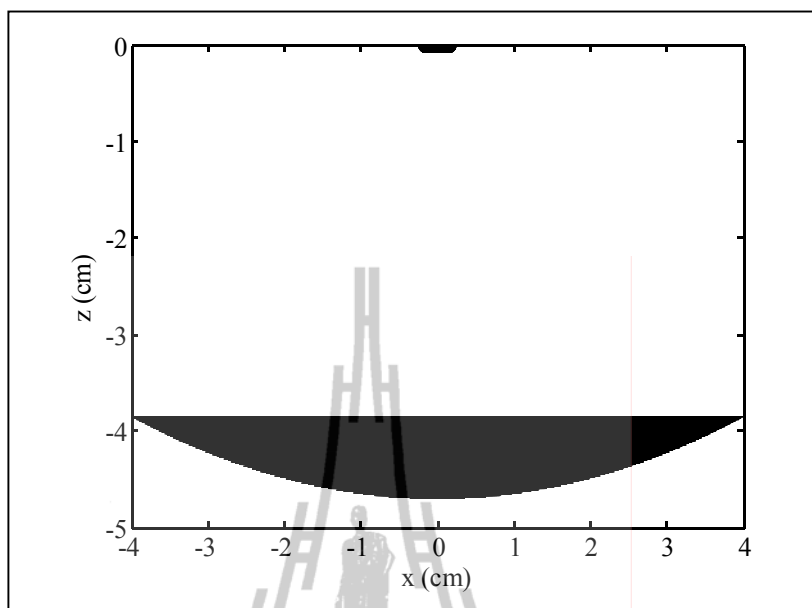


Figure 4.10 Geometry of front-feed single reflector antenna
with $D_m = 8$ m and $F = 4.7$ m.

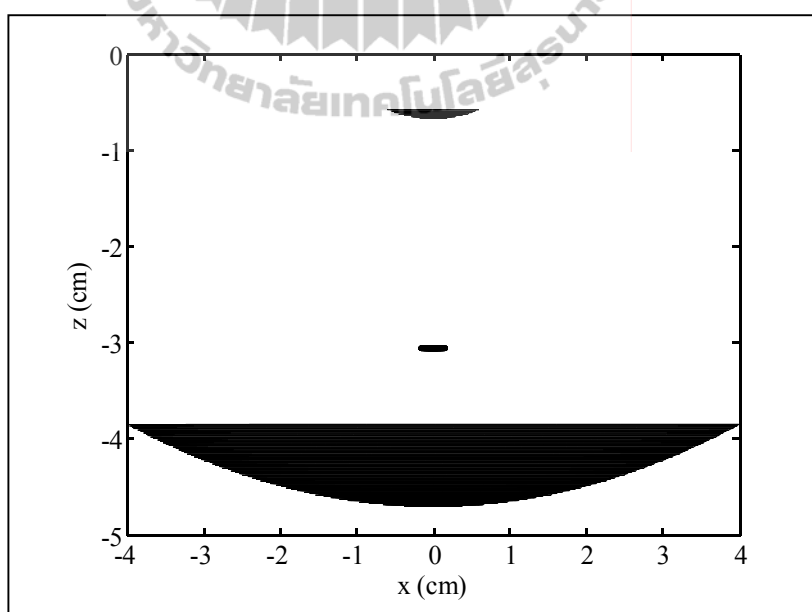


Figure 4.11 Geometry of classical Cassegrain dual reflector antenna
with $D_m = 8$ m, $D_s = 1.2$ m and $F = 4.7$ m.

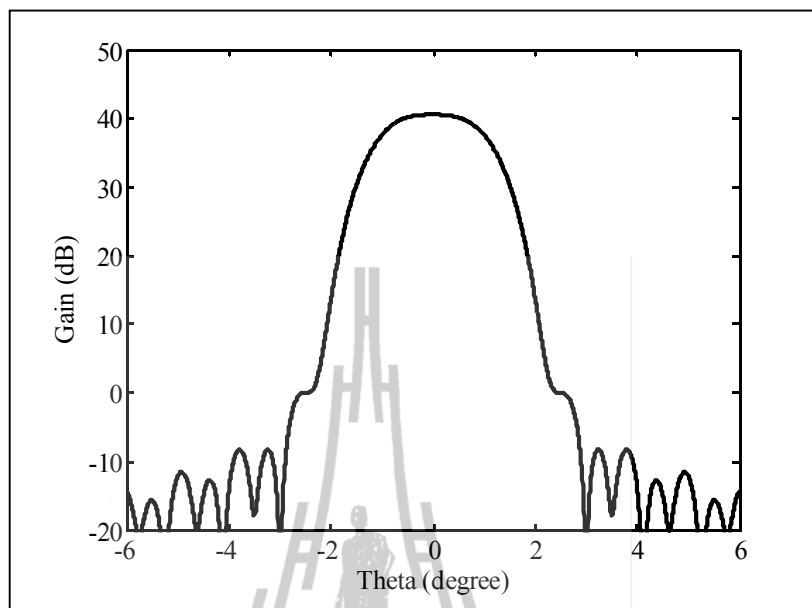


Figure 4.12 Radiation pattern of front-feed single reflector antenna.

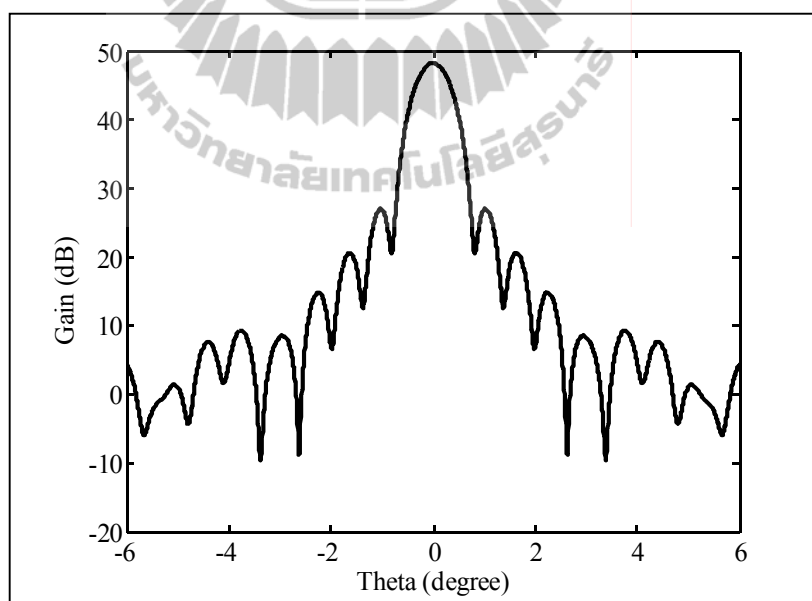


Figure 4.13 Radiation pattern of classical Cassegrain dual reflector antenna.

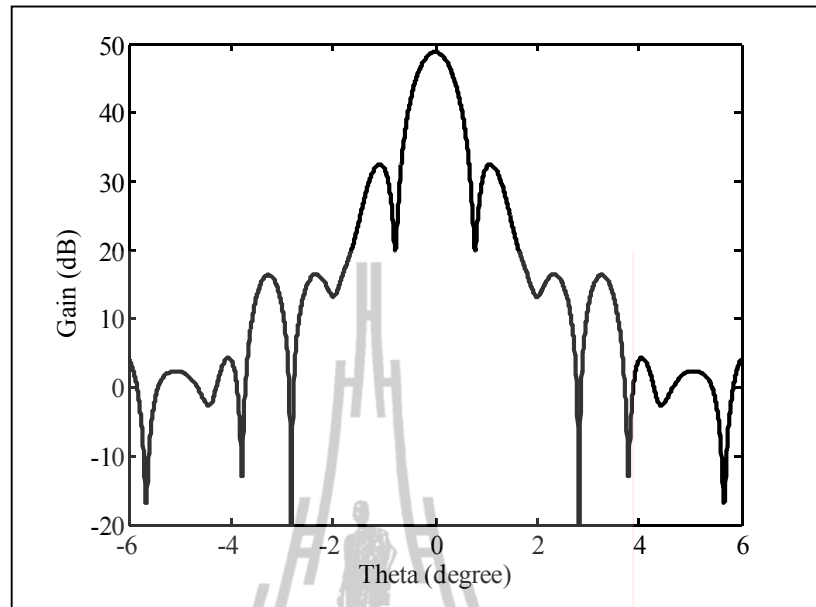


Figure 4.14 Radiation pattern of ADE reflector antenna.

In the next example, the ADE reflector antenna geometry with an electrically small aperture and its prototype are illustrated in Figure 4.15 and Figure 4.16, respectively. This antenna geometry was constructed by Kumar et al (1999). They analyzed and designed the ADE antenna at 8.484 GHz (the performance of the ADE antenna has been simulated in the commercially available reflector analysis program GRASP-9 from TICRA). A corrugated conical horn having symmetric radiation has been used to be feed of the antenna. The antenna has been designed using input parameters, $D_m = 70$ cm, $F = 18$ cm, $D_s = 7$ cm, and $\theta_e = 25^\circ$. The remaining design parameters in terms of these input parameters can be obtained by (4.15)-(4.20), found that $L_m = 12.1063$ cm, $L_s = 6.3625$ cm, $a = 4.9469$ cm, and $f = 3.4273$ cm. Physical optics is used to analyze radiation pattern of ADE antenna on both reflectors and compared with Kumar work.

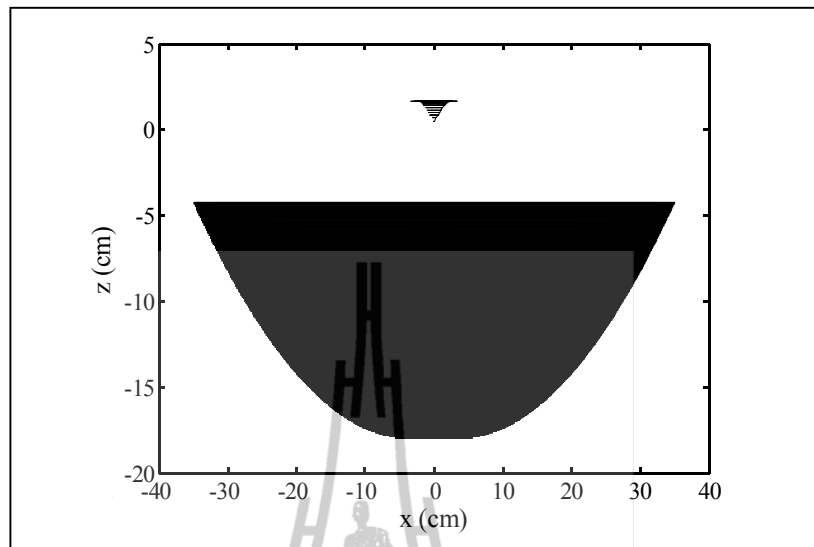


Figure 4.15 The ADE antenna geometry, $D_m = 70$ cm, $F = 18$ cm, $L_m = 12.1063$ cm,

$$D_s = 7 \text{ cm}, L_s = 6.3625 \text{ cm}, a = 4.9469 \text{ cm}, f = 3.4273 \text{ cm}, \theta_e = 25^\circ.$$

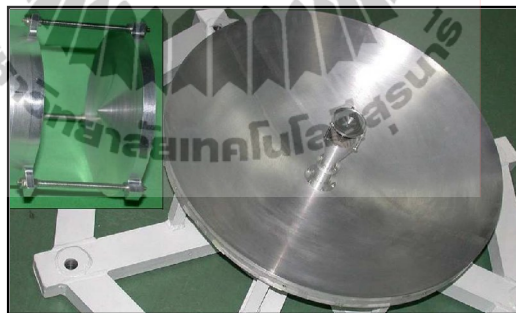


Figure 4.16 Photograph of the realized 70 cm diameter ADE antenna. Enlarged view of the subreflector is shown in the inset (Kumar et al., 2009).

The simulated radiation pattern of the ADE antenna without any studs, which is simulated by using PO on both reflectors is compared with radiation pattern of Kumar et al. (2009), which was simulated by using commercially analysis program GRASP-9. The measured radiation pattern by Kumar et al. (2009) is plotted together

with the simulated pattern as shown in Figure 4.17. This plot depicts very good agreement between the measured and simulated pattern. The small different between simulated and measured result is cause of simulation is without any studs, while the measurement is with studs. The results from the presented examples provide the confidence that the PO, which is developed by computer program, is accurate for prediction the field.

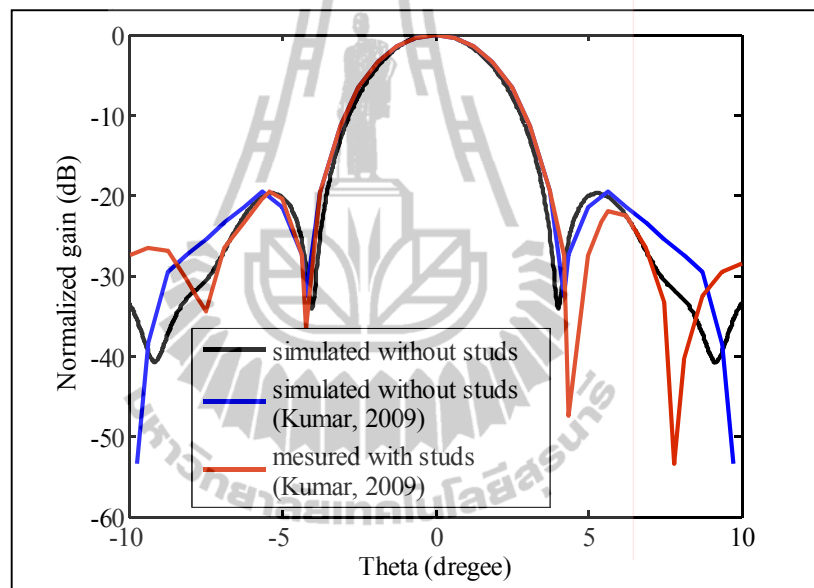


Figure 4.17 Radiation pattern of ADE reflector antenna compare with (Kumar, 2009).

4.5 Axially Displaced Ellipse Backscatter Antenna

4.5.1 Design of Axially Displaced Ellipse Backscatter Antenna

The geometry of axially displaced ellipse backscatter antenna, which is proposed antenna in this thesis, is shown in Figure 4.18. The antenna has axial symmetry. The curvature of main reflector is Gaussian, and the subreflector is a

portion of an ellipse. The three dimensional reflector surface is yielded by spinning the generating curve around the z-axis (symmetry axis). The design procedure is same in the section 4.4 and based on Granet (1999), where, again, we are dealing with a system of nine parameters defining the overall geometry of the antenna. These parameters i.e. $D_m, L, A, D_s, \theta_e, L_m, L_s, a,$ and f (see Figs. 4.18 to 4.19) where

D_m : diameter of the main reflector,

L : distance between point, F_0 , of the antenna and the projection of the bottom-edge of the half-main-reflector onto the axis,

D_s : diameter of the elliptical subreflector,

A : parameter to define the convexity of the main reflector,

θ_e : angle between the Z axis and the ray emanating from the point, F_0 , of the antenna in the direction of the subreflector edge,

L_m : distance between the point, F_0 , of the antenna and the projection of the top-edge of the half-main-reflector onto the Z axis,

L_s : distance between the point, F_0 , of the antenna and the apex of the subreflector,

a and f : parameters defining the geometry of the subreflector.

The main reflector is Gaussian equation as shown in (4.21). The subreflector is the portion of an ellipse as expressed in (4.22)

$$z_{mr}(x_{mr}) = Ae^{-\frac{2}{D_m}x_{mr}^2} - L, \quad (4.21)$$

$$z_{sr}(x_{sr}) = a\sqrt{1 + \frac{(x_{sr})^2}{f^2 - a^2}} - f. \quad (4.22)$$

Taking into account all of these factors, several sets of input parameters representing various solutions have been considered. In this thesis, we will consider eight sets of input parameters. From these input parameters and using distance relationship in an ellipse in (4.14), the overall parameters of the antenna are derived in close form. Table 4.1 presents eight cases where five input parameters are used, and the unknown parameters are determined. List of equations for eight case of input parameters are:

Set 1: Input parameters are D_m , L , A , D_s , and θ_e , which unknown parameters are in the form

$$\tan(\psi) = \frac{(D_m - D_s)}{2L}, \quad (4.23)$$

$$\tan(\phi) = \left[\frac{2}{\frac{\cos(\theta_e) + 1}{\sin(\theta_e)} - \frac{\cos(\psi) + 1}{\sin(\psi)}} \right], \quad (4.24)$$

$$a = \frac{D_s}{8} \left[\frac{\cos(\theta_e) + 1}{\sin(\theta_e)} + \frac{\cos(\psi) + 1}{\sin(\psi)} \right], \quad (4.25)$$

$$f = \frac{D_s}{4 \sin(\phi)}, \quad (4.26)$$

$$L_m = L - \frac{D_s}{4} \left[\frac{\cos(\theta_e) + 1}{\sin(\theta_e)} - \frac{\cos(\psi) + 1}{\sin(\psi)} \right] + A, \quad (4.27)$$

$$L_s = 2f \cos(\phi) + \frac{D_s}{2 \tan(\psi)}. \quad (4.28)$$

Set 2: Input parameters are D_m , A , L_m , L_s , and θ_e , which unknown parameters are in the form

$$\tan(\psi) = \frac{D_m}{2(L_m + L_s)}, \quad (4.29)$$

$$D_s = \frac{2 \left(L_s - L_m + \frac{D_m}{2 \tan \psi} \right)}{\left[\left(\frac{1 + \cos \theta_e}{\sin \theta_e} \right) + \left(\frac{\cos \psi - 1}{\sin \psi} \right) \right]}, \quad (4.30)$$

$$L = \frac{D_m - D_s}{2 \tan \psi}. \quad (4.31)$$

$\tan \phi$, a and f can be calculated by using (4.24), (4.25), (4.26), respectively.

Set 3: Input parameters are $D_m, L, A, L_m,$ and $\theta_e,$ which unknown parameters are in the form

$$\psi = \text{root of } \left\{ \begin{array}{l} \left(4(L - L_m) - \left(\frac{\cos \theta_e + 1}{\sin \theta_e} \right) D_m \right) Z^3 \\ + \left(D_m - 4L \left(\frac{\cos \theta_e + 1}{\sin \theta_e} \right) \right) Z^2 \\ + \left(4L + D_m \left(\frac{\cos \theta_e + 1}{\sin \theta_e} \right) - 4(L - L_m) \right) Z - D_m = 0 \end{array} \right\}, \quad (4.32)$$

where $Z = \tan \frac{\psi}{2}$ and the solution of ψ can be calculated by defining absolute of ψ is minimum.

$$D_s = D_m - 2L \tan \psi \quad (4.33)$$

$$L_s = \frac{D_s}{4} \left[\left(\frac{\cos \theta_e + 1}{\sin \theta_e} \right) - \left(\frac{1 - \cos \psi}{\sin \psi} \right) \right] \quad (4.34)$$

$\tan \phi, a$ and f can be calculated by using (4.24), (4.25), (4.26), respectively.

Set 4: Input parameters are $D_m, A, L_m, D_s,$ and $\theta_e,$ which unknown parameters are in the form

$$\psi = \text{root of } \left\{ \begin{array}{l} (D_s - D_m) Z^2 + \left(-4L_m - \left(\frac{\cos \theta_e + 1}{\sin \theta_e} \right) D_s \right) Z \\ + D_m = 0 \end{array} \right\}, \quad (4.35)$$

where $Z = \tan \frac{\psi}{2}$ and the solution of ψ can be calculated by defining absolute of ψ is minimum.

$$L = L_m + \frac{D_s}{4} \left[\left(\frac{\cos \theta_e + 1}{\sin \theta_e} \right) - \left(\frac{\cos \psi + 1}{\sin \psi} \right) \right] \quad (4.36)$$

$$L_s = \frac{D_m}{2 \tan \psi} - L_m \quad (4.37)$$

$\tan \phi$, a and f can be calculated by using (4.24), (4.25), (4.26), respectively.

Set 5: Input parameters are L , A , D_s , L_s , and θ_e , which unknown parameters are in the form

$$\psi = 2 \left\{ \tan^{-1} \left[\left(\frac{\cos \theta_e + 1}{\sin \theta_e} \right) - \frac{4L_s}{D_s} \right] \right\}, \quad (4.38)$$

$$L_m = L - \frac{D_s}{4} \left[\left(\frac{\cos \theta_e + 1}{\sin \theta_e} \right) - \left(\frac{\cos \psi + 1}{\sin \psi} \right) \right], \quad (4.39)$$

$$D_m = 2(L_m + L_s) \tan \psi. \quad (4.40)$$

$\tan \phi$, a and f can be calculated by using (4.24), (4.25), (4.26), respectively.

Set 6: Input parameters are A , D_s , L_m , L_s , and θ_e , which unknown parameters are in the form

$$\psi = 2 \left\{ \tan^{-1} \left[\left(\frac{\cos \theta_e + 1}{\sin \theta_e} \right) - \frac{4L_s}{D_s} \right] \right\}, \quad (4.41)$$

$$D_m = 2(L_m + L_s) \tan \psi, \quad (4.42)$$

$$L = L_m + \frac{D_s}{4} \left[\left(\frac{\cos \theta_e + 1}{\sin \theta_e} \right) - \left(\frac{\cos \psi + 1}{\sin \psi} \right) \right]. \quad (4.43)$$

$\tan \phi$, a and f can be calculated by using (4.24), (4.25), (4.26), respectively.

Set 7: Input parameters are D_m , A , L , L_s , and θ_e , which unknown parameters are in the form

$$\psi = \text{root of} \left\{ \begin{array}{l} D_m Z^3 + \left(4L + 4L_s - \left(\frac{\cos \theta_e + 1}{\sin \theta_e} \right) D_m \right) Z^2 \\ + \left(-D_m - 4 \left(\frac{\cos \theta_e + 1}{\sin \theta_e} \right) L \right) Z \\ + \left(\left(\frac{\cos \theta_e + 1}{\sin \theta_e} \right) D_m - 4L_s \right) = 0 \end{array} \right\}, \quad (4.44)$$

where $Z = \tan \frac{\psi}{2}$ and the solution of ψ can be calculated by defining absolute of ψ

is minimum.

$$D_s = D_m - 2L \tan \psi \quad (4.45)$$

$$L_m = \frac{D_m}{2 \tan \psi} - L_s \quad (4.46)$$

$\tan \phi$, a and f can be calculated by using (4.24), (4.25), (4.26), respectively.

Set 8: Input parameters are D_m , D_s , A , L_s , and θ_e , which unknown parameters are in the form

$$\psi = 2 \left\{ \tan^{-1} \left[\left(\frac{\cos \theta_e + 1}{\sin \theta_e} \right) - \frac{4L_s}{D_s} \right] \right\}, \quad (4.47)$$

$$L_m = \frac{D_m}{2 \tan \psi} - L_s, \quad (4.48)$$

$$L = L_m + L_s - \frac{D_s}{2 \tan \psi}. \quad (4.49)$$

$\tan \phi$, a and f can be calculated by using (4.24), (4.25), (4.26), respectively.

We have now defined all the solution of eight sets input parameters for representing the ADE backscatter antenna. This procedure allows the antenna designer to fully define the antenna geometry with different sets of input parameters, depending on the requirements of the antenna size and performance.

Table 4.1 Eight cases where five input parameters are used.

Parameters	D_m	L	A	D_s	a	f	L_m	L_s	θ_e
Set No.1	D_m	L	A	D_s	(4.25)	(4.26)	(4.27)	(4.28)	θ_e
Set No.2	D_m	(4.31)	A	(4.30)	(4.25)	(4.26)	L_m	L_s	θ_e
Set No.3	D_m	L	A	(4.33)	(4.25)	(4.26)	L_m	(4.34)	θ_e
Set No.4	D_m	(4.36)	A	D_s	(4.25)	(4.26)	L_m	(4.37)	θ_e
Set No.5	(4.40)	L	A	D_s	(4.25)	(4.26)	(4.39)	L_s	θ_e
Set No.6	(4.42)	(4.43)	A	D_s	(4.25)	(4.26)	L_m	L_s	θ_e
Set No.7	D_m	L	A	(4.45)	(4.25)	(4.26)	L_m	(4.46)	θ_e
Set No.8	D_m	(4.49)	A	D_s	(4.25)	(4.26)	(4.48)	L_s	θ_e

4.5.2 Calculation of Radiation Pattern by Using PO/PTD techniques

In this thesis, the radiation patterns for the subreflector and the main reflector are calculated by employing PO and PTD techniques which are classified into four cases:

- (1) Using PO on both subreflector and main reflector (PO-PO)
- (2) Using PTD on subreflector and PO on main reflector (PTD-PO)
- (3) Using PO on subreflector and PTD on main reflector (PO-PTD)
- (4) Using PTD on both subreflector and main reflector (PTD-PTD)

In the analysis of dual reflector antennas, electromagnetic energy emitted from the feed reflects on the subreflector and it advances toward the main

reflector where it reflects again toward the out field. The numerical calculation of the radiation pattern consists of four main parts:

(1) To define the inputs of geometrical and electrical parameters such as frequency of operation, main reflector and subreflector geometry (diameter, position and its equation), and feed characteristics (feed type and position).

(2) To calculate the equivalent currents (PO currents) on the subreflector surface and the fringe currents on the edge of subreflector from the given feed pattern.

(3) To calculate the equivalent currents (PO currents) on the main reflector surface and the fringe currents on the edge of main reflector.

(4) To calculate the scattered fields due to PO currents and fringe fields due to fringe currents.

The PO and PTD procedure for analysis radiation pattern of reflector antenna by using PO and PTD are detailed in chapter 3. The outline procedure of each case is graphically in Figure 4.20.

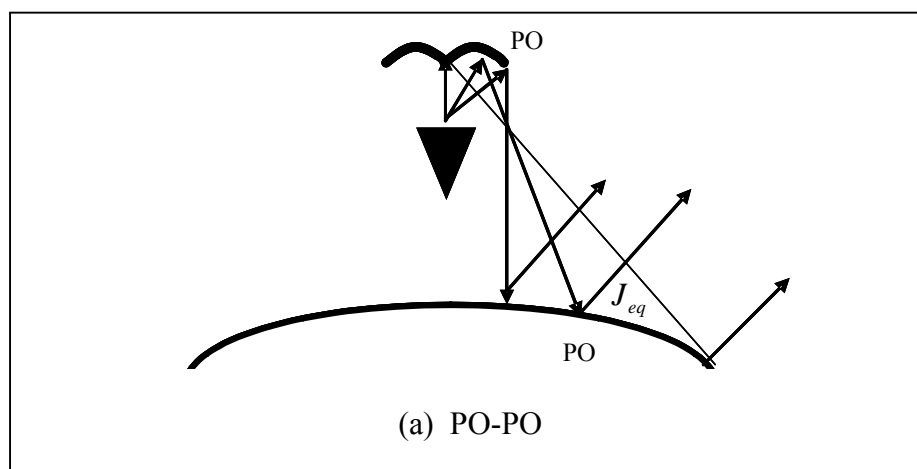


Figure 4.20 PO/PTD techniques for ADE backscatter antenna.

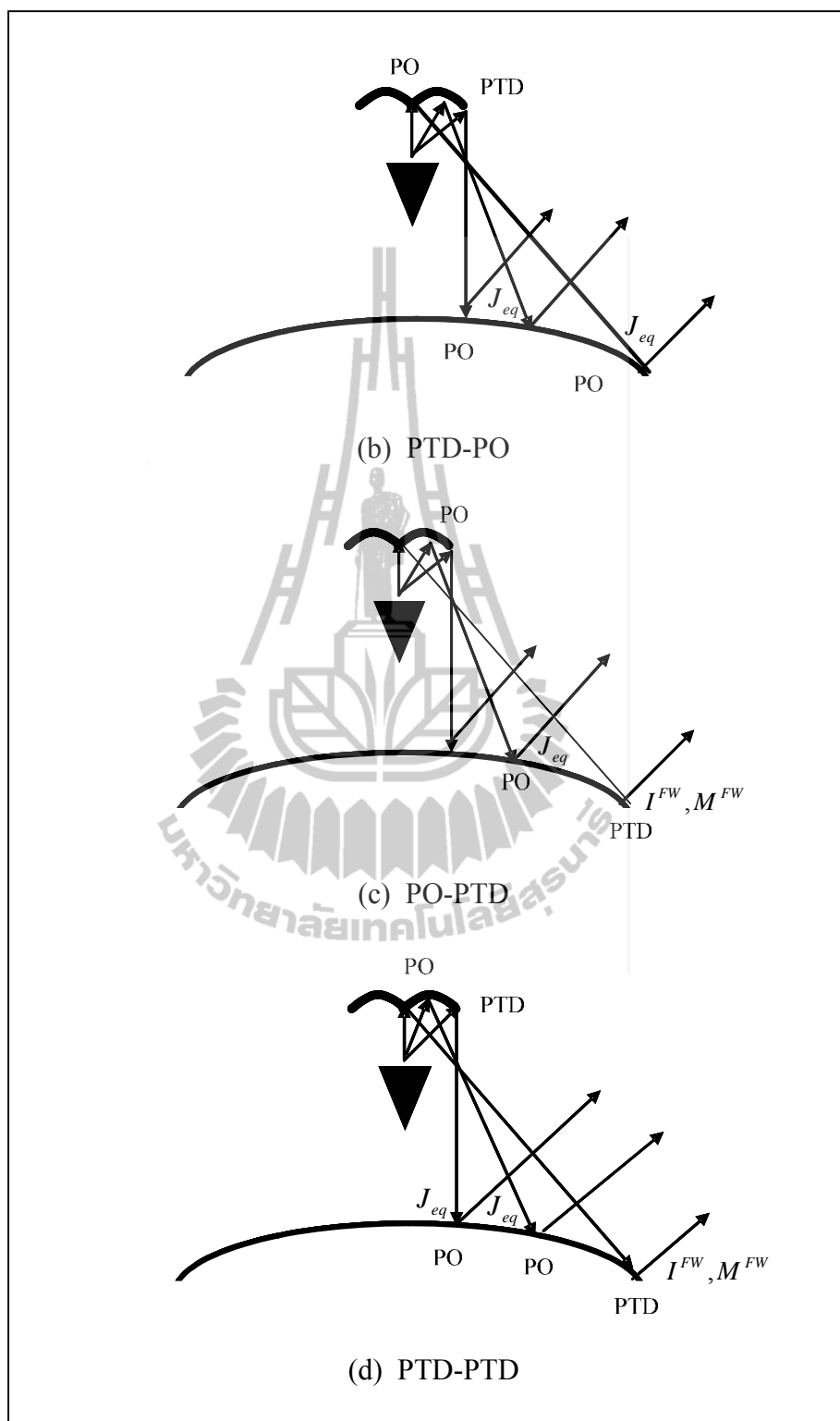


Figure 4.20 PO/PTD techniques for ADE backscatter antenna (Continued).

4.5.3 Analysis of Axially Displaced Ellipse Backscatter Antenna

In the first of analysis characteristics of ADE backscatter antenna, the radiation pattern of the proposed antenna has been simulated by using physical optics (PO) on subreflector and using physical theory of diffraction (PTD) on main reflector in order to enhance the accuracy of PO by better treatment of edge diffraction effect. The numerical calculation of the radiation pattern by using PO-PTD techniques consists of four main parts:

(1) To define the inputs of geometrical and electrical parameters such as frequency of operation, main reflector and subreflector geometry (diameter, position and its equation), and feed characteristics (feed type and position). The main reflector curve is Gaussian equation and subreflector is portion of an ellipse as expressed in (4.21) and (4.22), respectively. To design the axially displaced ellipse backscatter antenna as described in section 4.5.1, we need to choose five input parameters. The first example, set no.1 of input parameters i.e. diameter of the main reflector (D_m), diameter of the elliptical subreflector (D_s), parameter to define the convexity of the main Gaussian backscatter (A), parameter to define distance between main reflector and subreflector (L), and the angle θ_e are defined. The antenna has been carried out at 18.75 GHz. The conical horn as described in section 4.2 has been used to be a feed of the antenna. For choosing the input parameter, we start with the design of conical horn antenna that diameter has been accepted at 18.75 GHz (5.04 cm). Later, we choose the subreflector and main reflector diameters and the subreflector subtends angle (θ_e), values of the D_s / D_m ratio and θ_e have to provide the main reflector edge illumination around -10 dB to -15 dB. Then, we define the parameter A and L , to start with A between 7-9 cm and L between

20-40 cm. Finally, we iterate those parameters until the desired patterns are obtained. It was found that increasing of convexity of the main reflector can enhance coverage area but its gain is reduced. In addition, decreasing of the distance between main reflector and subreflector can enhance gain of the antenna. The antenna was designed using input parameters, i.e. $D_m = 30$ cm, $D_s = 5.6$ cm, $A = 8.2$ cm, $L = 30$ cm, and $\theta_e = 25^\circ$. From five input parameters, we can find the remaining design parameters in terms of these input parameters as expressed in Table 1. The geometry of proposed antenna is illustrated in Figure 4.21.

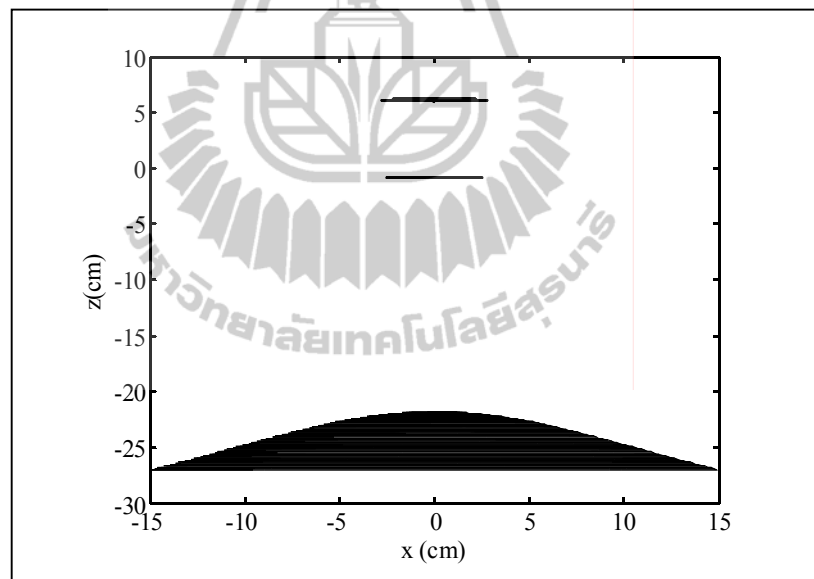


Figure 4.21 The ADE backscatter antenna geometry with set no.1 of input parameter: $D_m = 30$ cm, $D_s = 5.6$ cm, $A=8.2$ cm, $L=30$ cm, $a = 6.7370$ cm, $f = 1.4622$ cm, $L_s = 7.7293$ cm, $L_m = 37.3560$ cm and $\theta_e = 25^\circ$.

(2) To calculate the equivalent currents or PO currents on the subreflector surface. The subreflector surface and sampling points on its aperture are illustrated in Figure 4.22. The PO current on subreflector surface can be obtained directly from the incident field tangential to the subreflector at each point on its surface. The current distribution over the subreflector surface at each radial samples (ρ_{sr}^a) for diameter $D_s = 5.6$ cm and radius $\rho_{sr} = 2.8$ cm is shown in Figure 4.23.

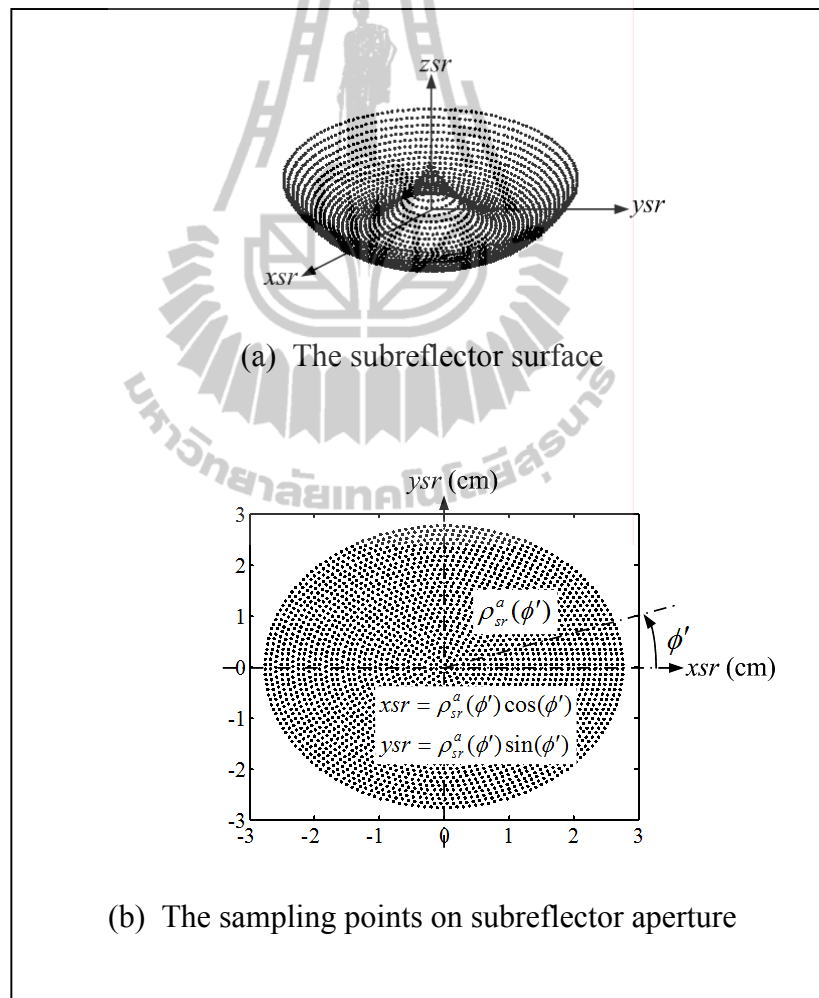


Figure 4.22 The subreflector surface and sampling points on its aperture.

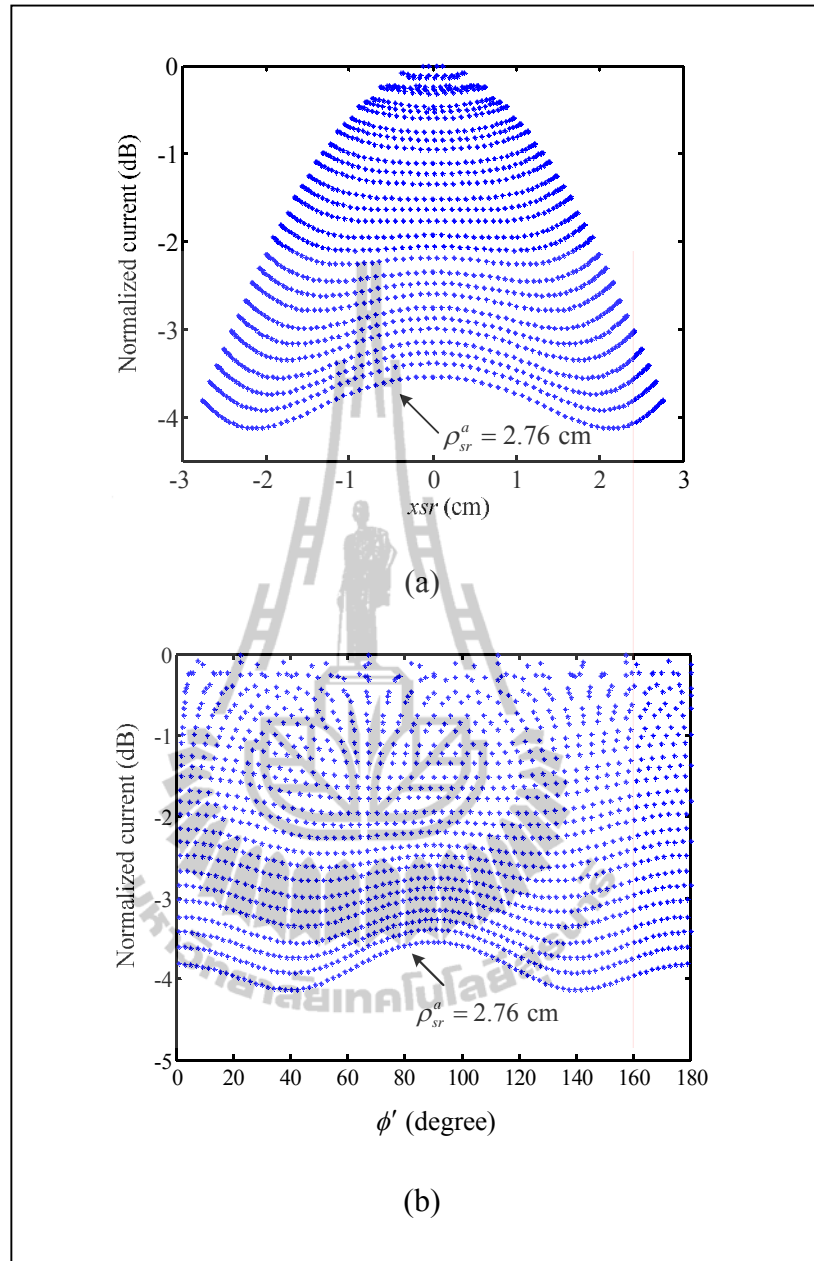


Figure 4.23 The current distributions over the subreflector surface at each radial samples for (a) plotting on x_{sr} coordination and (b) plotting on angle ϕ' in (degrees).

(3) To calculate the equivalent currents (PO currents) on the main reflector surface and the fringe currents on the edge of main reflector. The main reflector surface and sampling points on its aperture are illustrated in Figure 4.24. The current distribution over the main reflector surface at each radial samples (ρ_{mr}^a) for diameter $D_m = 30$ cm and radius $\rho_{mr} = 15$ cm and the fringe current on main reflector edge are shown in Figure 4.25 and Figure 4.26, respectively.

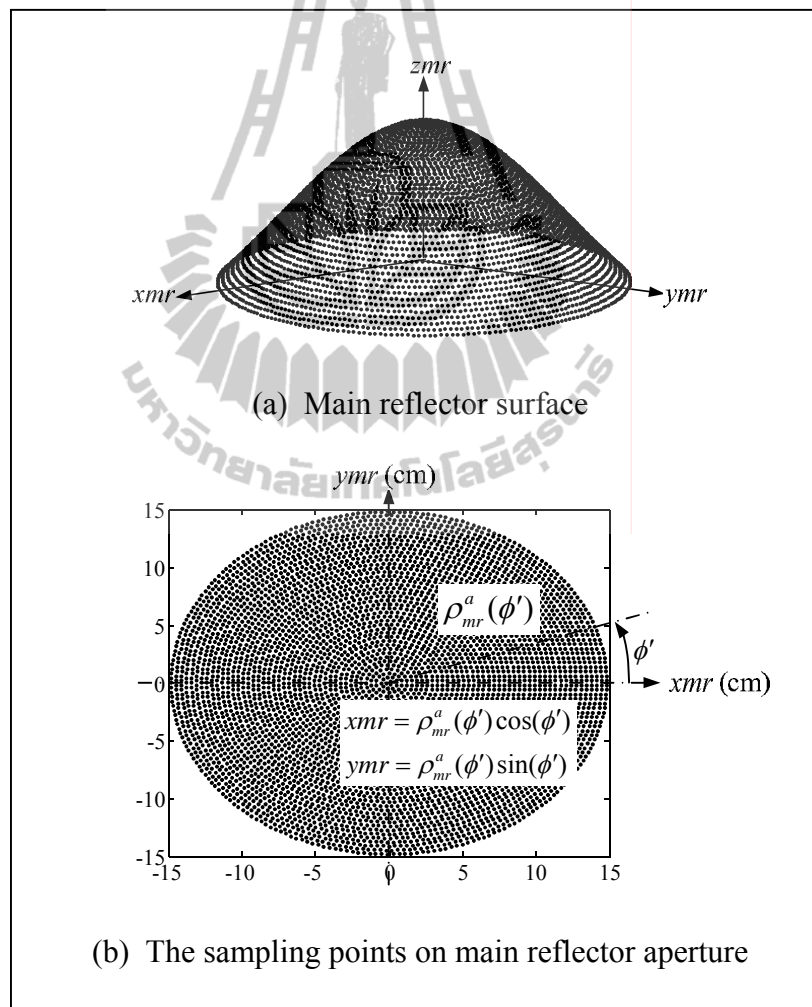


Figure 4.24 The main reflector surface and sampling points on its aperture.

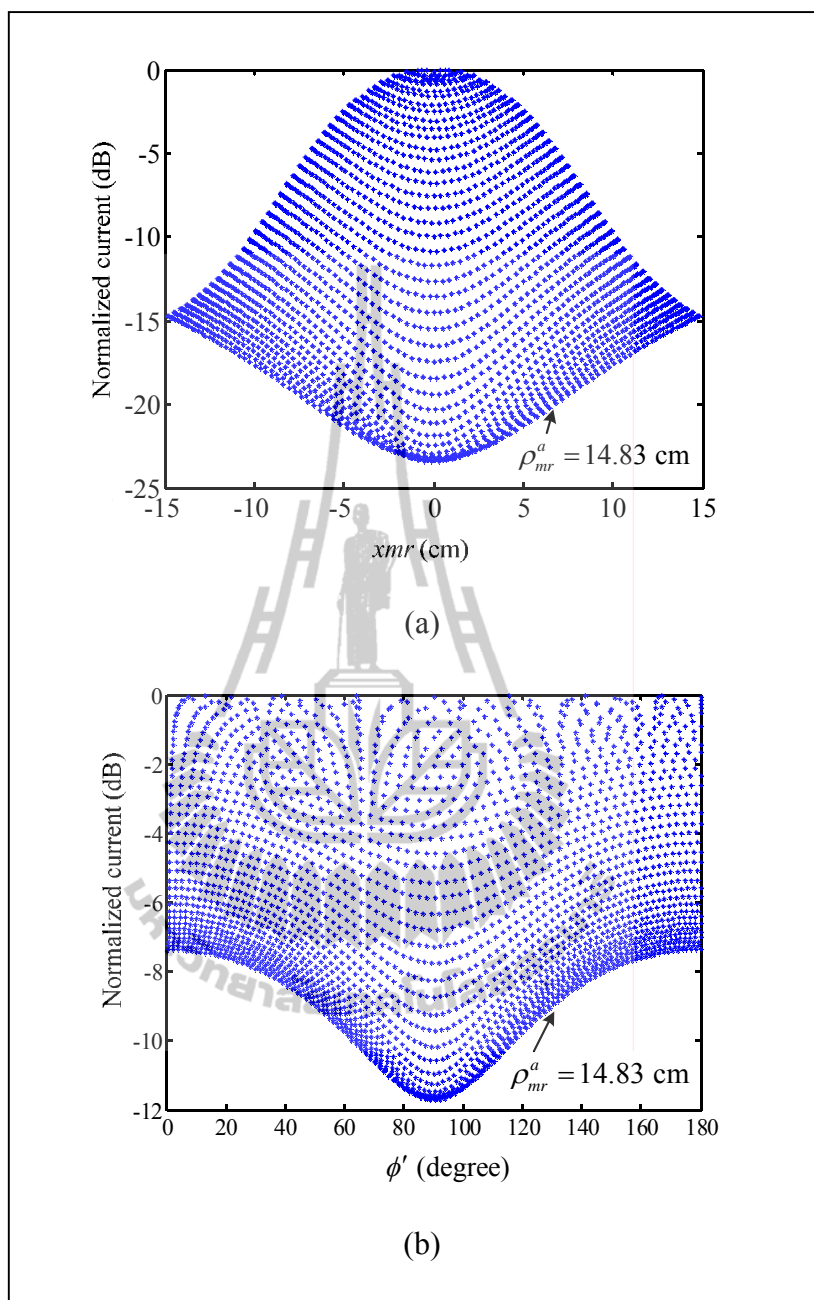


Figure 4.25 The current distributions over the main reflector surface at each radial samples for (a) plotting on x_{mr} coordination and (b) plotting on angle ϕ' in (degrees).

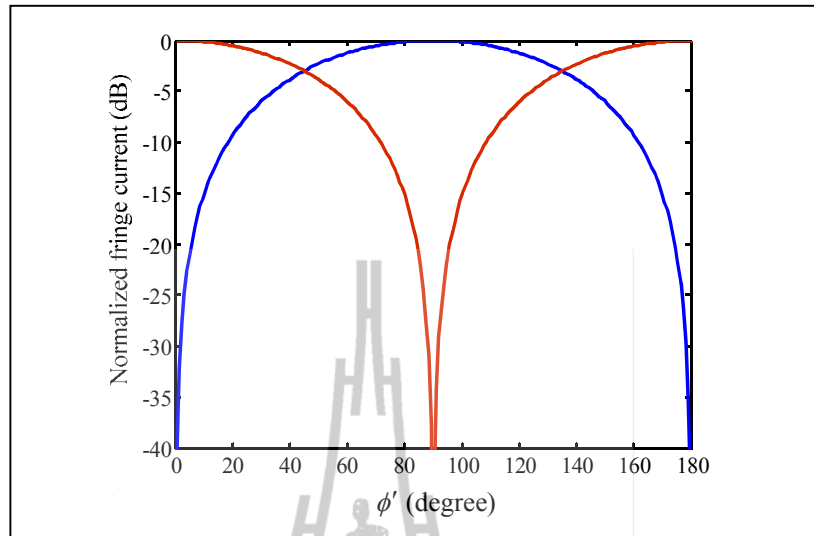


Figure 4.26 The fringe current along the edge of main reflector (red line: electrical equivalent fringe current, blue line: magnetic equivalent fringe current).

(4) To calculate the PO scattered fields due to PO currents and fringe fields due to fringe currents. The total scattered field is constructed by adding fringe field to the PO scattered field. The far-field patterns of proposed antenna in the $\phi = 0^\circ$ plane and $\phi = 90^\circ$ plane are shown in Figure 4.27. The antenna can provide gain about 12.75 dB in the $\phi = 0^\circ$ plane and 12.98 dB in the $\phi = 90^\circ$ plane. The coverage angle at gain 4 dB is around $\pm 72^\circ$ in the $\phi = 0^\circ$ plane and is around $\pm 68^\circ$ in the $\phi = 90^\circ$ plane.

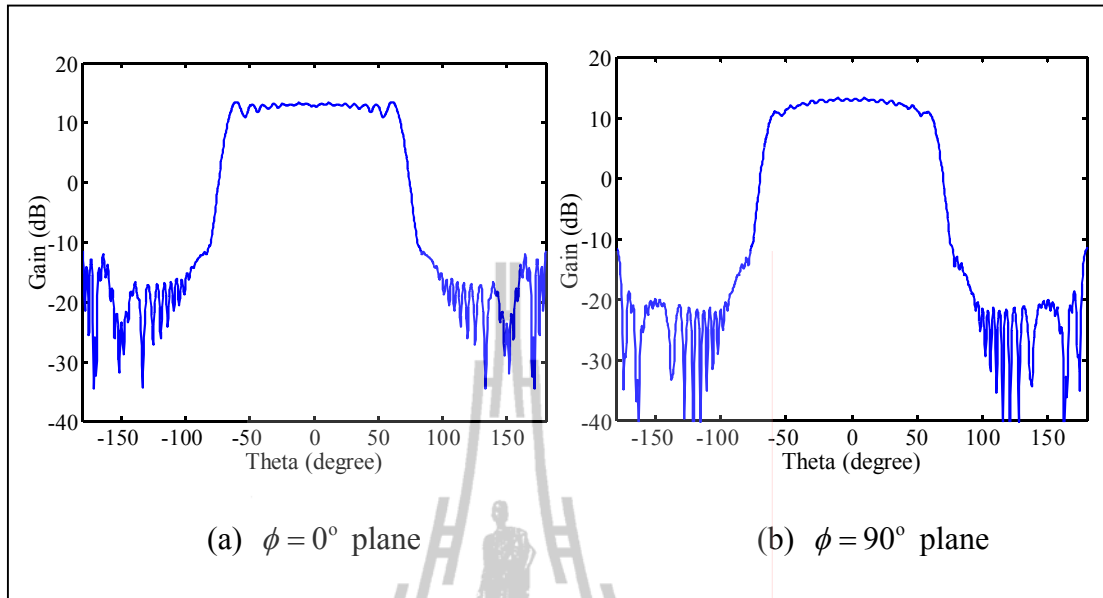


Figure 4.27 Radiation pattern of ADE backscatter antenna by using PO-PTD.

The simulation results as shown above, we have used PO on subreflector and PTD on main reflector. Taking into account the radiation pattern for ADE backscatter antenna by using hybrid method, we have classified the method for analysis ADE backscatter antenna into four cases as described in section 4.5.2 i.e., using PO on both subreflector and main reflector (PO-PO), using PTD on subreflector and PO on main reflector (PTD-PO), using PO on subreflector and PTD on main reflector (PO-PTD) and using PTD on both subreflector and main reflector (PTD-PTD). The results for radiation pattern computed by using PO-PO and PTD-PTD are plotted in Figure 4.28. It is seen that the effect of the PTD fringe field is importance in the far angular regions. The far-field patterns predicted by PO-PO underestimates the fields, and patterns predicted by using PTD-PTD accurately predict the fields. It is observed that in both the $\phi = 0^\circ$ plane and $\phi = 90^\circ$ plane, the far-field envelope predicted by PTD-PTD is higher than that by using PO-PO. The cross-polarized field

in the $\phi = 0^\circ$ plane and $\phi = 90^\circ$ plane compared between PO-PO and PTD-PTD are plotted in Figure 4.29. It is observed that PO-PO method predicts a very different cross-polarized pattern than that of PTD-PTD.

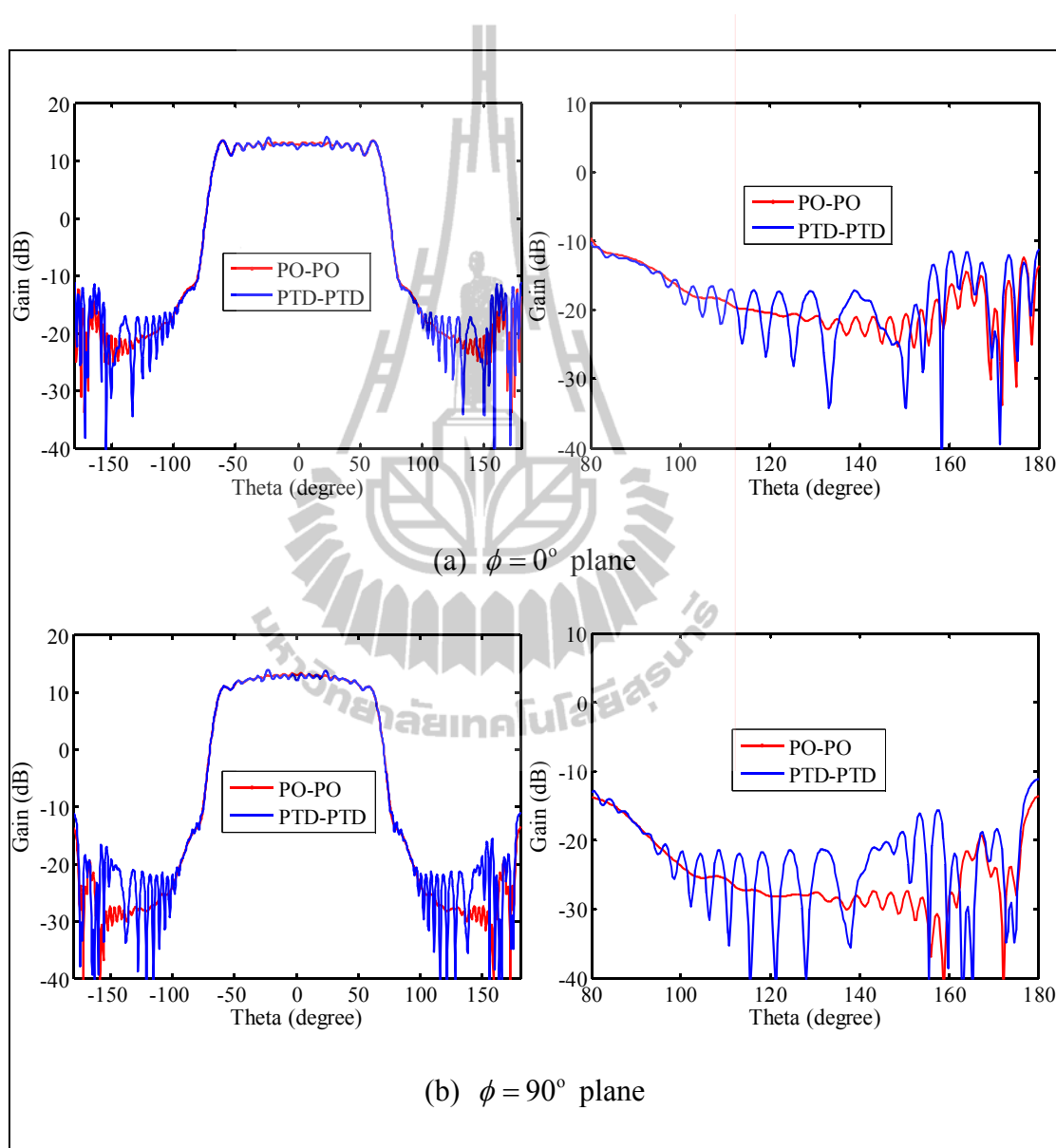


Figure 4.28 Radiation pattern of ADE backscatter antenna: comparison between PO-PO and PTD-PTD.

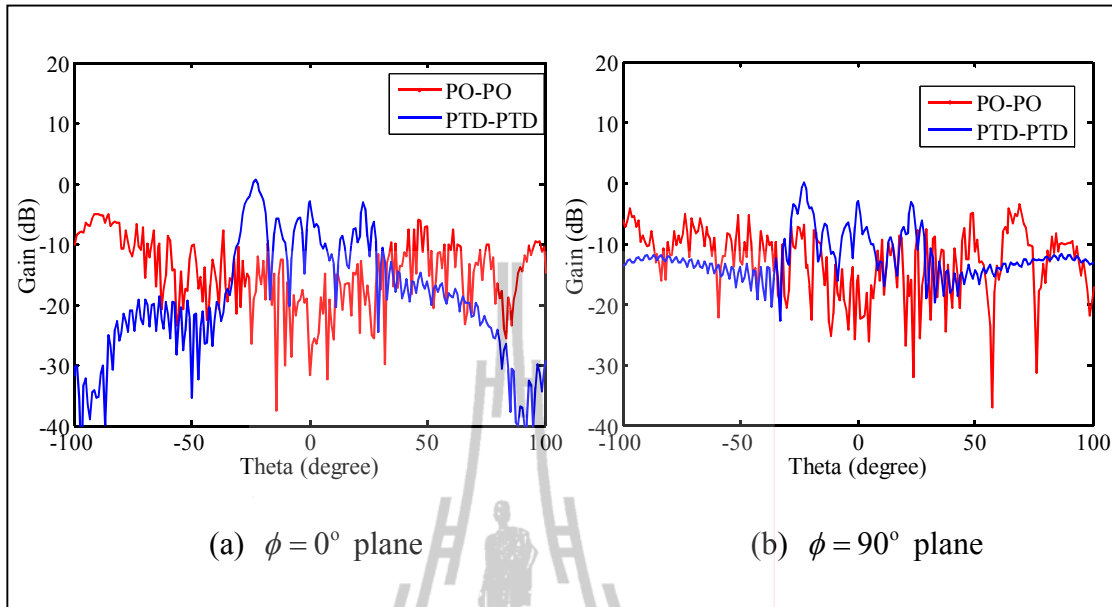


Figure 4.29 Cross-polarized fields of ADE backscatter antenna: comparison between PO-PO and PTD-PTD.

In the second case, the far-field patterns analyzed by using PTD-PO and PTD-PTD are illustrated in Figure 4.30. It is observed that the PTD-PO envelope error is also pronounced in the far angular regions on both the $\phi = 0^\circ$ plane and $\phi = 90^\circ$ plane. When we compare the far-field patterns predicted by PO-PO and PTD-PO found that the patterns predicted by PTD-PO are close to the patterns predicted by PTD-PTD than patterns predicted by PO-PO. To see the cross-polarized field, far-field patterns in the $\phi = 0^\circ$ plane and $\phi = 90^\circ$ plane are calculated and the results are shown in Figure 4.31. It is observed that in the angular $\theta \geq 25^\circ$, the envelope of the PTD-PTD field higher than that of the PTD-PO field both the $\phi = 0^\circ$ plane and $\phi = 90^\circ$ plane patterns.

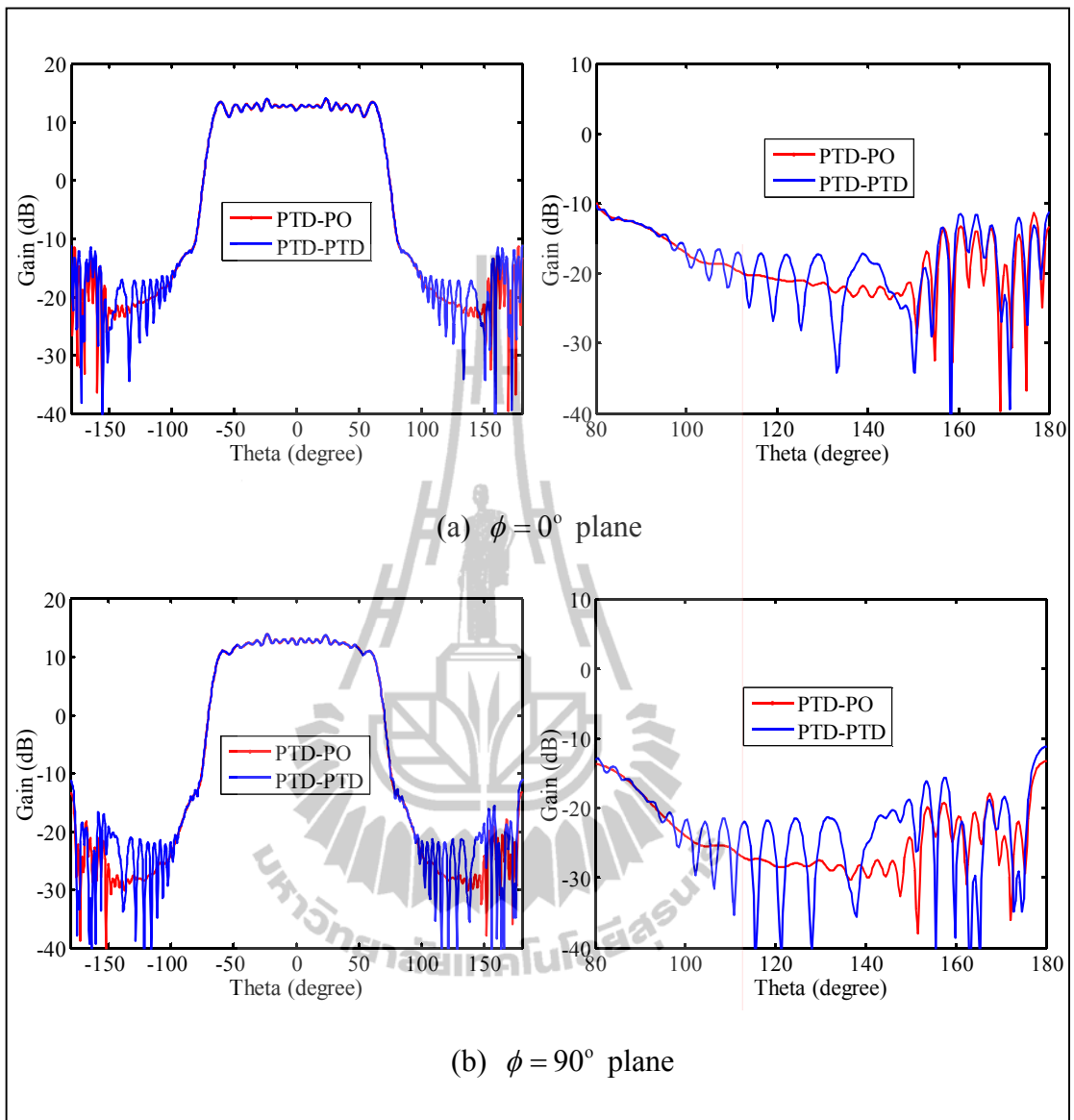


Figure 4.30 Radiation pattern of ADE backscatter antenna: comparison between PTD-PO and PTD-PTD.

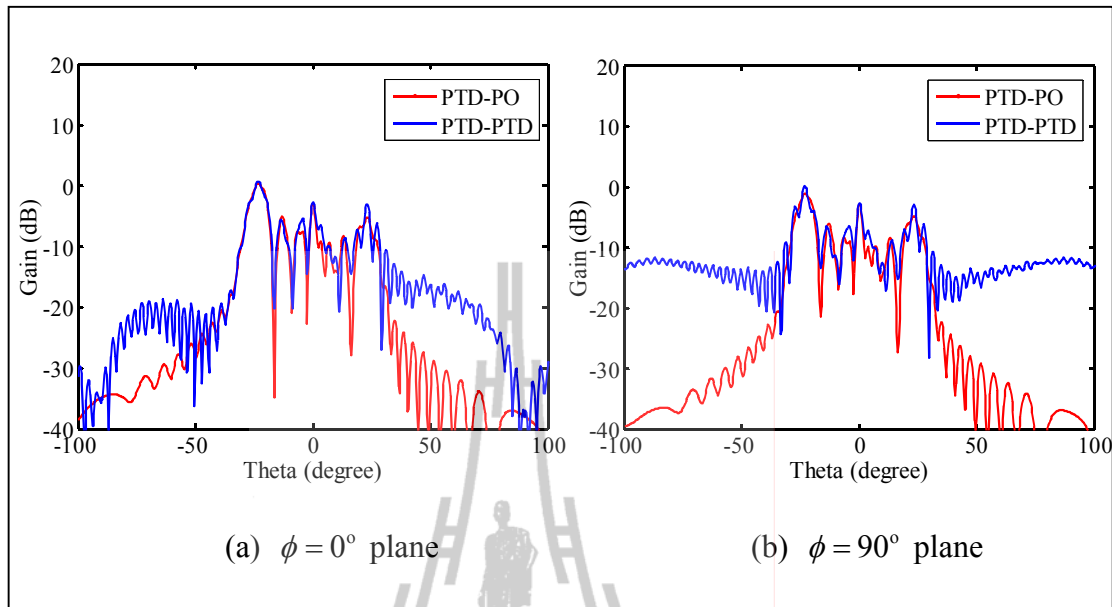


Figure 4.31 Cross-polarized fields of ADE backscatter antenna: comparison between PTD-PO and PTD-PTD

In the next case, the radiation comparison between PO-PTD and PTD-PTD are shown in Figure 4.32. It is observed that in the all angular region PO-PTD accurately predicts the field. The cross-polarized fields are plotted in Figure 4.33. It is found that in the angular range $-25^\circ \geq \theta \geq 25^\circ$, the envelope of the PTD-PTD field higher than that of the PO-PTD field both the $\phi = 0^\circ$ plane and $\phi = 90^\circ$ plane. From all simulation results, it can conclude that the PO-PTD solution is almost indistinguishable which that of the PTD-PTD. In the case of cross-polarization, PO-PO predicts a very different cross-polarized pattern than that of PTD-PO, PO-PTD and PTD-PTD. It is observed that in the near-in angular region, PTD-PO is small different with PTD-PTD, while in the far-angular region PO-PTD is close with PTD-PTD.

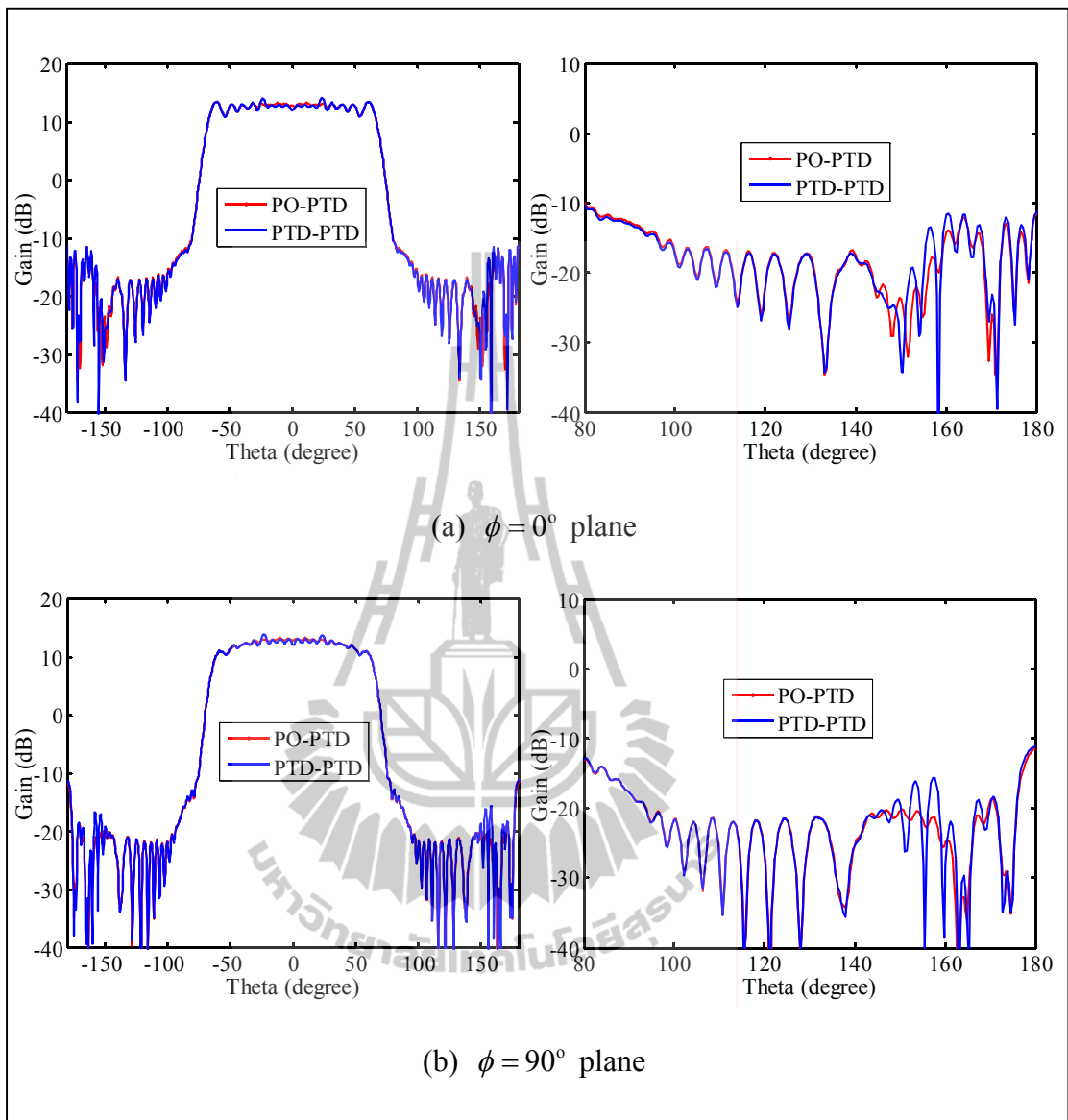


Figure 4.32 Radiation pattern of ADE backscatter antenna: comparison between PO-PTD and PTD-PTD.

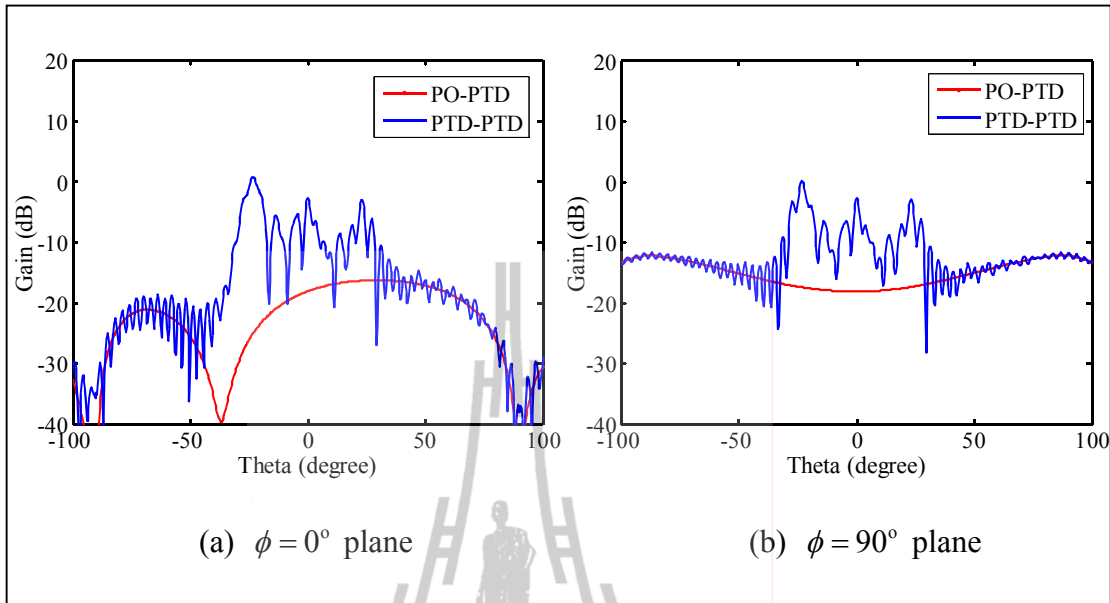


Figure 4.33 Cross-polarized fields of ADE backscatter antenna: comparison between PO-PTD and PTD-PTD.

4.5.4 Example of Axially Displaced Ellipse Backscatter Antenna when Input Parameters are Changed

In the section 4.5.3, we analyzed radiation pattern of ADE backscatter antenna by employing PO and PTD techniques. The ADE backscatter antenna was designed by using set no.1 of input parameters. In this section, we will give design example of ADE backscatter antenna when input parameters have been changed. The procedure for designing the ADE backscatter antenna with different sets of input parameters as describe in section 4.5.1 depend on the requirements of the antenna size and performance. The aim of this thesis is the proposed antenna must have the gain more than 10 dB and must have the coverage angle at gain 4 dB more than $\pm 65^\circ$.

In the first example, the proposed antenna will be designed by using set no.2 of input parameters i.e. diameter of the main reflector (D_m), parameter to define the convexity of the main reflector (A), parameter to define distance between feed and main reflector (L_m), parameter to define distance between feed and subreflector (L_s), and the angle θ_e . For choosing the input parameter, we start with choosing the main reflector diameter, parameter to define the convexity of the main reflector A and the angle θ_e . Then, we define the parameter L_s and the parameter L_m , to start with L_s between 5-10 cm and L_m between 25-30. Finally, we iterate those parameters until the desired patterns are obtained. The antenna was designed by using the input parameters, i.e. $L_m = 28$ cm, $D_m = 30$ cm, $A = 8.2$ cm, $L_s = 8$ cm, and $\theta_e = 20^\circ$. From five input parameters, we can find the remaining design parameters in terms of these input parameters as expressed in Table 1. These values present small antenna (compact size) with acceptable dimensions intended to provide optimum gain and wide beamwidth. The designed antenna is presented in Figure 4.34. The antenna is analyzed by using PO on subreflector and PTD on main reflector (PO-PTD). The radiation pattern of the antenna is shown in Figure 4.35. The gain in the $\phi = 0^\circ$ plane and $\phi = 90^\circ$ plane are 13.08 dB and 13.15 dB, respectively. The coverage angle at gain 4 dB is around $\pm 71^\circ$ in the $\phi = 0^\circ$ plane and is around $\pm 66^\circ$ in the $\phi = 90^\circ$ plane.

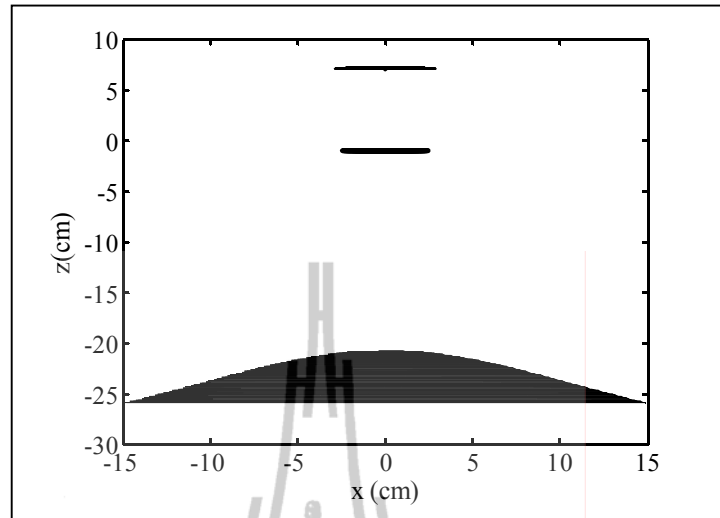


Figure 4.34 The ADE backscatter antenna geometry with set no.2 of input

parameter: $D_m = 30$ cm, $A = 8.2$ cm, $L_s = 8$ cm, $L_m = 28$ cm,

$D_s = 5.8487$ cm, $L = 28.9815$, $f = 1.5423$ cm,

$a = 7.8017$ cm and $\theta_e = 20^\circ$.

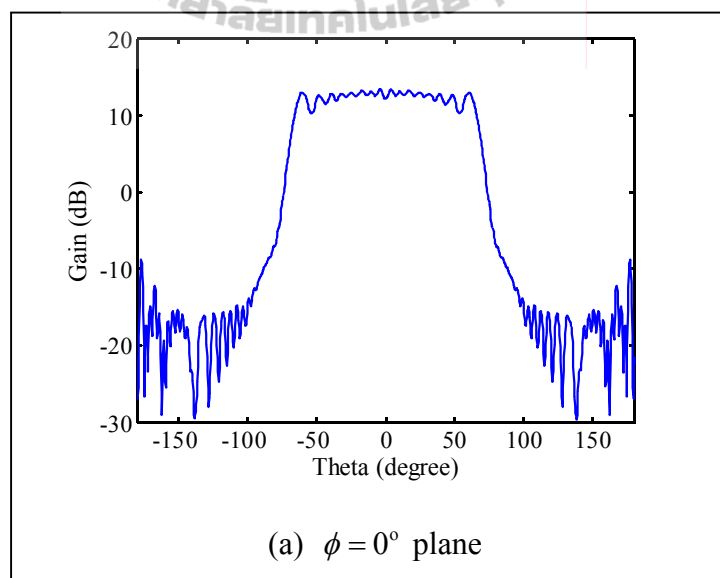


Figure 4.35 Radiation pattern of ADE backscatter antenna when using set no.2 of input parameters.

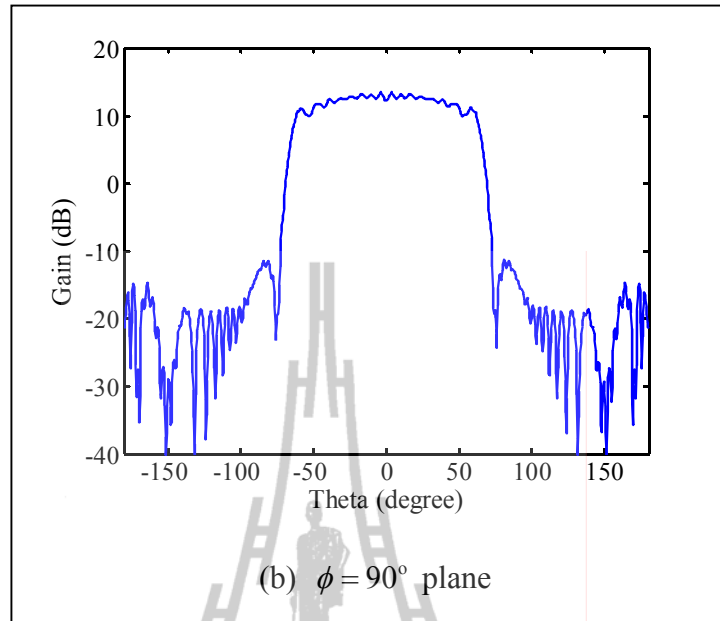


Figure 4.35 Radiation pattern of ADE backscatter antenna when using set no.2 of input parameters (Continued).

In the second example, the antenna is designed by using set no.5 of input parameters i.e. diameter of the subreflector (D_s), parameter to define the convexity of the main reflector (A), parameter to define distance between main reflector and subreflector (L), parameter to define distance between feed and subreflector (L_s) and the angle θ_e . For the optimum designed, the input parameters are chosen i.e. $D_s = 5.6$ cm, $L_s = 7.6$ cm, $L = 32$ cm, $A = 8.2$ cm, and $\theta_e = 20^\circ$. The antenna geometry is shown in Figure 4.36. The radiation pattern by using PO-PTD method is illustrated in Figure 4.37. The gain in the $\phi = 0^\circ$ plane and $\phi = 90^\circ$ plane are 15.24 dB and 15.70 dB, respectively. The coverage angle at gain 4 dB is around $\pm 66^\circ$ in the $\phi = 0^\circ$ plane and is around $\pm 61^\circ$ in the $\phi = 90^\circ$ plane. Although the coverage angle is reduced, however, this geometry can improve antenna gain.

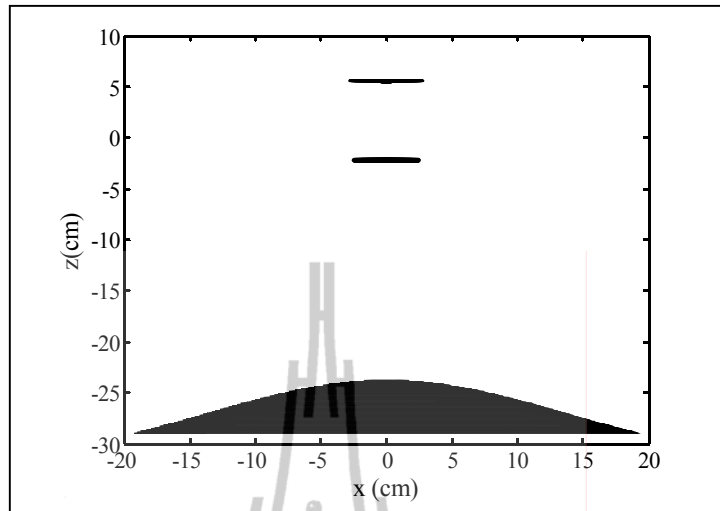


Figure 4.36 The ADE backscatter antenna geometry with set no.5 of input

parameter: $D_s = 5.6$ cm, $L_s = 7.6$ cm, $L = 32$ cm, $A = 8.2$ cm,

$L_m = 29.8284$ cm, $D_m = 38.6116$ cm, $f = 1.7717$ cm,

$a = 6.8540$ cm and $\theta_e = 20^\circ$.

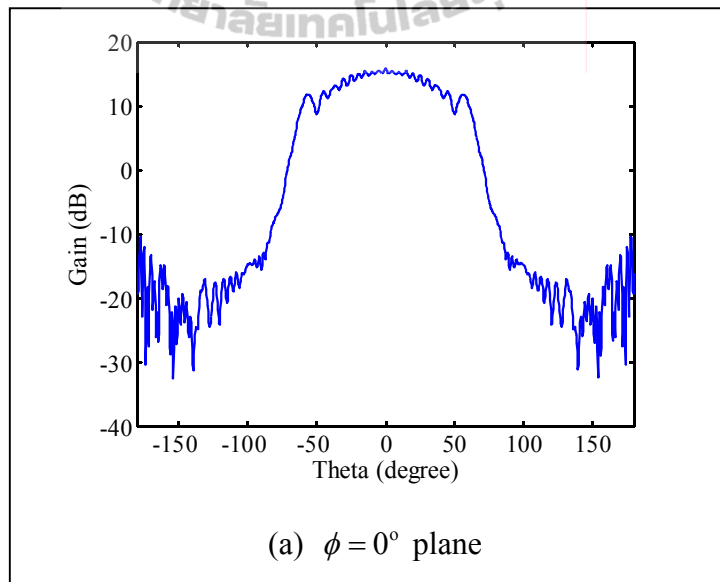


Figure 4.37 Radiation pattern of ADE backscatter antenna when using set no.5 of input parameters.

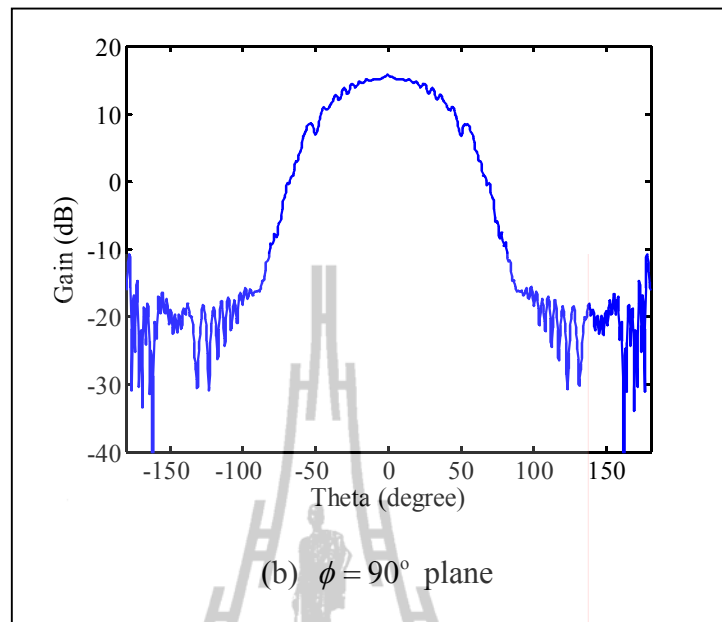


Figure 4.37 Radiation pattern of ADE backscatter antenna when using set no.5 of input parameters (Continued).

The examples of ADE backscatter antenna as describe above was designed by using different sets of input parameters. From the examples, it can be summarized that these set of input parameters can be chosen according to the characteristic requirements in practical applications such as size and its performance.

4.5.5 Example of Axially Displaced Ellipse Backscatter Antenna when Equation of Main Reflector is Changed

In this section, we will give design example when the main reflector equation has been changed. A quadratic equation is chosen to be main reflector as expressed in (4.49),

$$z_{mr}(x_{mr}) = A \left(1 - \left(\frac{2}{D_m} x_{mr} \right)^2 \right) - L. \quad (4.49)$$

The antenna is designed by using set no. 1 of input parameters (see Table 1). For the optimum designed, the input parameters are chosen i.e. $D_m = 30$ cm, $D_s = 5.6$ cm, $L = 30$ cm, $A = 5.8$ cm, and $\theta_e = 25^\circ$, where same input parameters with the case of Gaussian equation. The antenna geometry is presented in Figure 4.38. The radiation pattern of the antenna is analyzed by using PO-PTD method as shown in Figure 4.39. The gain in the $\phi = 0^\circ$ plane and $\phi = 90^\circ$ plane are 11.7 dB and 12.25 dB, respectively. The coverage angle at gain 4 dB is around $\pm 70^\circ$ in the $\phi = 0^\circ$ plane and is around $\pm 60^\circ$ in the $\phi = 90^\circ$ plane. It was found that when the main reflector shape has been changed, the antenna characteristics have also changed. When we compare the main reflector equations between Gaussian and quadratic with the same input parameter found that Gaussian equation can provide higher gain and wider coverage area than quadratic equation. In this thesis, we have decided to choose the Gaussian equation to construct antenna model because it has appropriate characteristics.

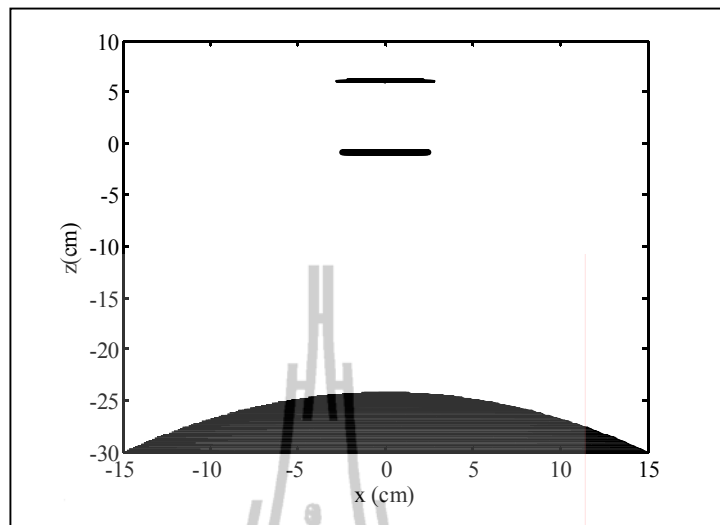


Figure 4.38 The ADE quadratic backscatter antenna geometry with set no.1 of input parameters: $D_m = 30$ cm, $D_s = 5.6$ cm, $A = 5.8$ cm, $L = 30$ cm, $f = 1.4622$ cm, $L_s = 7.7293$ cm, $L_m = 34.9560$ cm and $\theta_e = 25^\circ$.

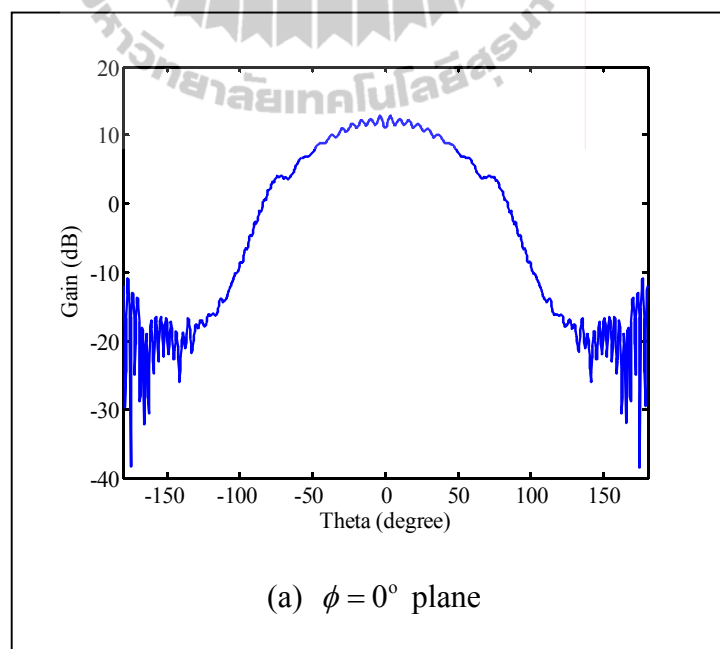


Figure 4.39 Radiation pattern of ADE quadratic backscatter antenna when using set no.1 of input parameters.

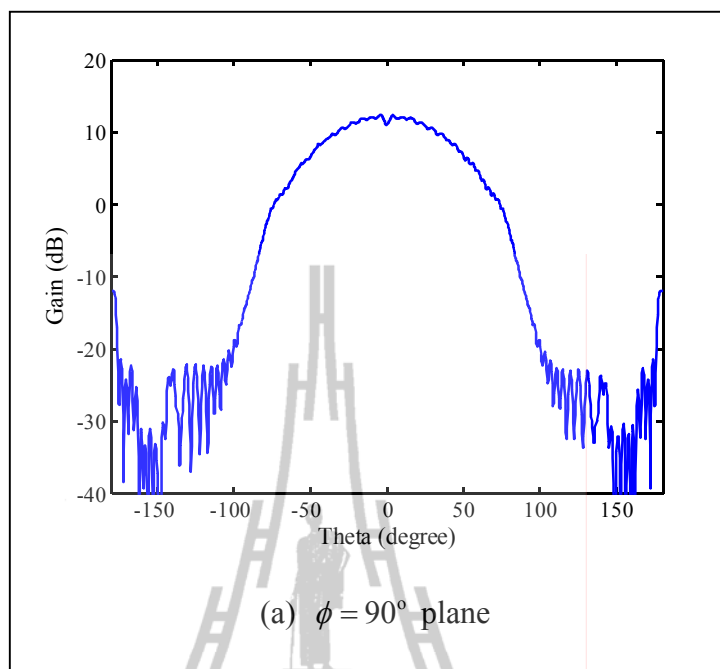
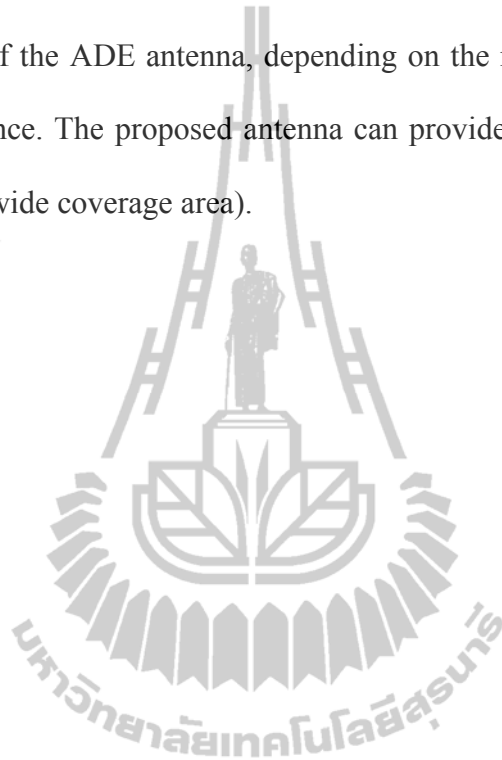


Figure 4.39 Radiation pattern of ADE quadratic backscatter antenna when using set no.1 of input parameters (Continued).

4.6 Chapter Summary

In this chapter presented analysis and design of axially displaced ellipse antenna (ADE antenna). The first, the design and numerical examples of ADE reflector antenna was compared with both computational and experimental data published in literature such as IEEE data base. The radiation patterns were compared with Granet (2001) and Kumar (2009). It was found that the results depict very good agreement. The results from these examples provide the confidence that the PO, which is developed by using Matlab program, is accurate for prediction the field. The second, the analysis and design of ADE backscatter antenna which is the proposed antenna in this research was presented. The radiation pattern of proposed antenna is analyzed by using PO and PTD method. We have classified the method for analysis of

radiation pattern of ADE backscatter antenna into four cases i.e. PO-PO, PTD-PO, PO-PTD, and PTD-PTD. It is found that the PO-PTD solution is most indistinguishable which that of the PTD-PTD. From design example of ADE backscatter antenna with several sets of input parameters, we can design and choose input parameters of the ADE antenna, depending on the requirements of the antenna size and performance. The proposed antenna can provide gain more than 10 dB and wide beamwidth (wide coverage area).



CHAPTER V

MEASUREMENT AND DISCUSSION

5.1 Introduction

In order to understand the general background and the theory behind the ADE antenna, the antenna measurements for the final verification of the ADE backscatter antenna operation will be presented in this chapter. The ADE backscatter antenna was fabricated and their performance was measured and discussed. To verify the theory calculation, the radiation patterns were measured in an anechoic chamber using vector network analyzer HP 8722D and compared with the simulated results by using PO/PTD method. The effects of the support structures on the radiation patterns of the proposed antenna have been investigated experimentally.

5.2 ADE Backscatter Antenna Prototype

The ADE backscatter antenna geometry consists of a main reflector by using backscattering technique, portion of an ellipse subreflector, and a conical horn antenna. In this thesis, we have chosen the Gaussian equation for main reflector because it has appropriate characteristics i.e. low ripple level and wide coverage angle. As describe in chapter 4, the ADE backscatter antenna was designed and analyzed at frequency of 18.75 GHz. The antenna was designed by using set no.1 of input parameters as summarized in Table 5.1. To verify the performance of the antenna, a prototype has been fabricated with aluminium at the operating frequency of

18.75 GHz as shown in Figure 5.1. The antenna was constructed by high-precision CNC machine.

Table 5.1 Dimensions of the ADE backscatter antenna.

Description	Dimension (λ)	Dimension (cm)
Diameter of the main reflector (D_m)	18.75	30
Distance between point O and the projection of the bottom-edge of the half-main-reflector onto the axis (L)	18.75	30
Diameter of the elliptical subreflector (D_s)	3.50	5.6
Parameter to define the convexity of the main reflector (A)	5.125	8.2
Half cone angle subtended by the subreflector at F_0 (θ_e)	25°	25°
Distance between the focus, F_0 , of the antenna and the projection of the top-edge of the half-main-reflector onto the Z axis (L_m)	23.346	37.3536
Distance between the focus, F_0 , of the antenna and the apex of the subreflector (L_s)	4.831	7.7293
Half distance between the foci of ellipse (f)	0.892	1.4622
Half major axis of the ellipse (a)	4.221	6.7370

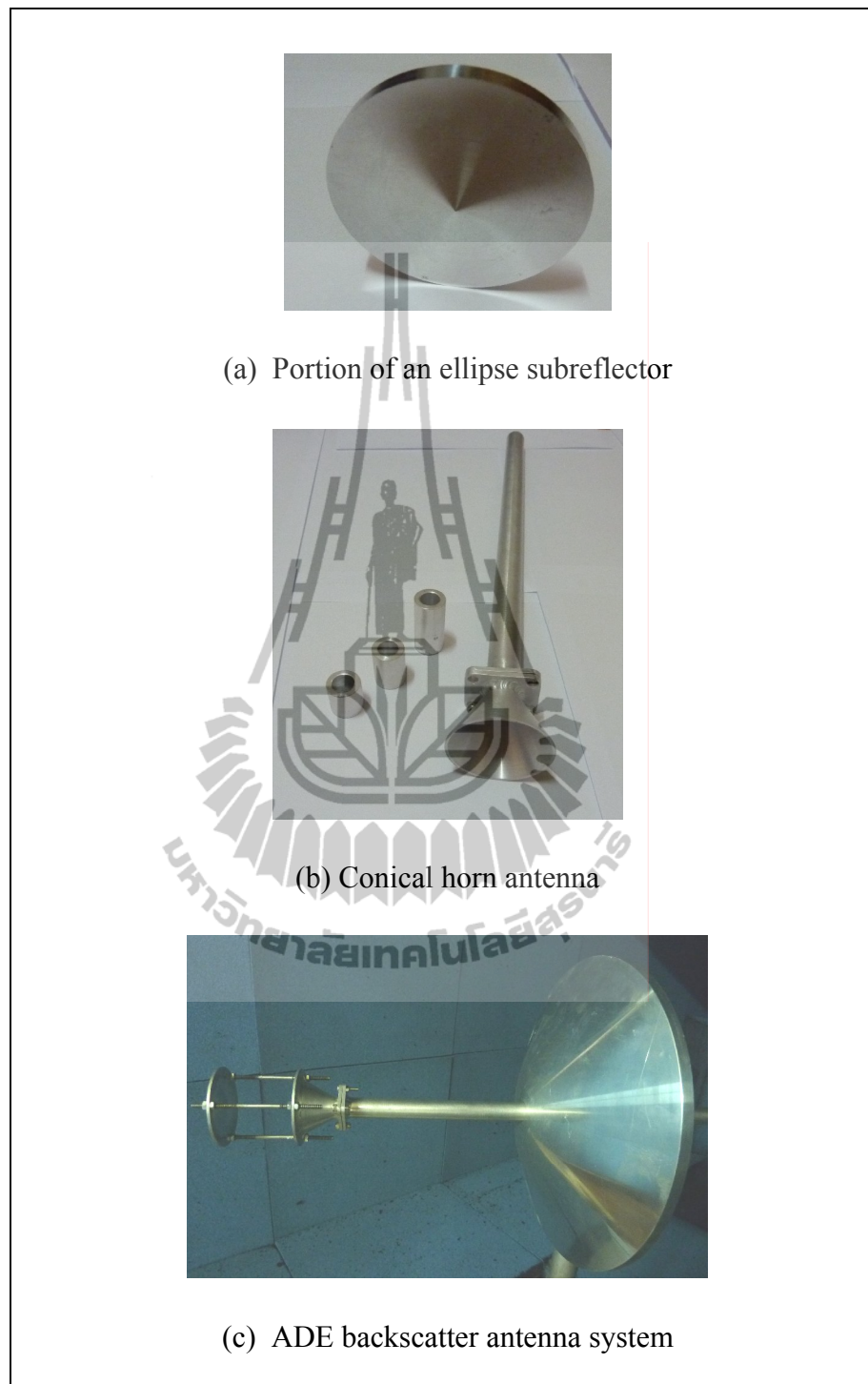


Figure 5.1 ADE backscatter antenna prototype.

5.3 Antenna Measurement

Antenna measurements are needed for the final verification of the antenna operation. Modern simulation and analysis methods predict often quite accurately the antenna characteristics, but for some complicated structures only measurements can give accurate information on the antenna properties. In the all cases, it is beneficial to verify the computed results with measurements to ensure that antenna was correctly modelled in the simulations and correctly assembled. In this section, antenna radiation characteristics and measured results are discussed.

Reciprocity theorem is applied to most antennas and, therefore, properties of antenna used to receive electromagnetic waves are the same as the properties for the same antenna when it is used to transmit electromagnetic waves. The space surrounding an antenna is commonly divided into three parts based on the behavior of the antenna radiation: a reactive near field region, a radiating near field region, and a far field region. The regions are illustrated in Figure 5.2.

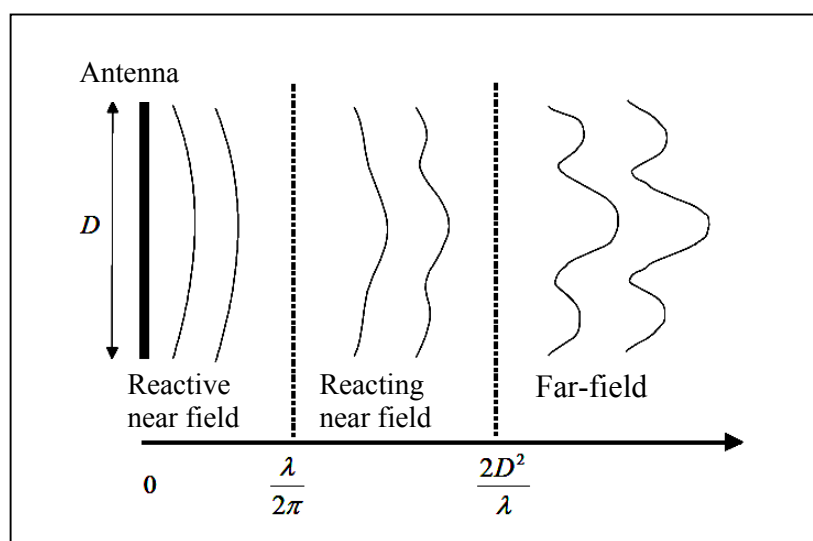


Figure 5.2 Near field and far field region of an antenna.

In the reactive near field, the reactive field dominates and power is not propagating. The borders between the regions are not exact or unique as there are various criteria to separate the regions. Outer boundary of the reactive near field is usually defined as

$$R = \frac{\lambda}{2\pi}. \quad (5.1)$$

The antenna is large compared to the wavelength λ . The radiating near field, or Fresnel region as it is also called for antenna focused at infinity, is a transition region between the reactive near field and the far field region. In this region, the radiation fields predominate, but the angular field distribution depends on the distance from the antenna. The radial field component may also significant in this region. The far field region is defined to begin at

$$R = \frac{2D^2}{\lambda}, \quad (5.2)$$

where D is maximum dimension of the antenna. At this distance the phase error due to the maximum path length difference between different points on antenna is $\pi/8$. In the far field, the field components are essentially transverse and the angular distribution of the field is independent of the distance.

5.3.1 Radiation Pattern

Radiation pattern (antenna pattern) is the spatial distribution of a quantity that characterizes the electromagnetic field generated by an antenna. The antenna radiation pattern is the display of the far field radiation properties of the

antenna in spherical coordinates at a constant radial distance and frequency. In general, this pattern is three-dimensional, however, because it is not practical to measure this, a number of two-dimensional patterns, or pattern cuts, are recorded by fixing one angle and varying the others (Balanis, 1997).

A far field pattern is obtained in the far field of the antenna as expressed in (5.2). In the far field antenna test, the ADE backscatter antenna was measured in anechoic chamber. The conical horn antenna is used to be transmitting antenna, while ADE backscatter antenna is in receiving mode. The ADE backscatter antenna is installed on a turntable with the Raleigh distance R far from transmitting antenna as shown in Figure 5.3. During the measurements, the ADE backscatter antenna was illuminated with a uniform plane wave and their receiving characteristics were measured.

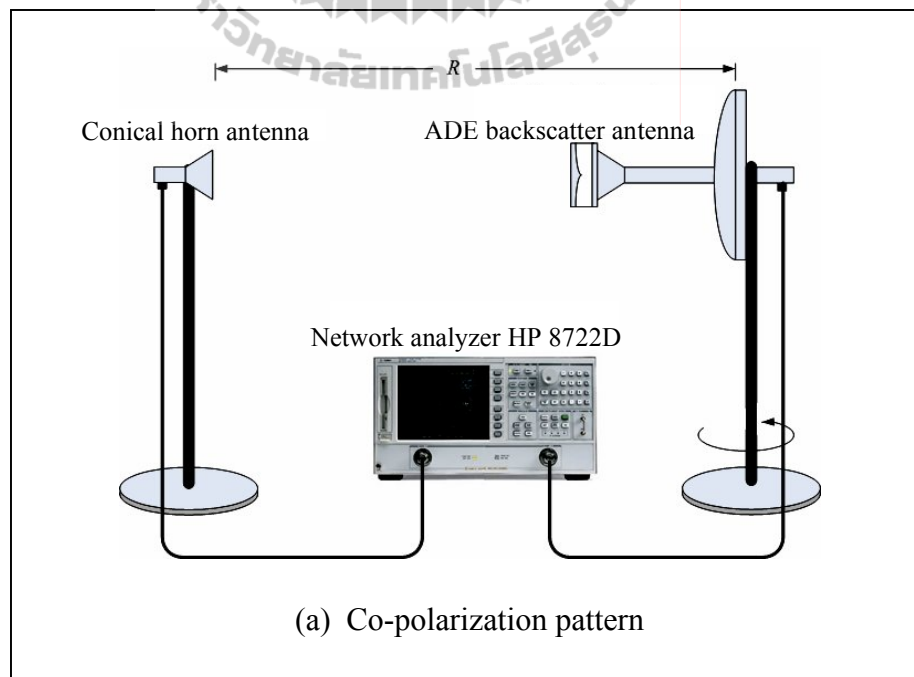


Figure 5.3 Measurement set up for the radiation pattern.

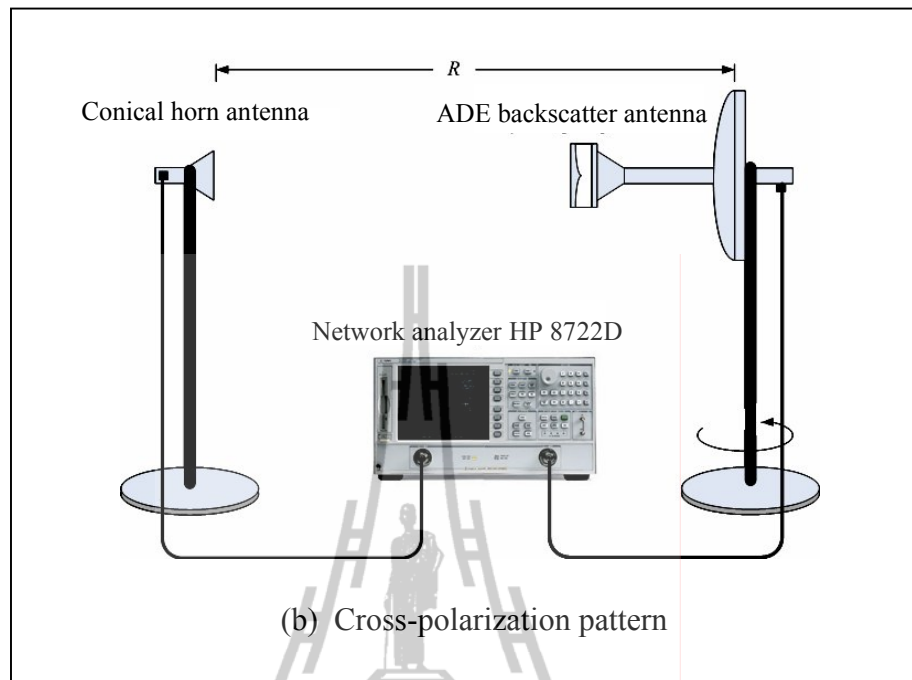


Figure 5.3 Measurement set up for the radiation pattern (Continued).

5.3.2 Gain

The gain of an antenna is the ratio of the radiation intensity, in a given direction, to the radiation intensity that would be obtained if the power accepted by the antenna is radiated isotropically. Absolute gain method is one of the basic methods to measure the gain of an antenna (Balanis, 1997). For this method, the theory is based on the Friis transmission formula as expressed in (5.3), which can be applied when two polarizations matched antennas aligned for the maximum directional radiation, and separated by a distance R that meets the far field criteria, are used for the measurements,

$$G_{r,dB} + G_{t,dB} = P_{r,dB} - P_{t,dB} + 20 \log \left(\frac{4\pi R}{\lambda} \right), \quad (5.3)$$

where P_r is the received power,

P_t is the transmitted power,

G_r is the gain of the receiving antenna,

G_t is the gain of the transmitting antenna.

The absolute gain method requires no a knowledge of the transmitting or receiving antenna gain. If the receiving and transmitting antennas are identical, only one measurement is required and (5.3) can be simplified as

$$G_{r,dB} = G_{t,dB} = \frac{1}{2} \left[P_{r,dB} - P_{t,dB} + 20 \log \left(\frac{4\pi R}{\lambda} \right) \right]. \quad (5.4)$$

5.3.3 Bandwidth

The bandwidth of an antenna is defined as the range of frequencies within which the performance of the antenna, with respect to some characteristics, conforms to a specified standard. The bandwidth can be considered to be the range of frequencies, on either side of a center frequency, where the antenna characteristics such as input impedance, pattern, beamwidth, polarization, side lobe level, gain, beam direction or radiation efficiency, are within an acceptable value of those at the center frequency (Balanis, 2005).

For narrowband antennas, the bandwidth is expressed as a percentage of the frequency difference (upper minus lower) over the center frequency of the bandwidth. Equation (5.5) is the fundamental formula to calculate the bandwidth of the antenna from the return loss versus the frequency plot.

$$\text{Bandwidth (\%)} = \left[\frac{(f_{upper} - f_{lower})}{f_0} \right] \times 100\% \quad (5.5)$$

5.3.4 Input Impedance, Standing Wave Ratio and Return Loss

The input impedance, standing wave ratio (SWR) and return loss (S_{11}) are parameters which can be used to indicate the degree of mismatch between transmission line and its load (usually a radio antenna), or evaluate the effectiveness of impedance matching efforts. The impedance is in the range of 40-60 Ω and SWR less than 2 can be accepted for impedance matching between transmission line and the antenna which correspond to the return loss less than -10 dB.

5.4 Experimental Results

5.4.1 Conical Horn Antenna

In this thesis, the conical horn antenna operating at the frequency of 18.75 GHz is used to be feed of ADE backscatter antenna. The measured results of return loss (S_{11}), input impedance and standing wave ratio (SWR) are shown in Figure 5.4 to 5.6, respectively. It is found that the measured return loss at frequency of 18.75 GHz is -29.059 dB. Impedance matching which is referred to $S_{11} \leq -10$ dB is achieved. The measured of input impedance of conical horn antenna is 49.994 Ω . The impedance is accepted because it is in the range of 40 to 60 Ω . The standing wave ratio is 1.0711 ($\text{SWR} \leq 2$). The measured impedance bandwidth is about 6.94% ($S_{11} < -10$ dB). As shown in Figure 5.7, the measured far field patterns in E- and H-planes of conical horn antenna are plotted together with the simulated results which are calculated by using aperture field integration method (AFIM). From the measured

results, the conical horn antenna can provide the gain and HPBW in E-plane of 11.05 dB and 28°, respectively, and in H-plane of 10 dB and 29°, respectively. It is correspond to the directivity around 17 dB. It is observed that the simulation results of conical horn antenna are in good agreement which those of the measured results. The measured results of conical horn antenna are summarized in Table 5.2.

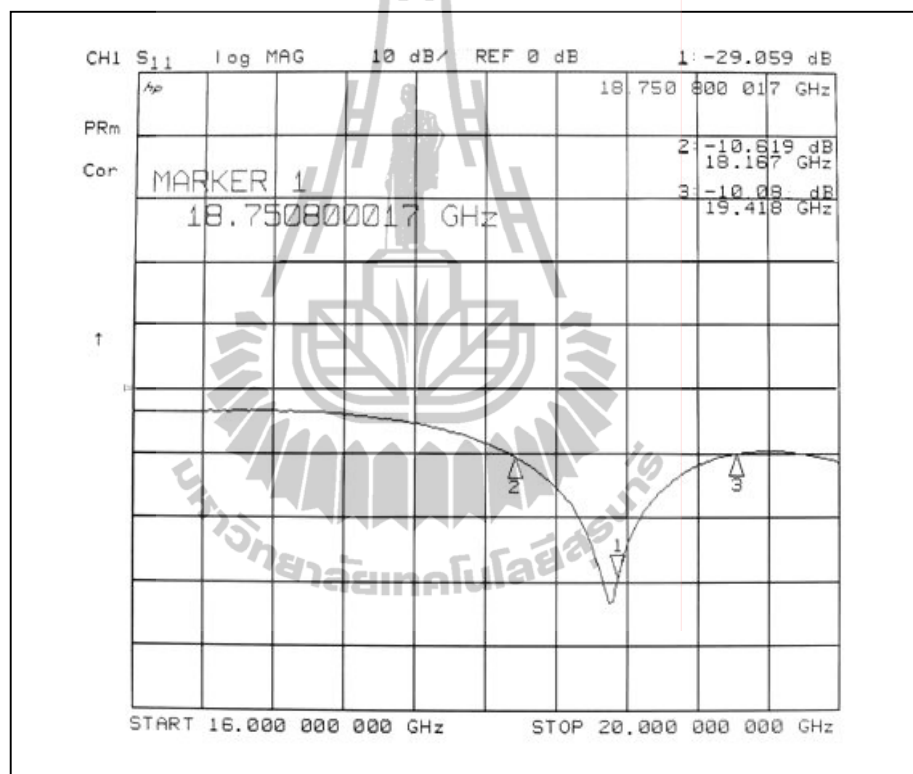


Figure 5.4 Measured return loss for the conical horn antenna.

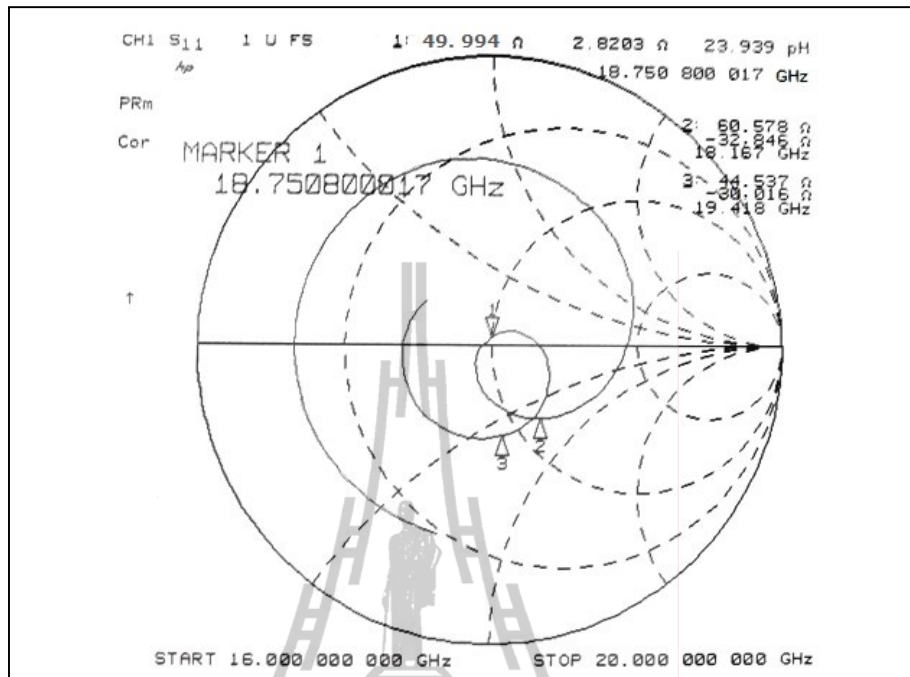


Figure 5.5 Measured impedance for the conical horn antenna.

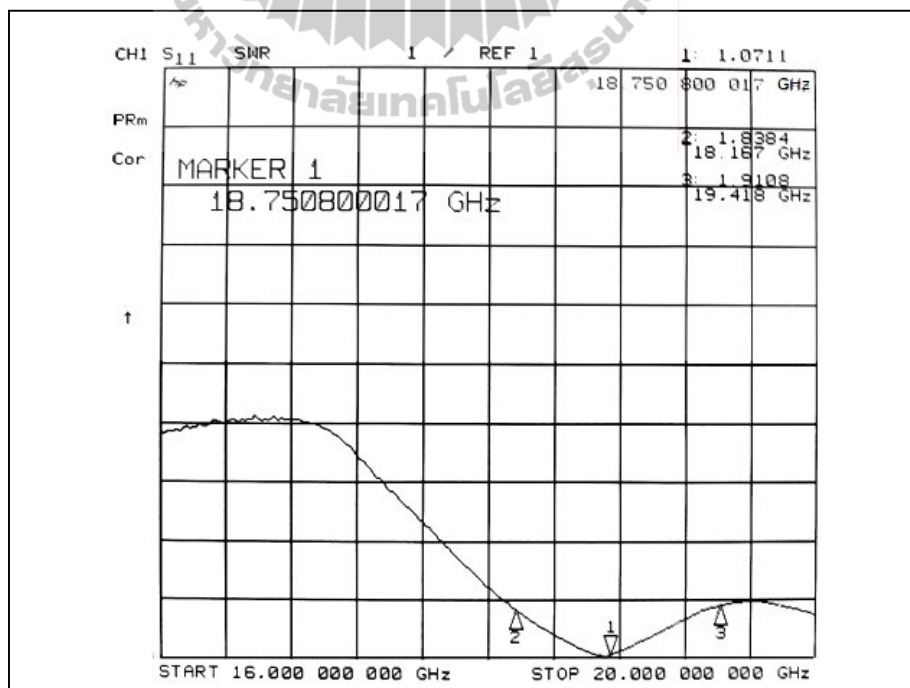


Figure 5.6 Measured standing wave ratio for the conical horn antenna.

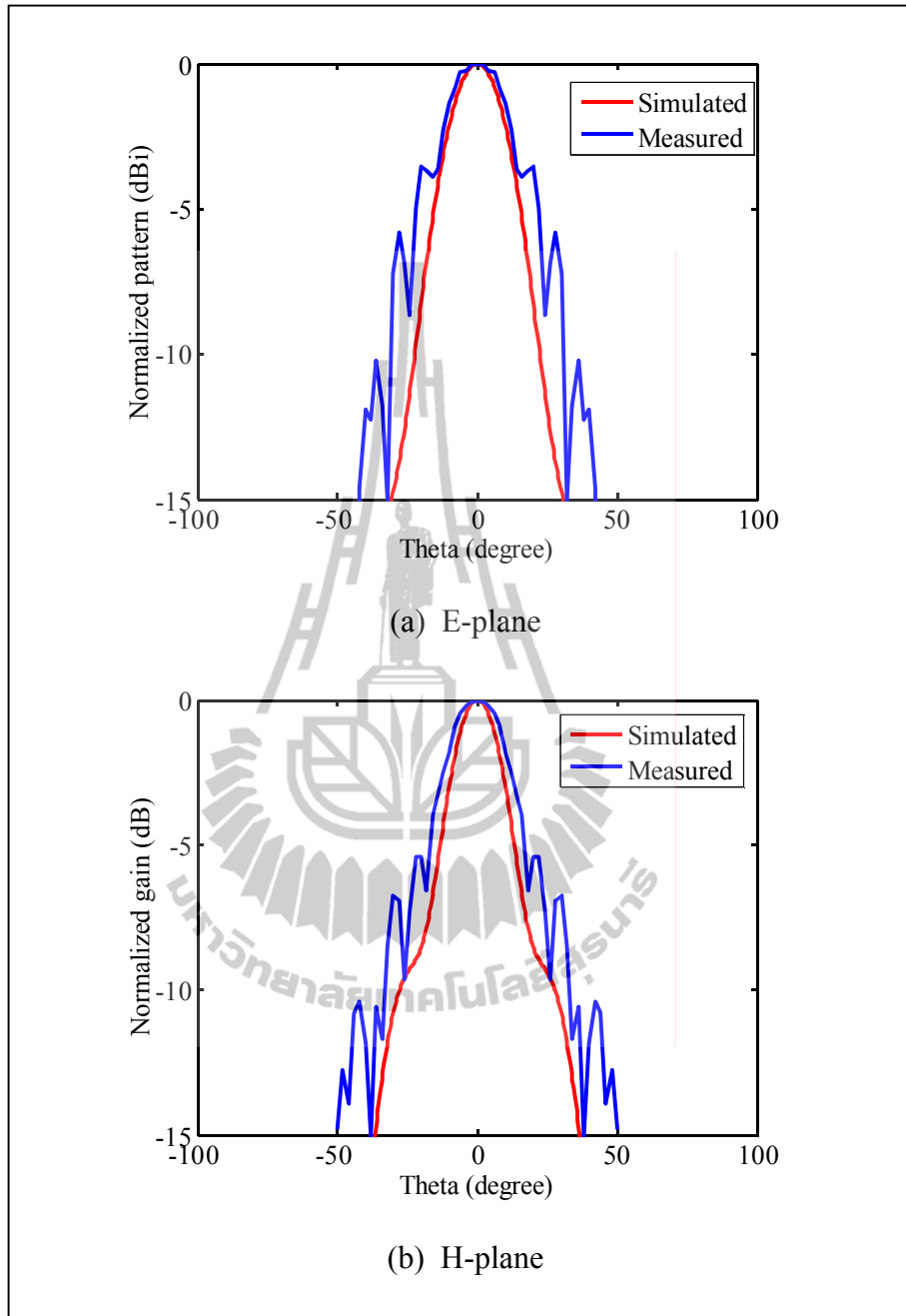


Figure 5.7 Radiation pattern for conical horn antenna.

Table 5.2 Measured characteristics for conical horn antenna.

Characteristics	Measured results
Return loss (S_{11})	-29.059 dB
Input impedance	49.994 Ω
Standing wave ratio (SWR)	1.0711
Gain	11.05 dB
Half power beamwidth (HPBW)	29°

5.4.2 ADE Backscatter Antenna

In order to compare ADE Gaussian backscatter antenna performance, we consider the two cases of the subreflector support structures. The first case, the subreflector is supported from the conical horn using cylindrical stainless steel studs of 2.5 mm diameter as shown in Figure 5.8(a). The second case, the subreflector is supported from the conical horn using cylindrical superlens cavity with a wall thickness of around 1 mm as shown in Figure 5.8(b).

In the first case, the measured results of return loss (S_{11}), input impedance and standing wave ratio (SWR) are shown in Figure 5.9 to 5.11, respectively. It is found that the measured return loss at frequency of 18.75 GHz is -21.346 dB. The measured of impedance is 49.43 Ω . The standing wave ratio is 1.2886. The ADE backscatter antenna can provide impedance bandwidth is about 59 MHz from 18.716 GHz to 18.775 GHz (for $S_{11} < -10$ dB).

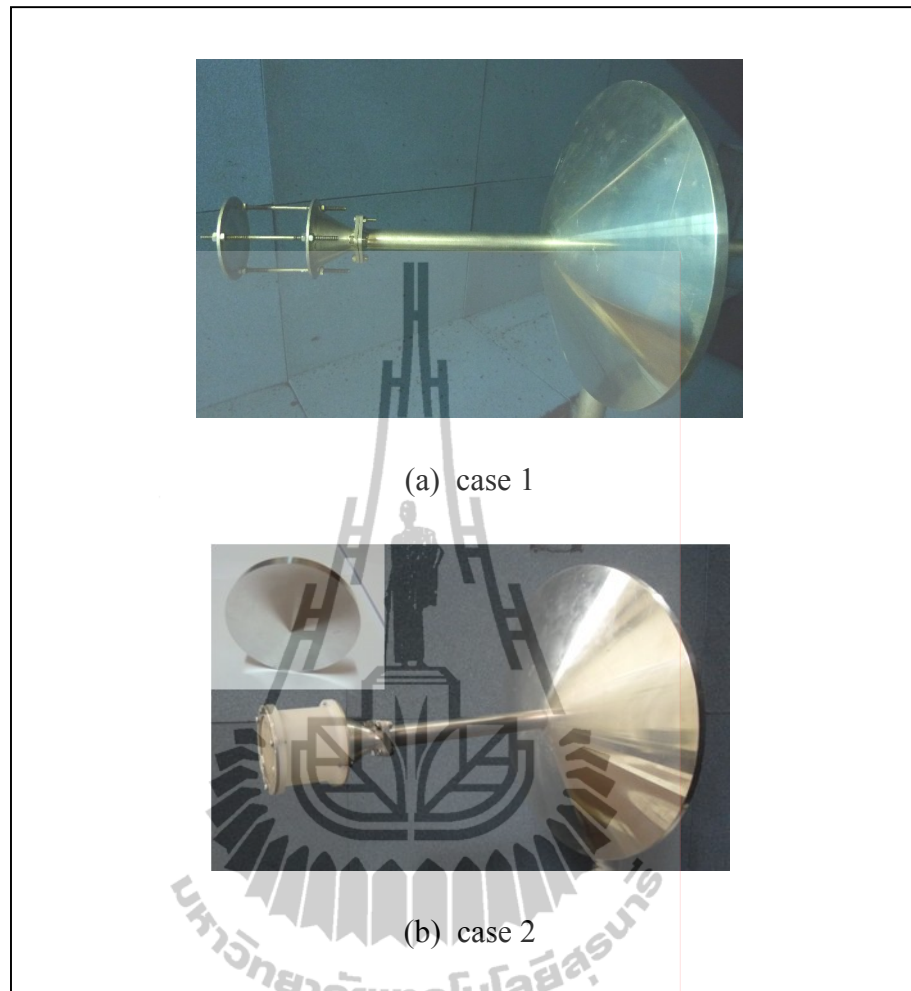


Figure 5.8 Antenna prototype of the realized 30 cm diameter ADE antenna

(a) subreflector is supported from the horn using stainless steel studs

(b) subreflector is supported from the horn using cylindrical superlens cavity.

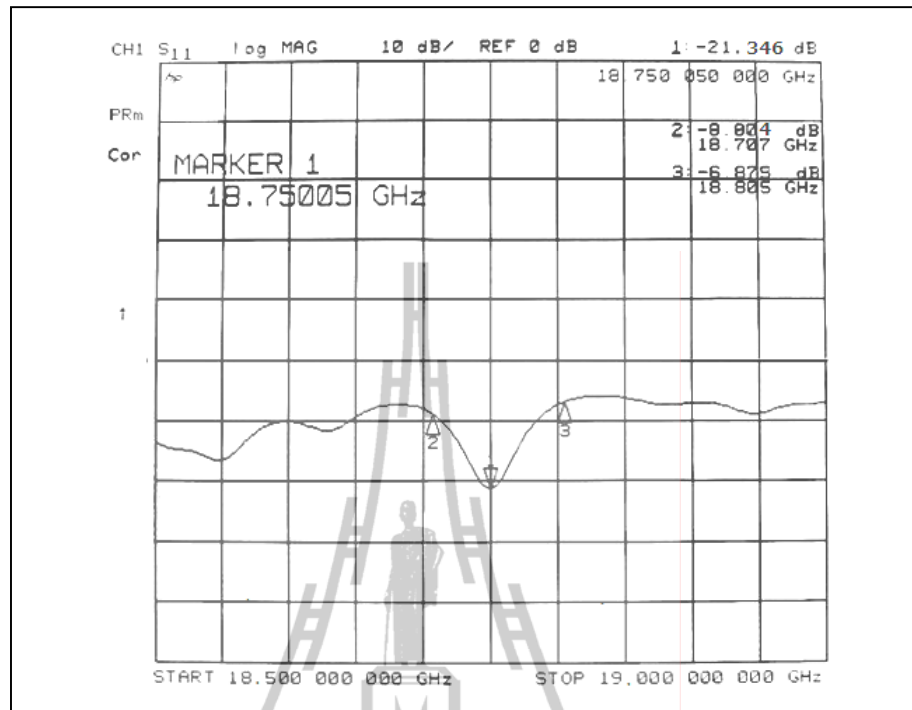


Figure 5.9 Measured return loss for the ADE backscatter antenna (case 1).

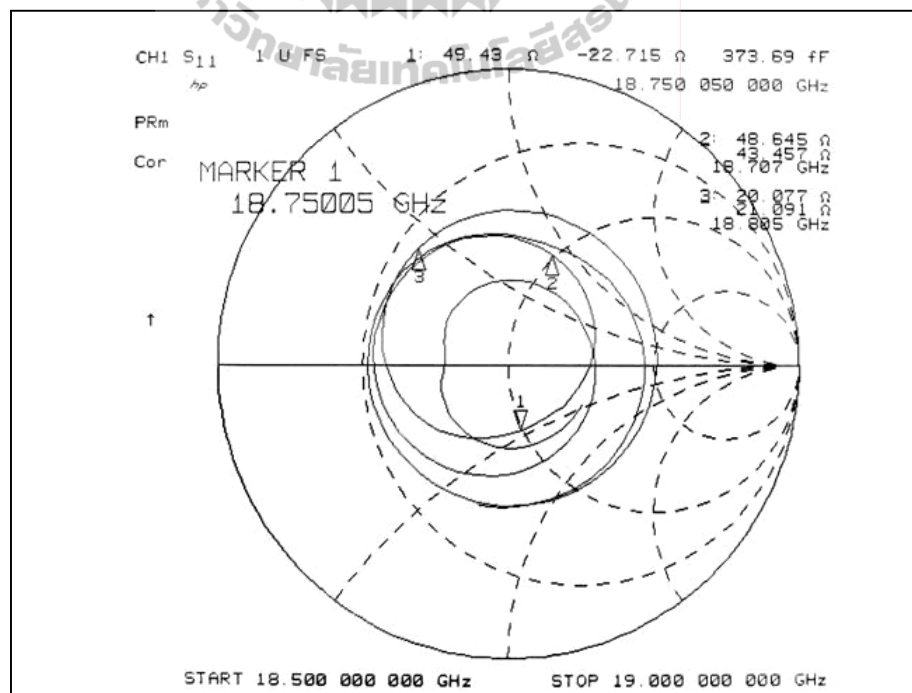


Figure 5.10 Measured impedance for the ADE backscatter antenna (case 1).

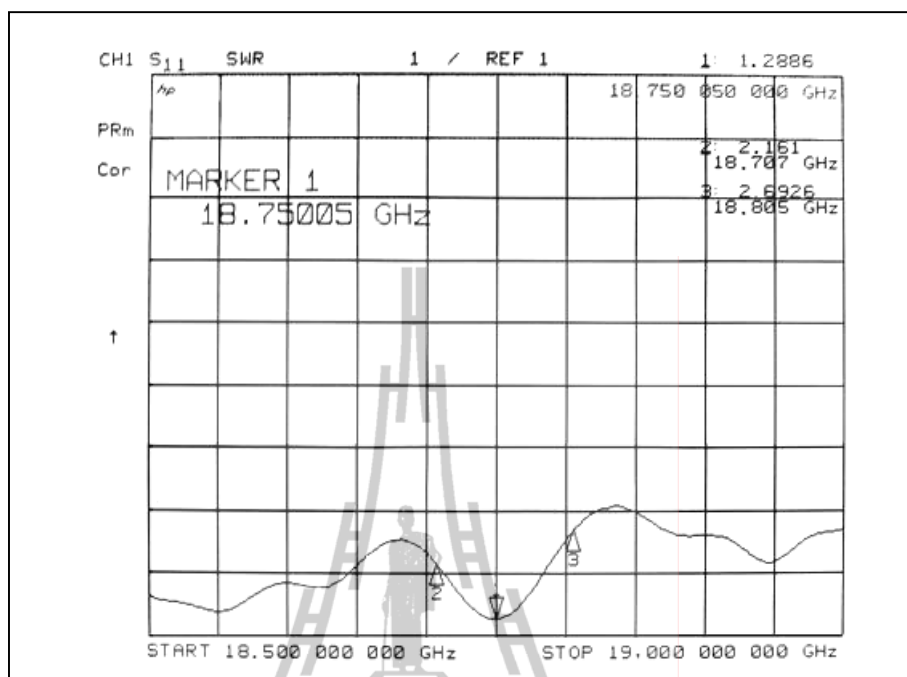


Figure 5.11 Measured SWR for the ADE backscatter antenna (case 1).

The measured radiation pattern of the antenna in the first case is plotted together with the simulated pattern (by using PTD-PTD method) as shown in Figure 5.12. This plot shows agreement between the measured and simulated both in E-plane and H-plane patterns. The measured the gain in E-plane and H-plane are 14.71 dB and 14.21 dB, respectively. The gain at $\theta = \pm 65^\circ$ of the measured result is around 4.20 dB in E-plane and 5.21 dB in H-plane. The measured cross-polarization as shown Figure 5.13 is lower than the co-polarization at $\theta = 0^\circ$ around 18 dB. However, the measured radiation patterns show much ripple. This can be explained by reflections occurring between the cylindrical stainless steel studs and the reflector.

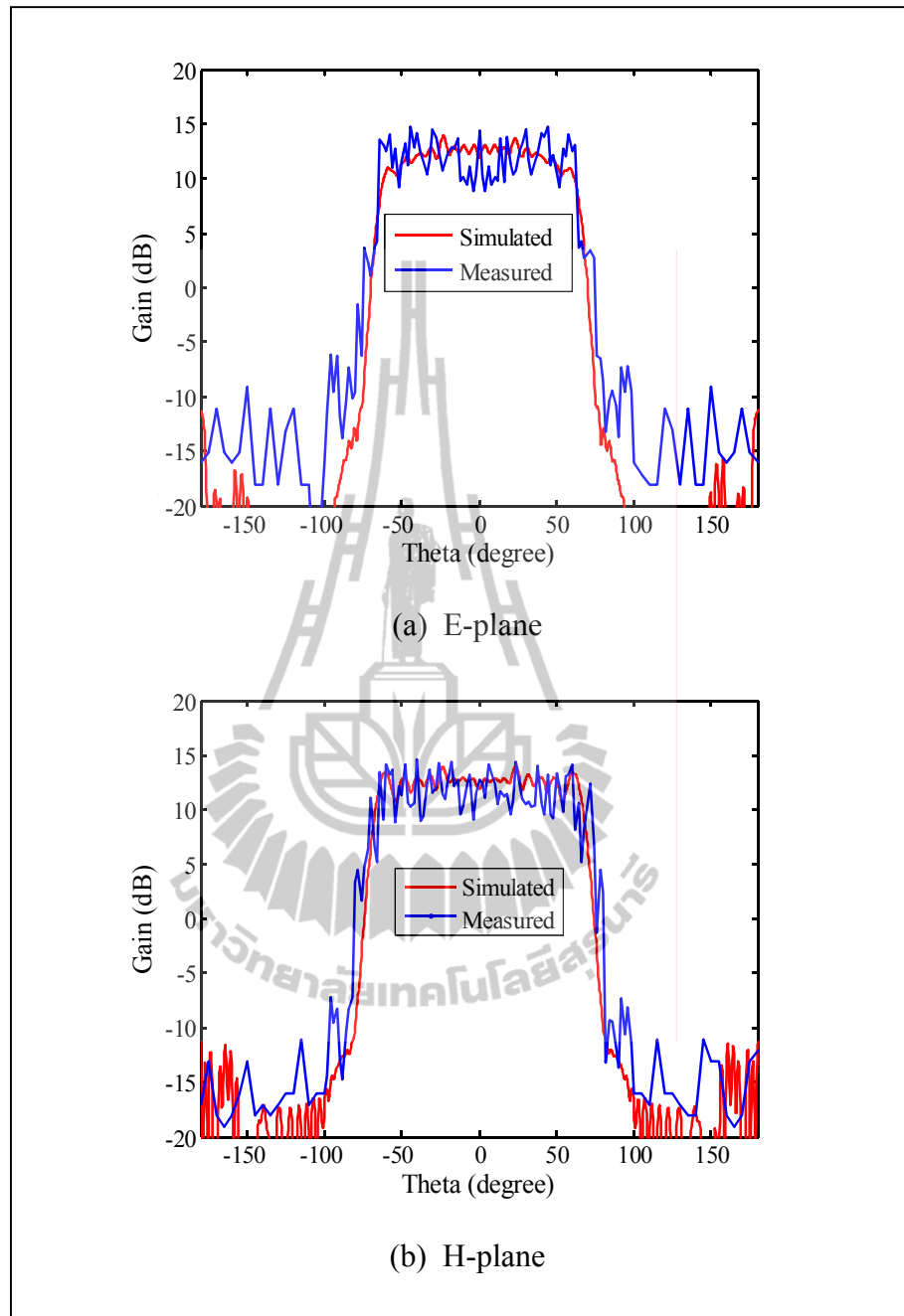


Figure 5.12 Co-polarized field patterns of a ADE backscatter antenna (case 1).

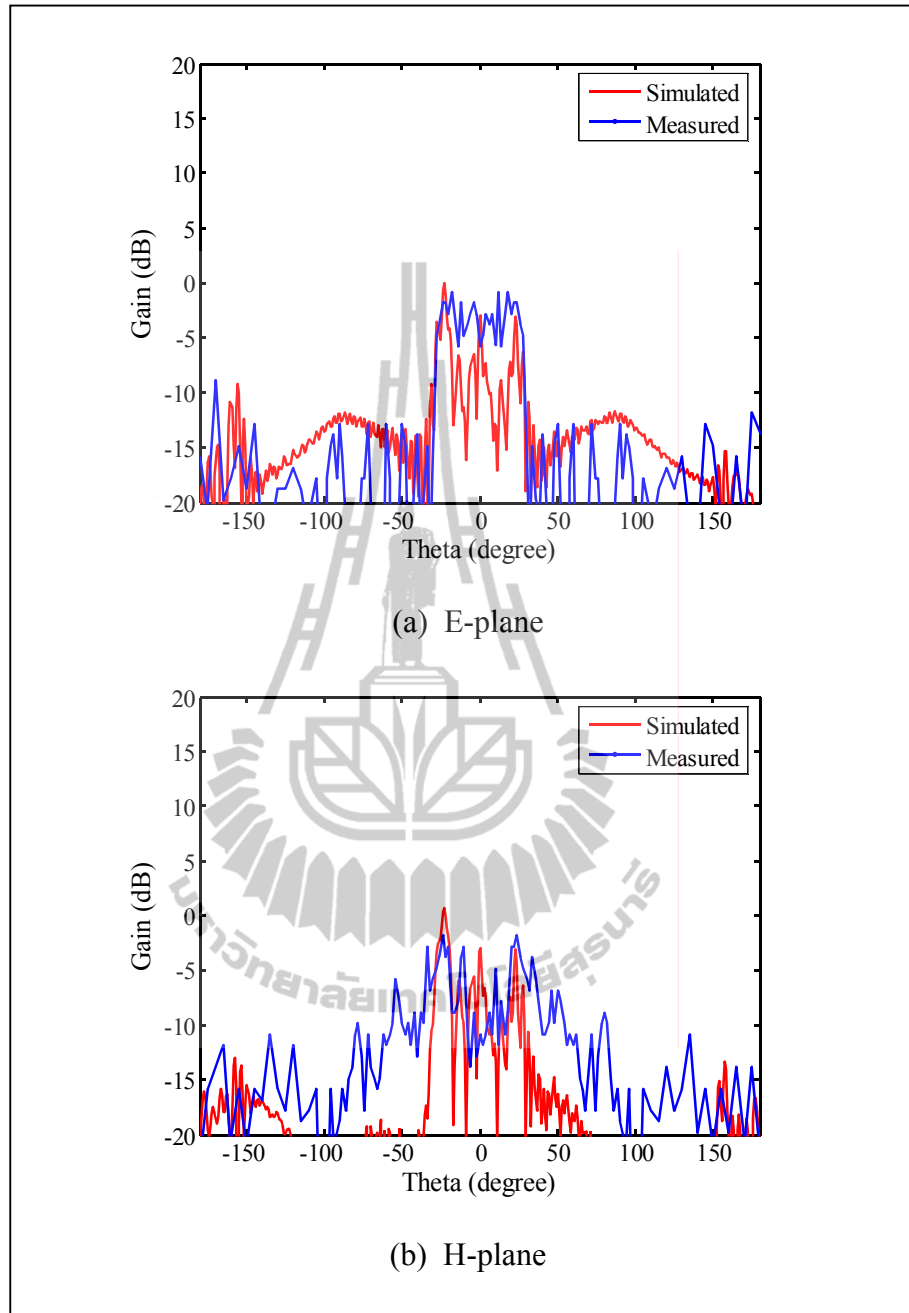


Figure 5.13 Cross-polarized field patterns of a ADE backscatter antenna (case 1).

An alternative method of supporting the subreflector of ADE antenna is the use of a thin-wall dielectric cylinder (the second case) as shown in Figure 5.8(b). The basic problem here is the large variation in incident angles at the cylinder wall for rays reflected from the subreflector. The effect is minimized by using a material with the smallest possible dielectric constant and thickness. Low loss tangent and high mechanical strength are also desirable. Practical considerations lead to the choice of polyamide (nylon-6). This material, popularly called superlene nylon, has a relatively low dielectric constant. The superlene nylon is suitable for this application and can have the small thickness. Figure 5.8(b) shows that the subreflector is supported from the horn using cylindrical superlene cavity with a wall thickness around 1 mm.

In this case, the measured results of return loss (S_{11}), input impedance and standing wave ratio (SWR) are shown in Figure 5.14 to 5.16, respectively. It is found that the measured return loss at frequency of 18.75 GHz is -17.208 dB. The measured of impedance is 44.863Ω . The standing wave ratio is 1.3201. The measured impedance bandwidth is about 51 MHz from 18.707 GHz to 18.758 GHz (for $S_{11} < -10$ dB).

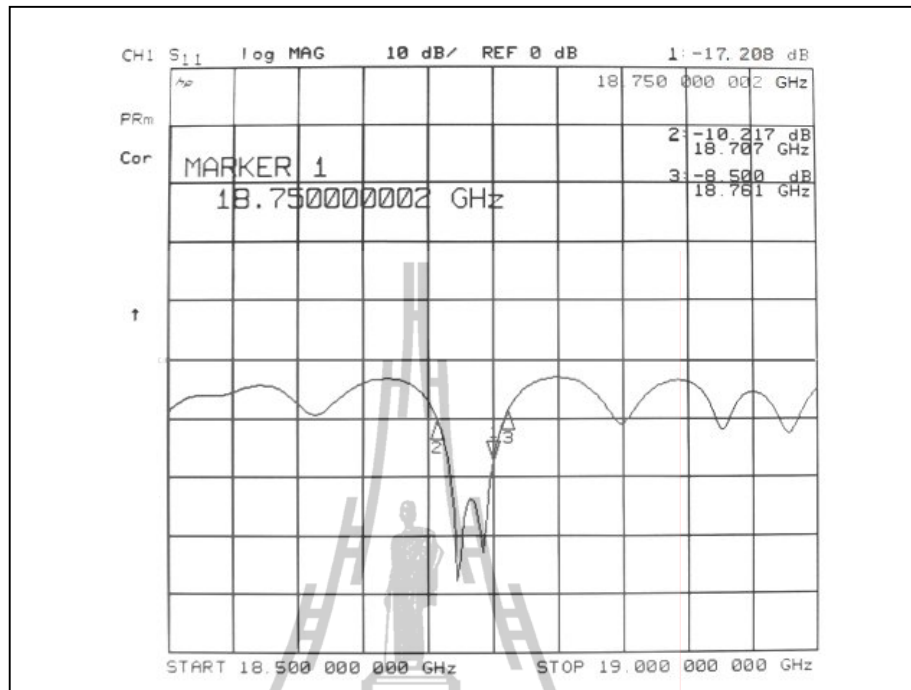


Figure 5.14 Measured return loss for the ADE backscatter antenna (case 2).

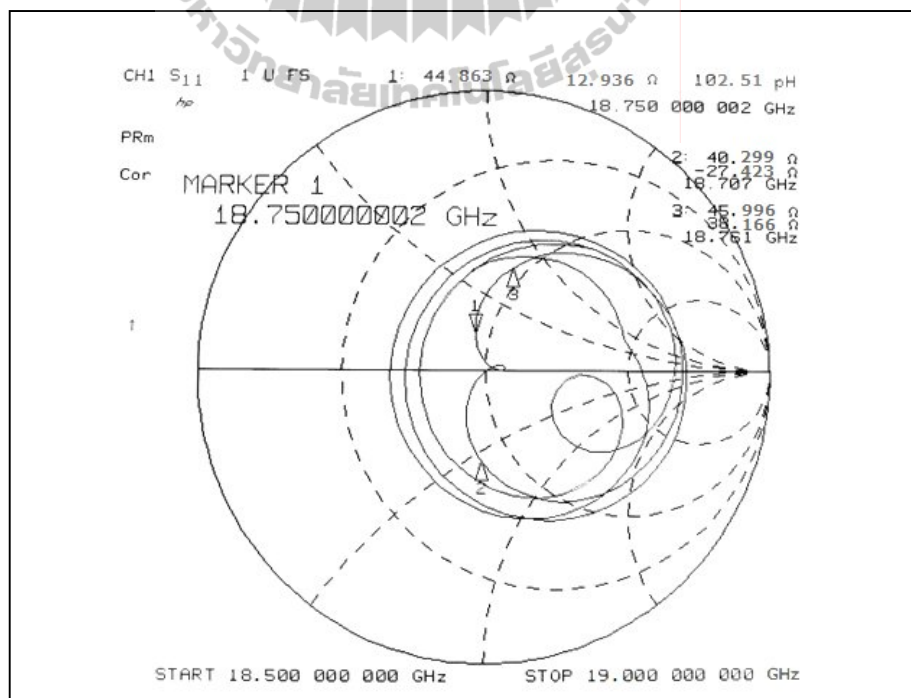


Figure 5.15 Measured impedance for the ADE backscatter antenna (case 2).

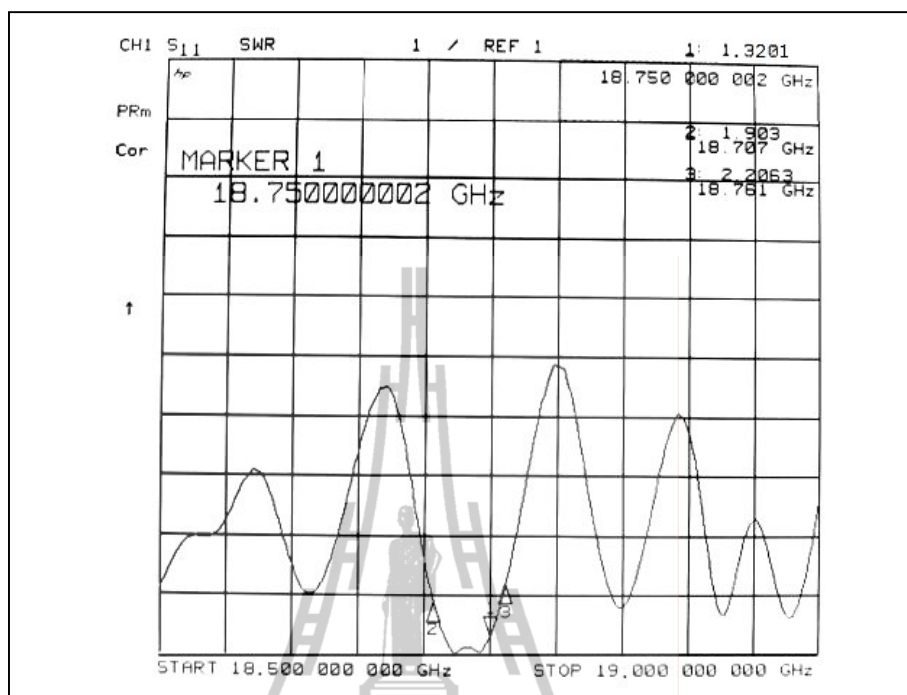


Figure 5.16 Measured SWR for the ADE backscatter antenna (case 2).

The measured radiation pattern of the antenna in this case is plotted together with the simulated pattern as shown in Figure 5.17. This plot shows good agreement between the measured and simulated both in E-plane and H-plane patterns. The measured the gain in E-plane and H-plane are 14.50 dB and 14.32 dB, respectively. The gain at $\theta = \pm 65^\circ$ of the measured result is around 7.62 dB in E-plane and 9.21 dB in H-plane. The measured cross-polarization is lower than the co-polarization at $\theta = 0^\circ$ about 17 dB. From the radiation patterns in Figure 5.12 and Figure 5.17, we can observe that subreflector support structures using metallic studs obviously more impact the electrical performance of the antenna than using thin-wall dielectric cylinder. The use of dielectric materials for this support may give better characteristics of the radiation pattern. The comparison of simulated (without support structure) and measured results are summarized in Table 5.3. An additional cause of

asymmetry observed in the measured patterns in both cases is (the combination of) the small defocusing and mispointing of the feed, i.e., feed displacements and tilts.

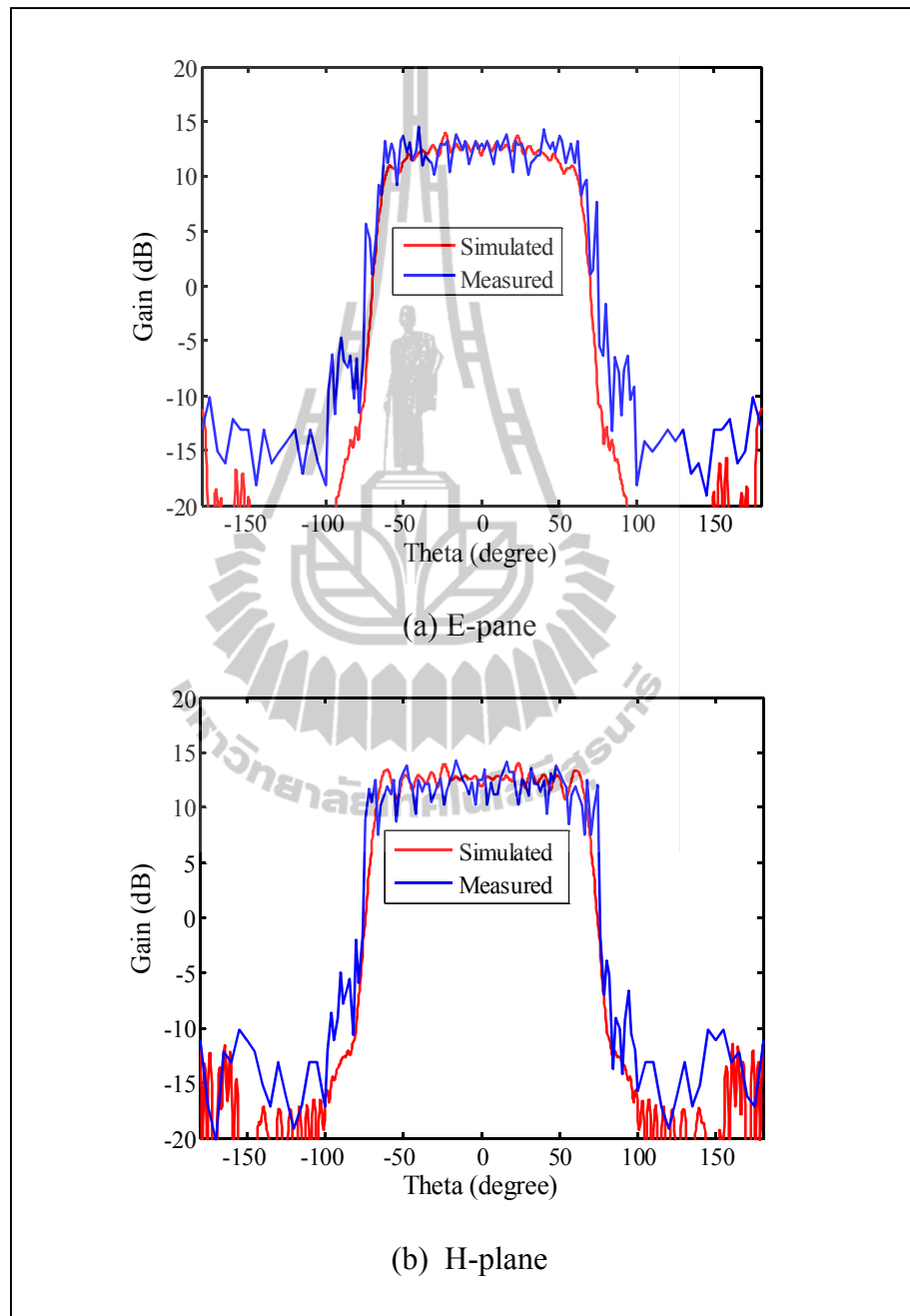


Figure 5.17 Co-polarized field patterns of a ADE backscatter antenna (case 2).

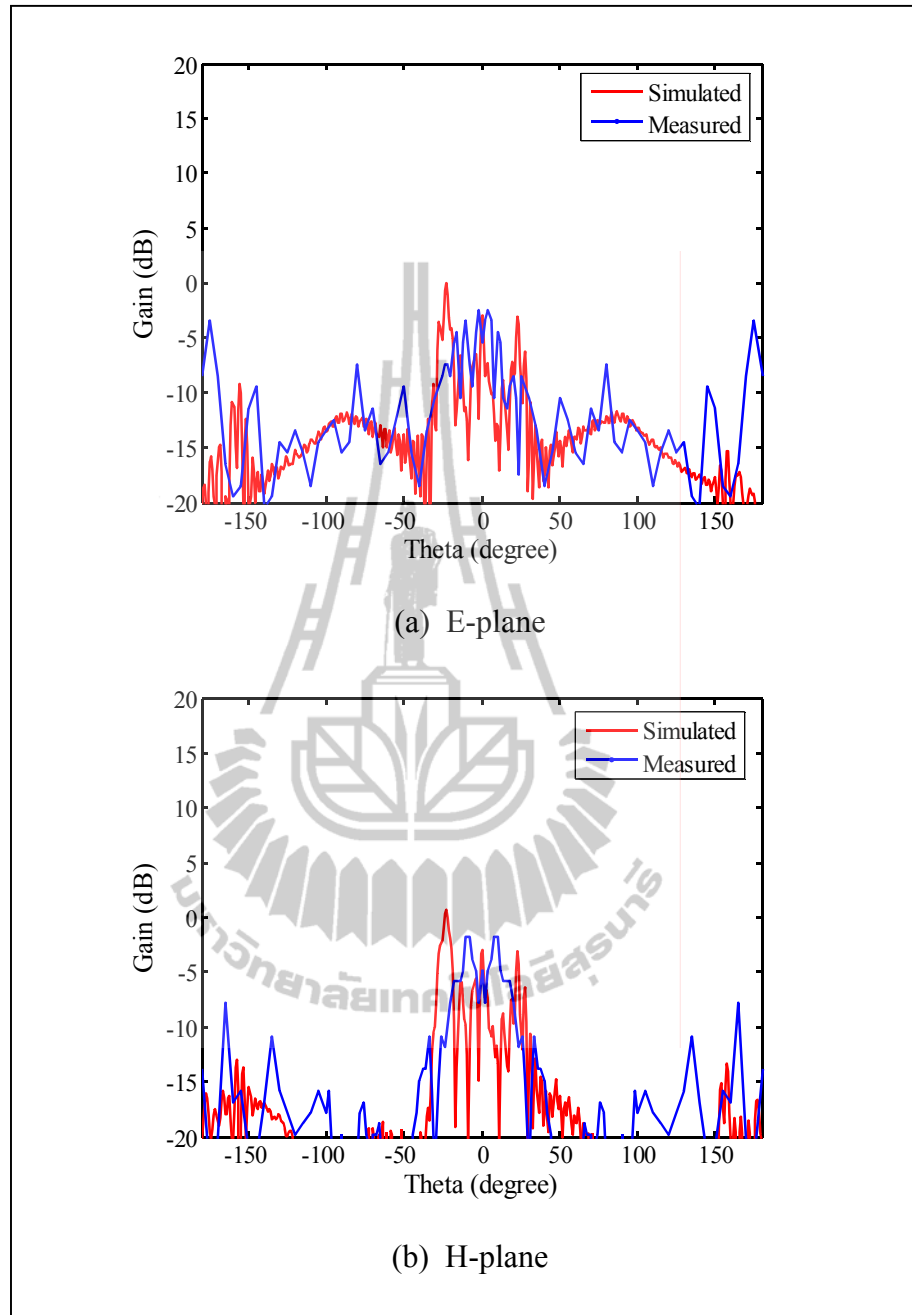


Figure 5.18 Cross-polarized field pattern of a ADE backscatter antenna (case 2).

Table 5.3 Comparison of simulated and measured results for antenna characteristics.

Antenna characteristics	Case 1: Stainless steel studs		Case 2: Cylindrical superlene nylon cavity	
	Simulated	Measured	Simulated	Measured
E-plane				
Maximum Gain (dB)	13.90	14.71	12.90	14.50
Gain at $\theta = \pm 65^\circ$	7.50	4.20	7.50	7.62
H-plane				
Maximum Gain (dB)	13.73	14.21	13.73	14.32
Gain at $\theta = \pm 65^\circ$	11.65	5.21	11.65	9.21

5.5 Chapter Summary

This chapter presents the antenna measurements in order to verify the computed results with measurements to ensure that antenna was correctly modelled in the simulations and correctly assembled. The ADE backscatter antenna prototype with Gaussian main reflector was fabricated by high-precision CNC machine and measured field patterns in anechoic chamber. The subreflector support structures by using metallic studs and thin-wall dielectric cylinder have been considered. The measured maximum gain in the case of using metallic tripod support is 14.71 dB, and the maximum gain at $\theta = \pm 65^\circ$ is around 5.21 dB. The measured maximum gain in the case of using thin-wall dielectric cylinder support is 14.50 dB, and the maximum gain at $\theta = \pm 65^\circ$ is around 9.21 dB. It was found that metallic tripod support obviously impact the electrical performance. The thin-wall dielectric cylinder may give better characteristics of the radiation pattern. Good agreement between simulated and measured results is obtained.

CHAPTER VI

CONCLUSIONS

6.1 Thesis Concluding Remarks

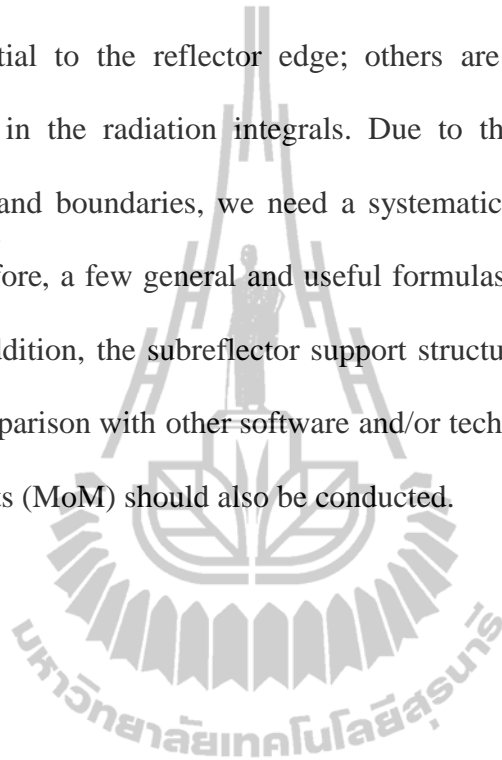
In this thesis, analysis of back feed curved reflector antenna using ring focus feeding has been presented. This antenna can be called the ADE backscatter antenna. The antenna geometry consists of a main reflector by using backscattering technique, portion of an ellipse subreflector and a conical horn antenna. In the designing of ADE backscatter antenna, we need to define parameters to represent antenna geometry with nine parameters. However, these parameters can not be specified arbitrarily. Therefore, we choose five input parameters to define the antenna geometry. Taking into account all of these factors, several sets of input parameters representing various solutions have been considered. In this thesis, we have considered eight sets of input parameters. From these input parameters and using distance relationship in an ellipse, the overall parameters of the antenna are derived in close form. When we have known all the solution of input parameters, the ADE backscatter antenna geometry will be represented. This procedure allows the antenna designer to fully define the antenna geometry with different sets of input parameters, depending on the requirements of the antenna size and performance. For the antenna analysis, physical optics (PO) and physical theory of diffraction (PTD) are used to analytically determine the radiation characteristics of antenna. We have classified the method to analyze the radiation patterns for the subreflector and the main reflector into four cases i.e. using PO on both subreflector and main reflector (PO-PO), using PTD on subreflector and PO on

main reflector (PTD-PO), using PO on subreflector and PTD on main reflector (PO-PTD), and using PTD on both subreflector and main reflector (PTD-PTD). Comparisons each method with the PTD-PTD found that the PO-PO far field envelope in the far angular region was not accurate while PO-PTD solution was most indistinguishable that of the PTD-PTD solution. In the example of the ADE backscatter antenna, the Gaussian equation was chosen to be main reflector. This antenna geometry can provide gain more than 10 dBi and wide beamwidth. To verify the performance of the antenna discussed, the antenna prototype was fabricated with aluminium. The subreflector support structures by using metallic studs and thin-wall dielectric cylinder have been considered. This antenna was tested in an anechoic chamber. The gain measurements were recorded. It was found that metallic tripod support obviously impact the electrical performance. The thin-wall dielectric cylinder may give better characteristics of the radiation pattern. The agreement between simulated and measured results is satisfactory. Based on the results achieved in this thesis, it can be concluded that this ADE backscatter antenna concept is a viable option to meet the demanding customer antenna design requirements of small LEO satellites constellations.

6.2 Remark for Future Studies

Based on the knowledge learned and acquired over this research, some recommendations for future ADE antenna design should be presented. In this thesis, the design examples of ADE backscatter antenna have used Gaussian and quadratic equation to be main reflector. It was found that when we have changed reflector shape, the antenna characteristics are also changed. In the future study, we can change

main reflector for variety shapes in order to provide variety of antenna characteristics. In applying the techniques of PO and PTD to analyze reflector antenna, it is necessary to know several first order derivatives associated with a reflector. Some of the derivatives can be used to construct unit vectors that are normal to the reflector surface or tangential to the reflector edge; others are useful in determining the Jacobians needed in the radiation integrals. Due to the variety in the shapes of reflector surfaces and boundaries, we need a systematical approach to obtain these derivatives. Therefore, a few general and useful formulas in variety geometry should be reviewed. In addition, the subreflector support structure should be considered for simulation. A comparison with other software and/or techniques such as GTD and the method of moments (MoM) should also be conducted.



REFERENCE

- Ahluwalia, D. S., Lewis, R. M., Boersma, J. (1968). Uniform Asymptotic Theory of Diffraction by a Plane Screen. **SIAM J. Appl. Math.** 16: 783-807.
- Ando, M. (1985). Radiation Pattern Analysis of Reflector Antennas. **Electronics and Communications in Japan.** Part 1, 68(4): 93-102.
- Ando, M., and Kinoshita, T., (1989). Accuracy Comparison of PTD and PO for Plane Wave Diffraction from a Large Circular Disk. **The Transactions of the IEICE.** E-72(11): 1212-1218.
- Ando, M. (2005). Radiation Pattern Analysis of Reflector Antenna – Discussions and Hybrid Use of Physical Optics and Aperture Field Integration Method. **IEICE Transaction on Communication.** E88-B(5): 1790-1800.
- Balanis, C. A. (1989). **Advanced Engineering Electromagnetics.** John Wiley & Sons. New York.
- Balanis, C. A. (1997). **Antenna Theory Analysis and Design.** John Wiley & Sons. New York.
- Balanis, C. A. (2005). **Advanced Engineering Electromagnetic (Third edition).** John Wiley & Sons. New York.
- Bergmann, J. R., Hasselmann, F. J. V., and Branco, M. G. C. (2002). MoM Analysis of a Reflector Antenna Design for Omnidirectional Coverage. **Antennas and Propagation Society International Symposium.** 4: 148-151.
- Bergmann, J. R., Hasselmann, F. J. V., Pereira, L. C. P., and Branco, M. G. C. (1998). Reflector Antenna Configurations for Radio Base Stations in Cellular

Communications. **IEEE-APS Conference on Antennas and Propagation for Wireless Communications**. 1-4: 61-64.

Breinbjerg, O., Samii, Y. R., and Hansen, J. A. (1987). Theoretical Examination of the Physical Theory of Diffraction and Related Equivalent Currents. **Tech. Univ. Denmark**, Lyngby, Rep. R339.

Brown, K. W., and Prata, Jr. (1994). A Design Procedure for Classical Offset Dual-Reflector Antennas with Circular Aperture. **IEEE Transactions on Antennas and Propagation**. AP-42(8) : 1145-1153.

Chen, S. L., and Chuang, H. R. (1997). Comparison of the Design of a Contoured-Beam and Elliptical-Beam Satellite Offset Reflector Antennas to Cover the Taiwan Island Region for Satellite Communications. **IEEE Transactions on Broadcasting**. 43(2): 117-126.

Cherrette, A. R., Lee, S. W., and Roberto, J. A. (1989). A Method for Producing a Shaped Contour Radiation Pattern Using a Single Shaped Reflector and a Single Feed. **IEEE Transactions on Antennas and Propagation**. 37(6): 698-705.

Clarricoats, P. J. B., and Olver, A. D. (1984). **Corrugated Horns for Microwave Antennas**, London, UK : Peter Peregrinus.

Collin, R. E., and Zucker, F. J. (1969). **Antenna Theory**, Part I, Chapter 1, McGraw-Hill Book Company, New York.

Duan, D.W., Samii, Y. R., and Mahon, J.P. (1991). Scattering from a Circular Disk: a Comparative Study of PTD and GTD Techniques. **Proceeding of the IEEE**, 79(10): 1472-1480.

- Diaz, L., and Milligan, T. (1996). **Antenna Engineering Using Physical Optics: Practical CAD Techniques and Software.** Boston London Artech House.
- Felsen, L. B., and Marcuvitz, N. (1973). **Radiation and Scattering of Waves.** Prentice-Hall, Englewood Cliffs.
- Galindo, V. (1964). Design of Dual-Reflector Antennas with Arbitrary Phase and Amplitude Distributions. **IEEE Transactions on Antennas and Propagation.** AP-12: 403–408.
- Gennarelli, C., Pelosi, G., and Riccio, G. (1998). Physical Optics Analysis of the Field Backscattered by a Depolarizing Trihedral Corner Reflector. **IEEE Proceedings Microwaves on Antennas and Propagation.** 145: 213-218.
- Granet, C. (1999) A Simple Procedure for the Design of Classical Displaced-Axis Dual-Reflector Antennas Using a Set of Geometric Parameters. **IEEE Antennas and Propagation Magazine.** 41(6): 64-71.
- Griesser, T., and Balanis, C. A. (1985). Backscatter Analysis of Triangular Corner Reflectors Using Geometrical Theory of Diffraction and Physical optics. **IEEE Transactions on Antennas and Propagation.** AP-35(10): 650-660.
- Griesser, T., and Balanis, C. A. (1987). Backscatter Analysis of Dihedral Corner Reflectors Using Physical Optics and Physical Theory of Diffraction. **IEEE Transactions on Antennas and Propagation.** AP-35(10): 1137-1147.
- Hannan, P. W. (1961). Microwave Antennas Derived from the Cassegrain Telescope. **IRE Transactions on Antennas and Propagation.** AP-9:140–153.
- Harrington, R. F. (1961). **Time-Harmonic Electromagnetic Fields.** McGraw-Hill. New York.

- Chen, I. F., Peng, C. M., and Liang, S. C., (2005). Single Layer Printed Monopole Antenna for Dual ISM-Band Operation. **IEEE Transactions on Antennas and Propagation**. 53(2): 1270-1273.
- James G. L., and Kerdelmelidis, V. (1973). Reflector Antenna radiation Pattern Analysis by Equivalent Edge Current. **IEEE Transactions on Antennas and Propagation**. AP-21: 19-24.
- James, J. D., and Hall, P. S. (1989). **Handbook of Microstrip Antenna**. Vol.1. London.
- Keller, J. B. (1957). Diffraction by an Aperture. **J. Opt. Soc. Amer.**, 28: 426-444.
- Keller, J. B. (1962). Geometrical Theory of Diffraction. **J. Opt. Soc. Amer.**, 52(2): 116-130.
- Knott, E. F. (1985). The Relationship between Mitzner's ILDC and Michaeli's Equivalent Currents. **IEEE Transactions on Antennas and Propagation**. AP-33: 112-114.
- Kouyoumjian, R. G., and Pathak, P. H. (1974). A Uniform Geometrical Theory of Diffraction for an Edge in a Perfectly Conducting Surface. **IEEE Proc.**, 63: 1448-1461.
- Kumar, C., Srinivasan, V. V., Lakshmeesha, V. K., and Pal, S. (2009). Performance of an Electrically Small Aperture, Axially Displaced Ellipse Reflector Antenna. **IEEE Antennas and Wireless Propagation Letters**. 8: 903-904.
- Lee, S. W., and Deschamps, G. A. (1976). A uniform Asymptotic Theory of Electromagnetic Diffraction by a Curved Wedge. **IEEE Transactions on Antennas and Propagation**. AP-24(1): 25-34.

- Lorenzo, J. A. M., Pino, A. G., Vega, I., Arias, M., and Rubinos, O. (2005). ICARA: Induced-Current Analysis of Reflector Antennas. **IEEE Antennas and Propagation Magazine.** (47): 92-100.
- Ludwig, A. C. (1973). The Definitions of Cross Polarisation. **IEEE Transactions on Antennas and Propagation.** 21(1): 116-119.
- Michaeli, A. (1984). Equivalent edge currents for arbitrary aspects of observation. **IEEE Transactions on Antennas and Propagation.** 32(31): pp. 252-258.
- Michaeli, A. (1986). Elimination of Infinities in Equivalent Edge Currents, Part I: Fringe Current Components. **IEEE Transactions on Antennas and Propagation.** 34(7): 912-918.
- Michaeli, A. (1984). Elimination of Infinities in Equivalent Edge Currents, Part II: Physical Optics Current Components. **IEEE Transactions on Antennas and Propagation.** AP-34(8): 1034-1037.
- Milligan, T. A. (1985). **Modern Antenna Design.** McGraw-Hill. New York.
- Mitzner, K. M. (1974). Incremental Length Diffraction Coefficients, Aircraft Division Northrop Corp., Tech. Rep. AFAl-TR, pp. 73-296.
- Moreira, F.J.S., and Bergmann, J. R. (2005). Classical Axis-Displaced Dual-Reflector Antennas for Omnidirectional Coverage. **IEEE Transactions on Antennas and Propagation.** 53(9): 2799–2808.
- Moreira, F.J.S., and Prata, A. (2001). Generalized Classical Axially Symmetric Dual-Reflector Antenna. **IEEE Transactions on Antennas and Propagation.** 49(4): 547–554.
- Pontoppidan, K. (2005). **Technical Description of GRASP9,** TICRA, Copenhagen, Denmark.

- Popov, A.P., and Milligan, T. (1997). Amplitude Aperture-Distribution Control in Displaced Axis Two-Reflector Antennas. **IEEE Antennas and Propagation Magazine**, 39(6): 58-63.
- Prata, A., Moreira, F.J.S., and Amaro, L.R. (2003). Displace Axis Ellipse Reflector Antennas for Spacecraft Communications. **Proc. SBMO IEEE MTT-S IMOC.** : 391-395.
- Rotman, W., and Lee, J. C. (1984). Compact Dual Frequency Reflector Antennas for EHF Mobile Satellite Communication Terminals. **Proc. IEEE AP-S International Symposium.** : 771-774.
- Rusch, W. V. T. (1963). Scattering from a Hyperboloidal Reflector in a Cassegrain Feed System. **IEEE Transactions on Antennas and Propagation.** AP-11: 414-421.
- Rusch, W. V. T. (1974). A Comparison of Geometrical and Integral Fields from High-Frequency. Reflectors. **IEEE Transactions on Antennas and Propagation.** 62: 1603-1604.
- Rusch, W. V. T. (1984). The Current State of the Reflector Antenna art, **IEEE Transactions on Antennas and Propagation.** 32 : 313-329
- Rusch, W. V. T., and Potter, P. D. (1970). **Analysis of Reflector Antennas.** Academic Press Inc. New York.
- Samii, Y. R., and Mittra, R. (1977). A Spectral Domain Interpretation of High Frequency Diffraction Phenomena. **IEEE Transactions on Antennas and Propagation.** AP-25: 676-687.

- Samii Y. R. (1984). A Comparison between GO/Aperture-Field and Physical Optics Methods for Offset Reflectors. **IEEE Transactions on Antennas and Propagation**. AP-32: 301-306.
- Samii Y. R. (1993). Reflector Antenna. **Antenna Handbook**. New York. Van Nostrand Reinhold. Vol.2: 1-124.
- Samii Y. R. (1995). A Generalized Diffraction Synthesis Technique for High-Performance Reflector Antennas. **IEEE Transactions on Antennas and Propagation**. 43: 27-40.
- Samii Y. R. (1988). **Reflector Antennas**. In Y. T. Lo and S. W. Lee, editors, **Antenna Handbook**, Chapter 15. Van Nostrand Reinhold Company, New York.
- Samii, Y. R., and Galindo-Israel, V. (1980). Shaped Reflector Antenna Analysis using the Jacobi-Bessel Series. **IEEE Transactions on Antennas and Propagation**. 28(4): 425-435.
- Schorr, M. G., and Beck, Jr. F. J. (1950). Electromagnetic Field of a Conical Horn. **J. Appl. Phys.**, 21 : 795-801
- Scott, C. (1990). **Modern Methods of Reflector Antenna Analysis and Design**. Artech House. Norwood.
- Shogen, K., Nishida, H., and Toyama, N. (1992). Single Shaped Reflector Antennas for Broadcasting satellites. **IEEE Transactions on Antennas and Propagation**. 40(2): 178-187.
- Silva, L. C., Bermann, J. R., and Hasselmann, F. J. V. (2001). Synthesis and Analysis of Microwave Reflector Antennas and Waveguide Feed System- Some Recent Developments. **Microwave and Optoelectronics Conference**. (1): 85-91.

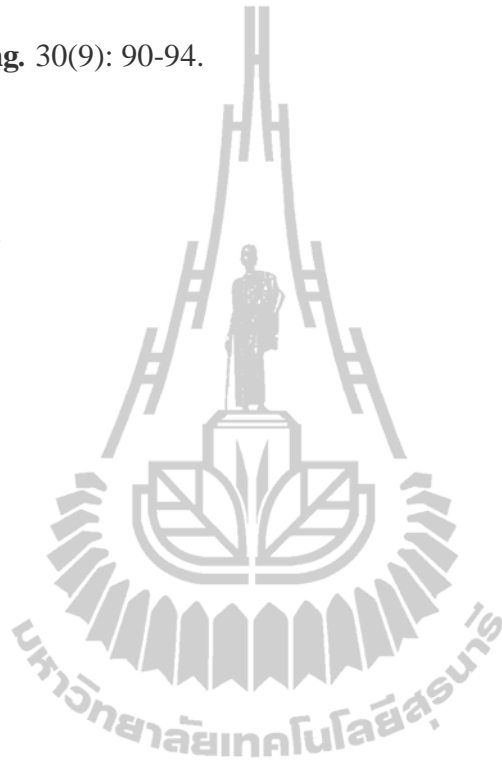
- Silver, S. (1949). **Microwave Antenna Theory and Design**. New York. McGraw-Hill.
- Sim, D. U., and Choi, J. I. (2006). A Compact Wideband Modified Planar Inverted F Antenna (PIFA) for 2.4/5-GHz WLAN Applications. **Antennas and Wireless Propagation Letters**. 5(1): 391-394.
- Smulders, P. F. M., Khusial, S., and Herben, M. H. A. J. (2001). A Shaped Reflector Antenna for 60-GHz Indoor Wireless LAN Access Points. **IEEE Transactions on Vehicular Technology**. 50(2): 584-591.
- Taguchi, M., Egashira, S., and Tanaka, K. (1991). Sleeve Antenna with Ground Wires. **IEEE Transactions on Antennas and Propagation**. 39(1):1-7.
- Thaivirod, V., Krachodnok, P., and Wongsan, R. (2008). Radiation Pattern Synthesis from Various Shaped Reflectors Base on PO and PTD Methods for Point-to-Multipoint Applications. **WSEAS Transactions on Communications**. 1(7): 531-540.
- Thomus, A. M. (1985). **Modern Antenna Design**. McGraw-Hill Book Company, New York.
- Ufimtsev, P. Y. (1962). Method of Edge Waves in the Physical Theory of Diffraction. **Izd-Vo Sovyetskoye Radio**, (Translation prepared by the U.S. Air Force Foreign Technology Division Wright Patterson, AFB, OH, 1971; available from NTIS, Springfield, VA 22161, AD733203): 1-243.
- Viskum, H. H., and Wolf, H. (1993). A Dual Offset Shaped Reflector for Elliptical Beams. **IEEE International Conference on Antennas and Propagation**. 1: 565-569.

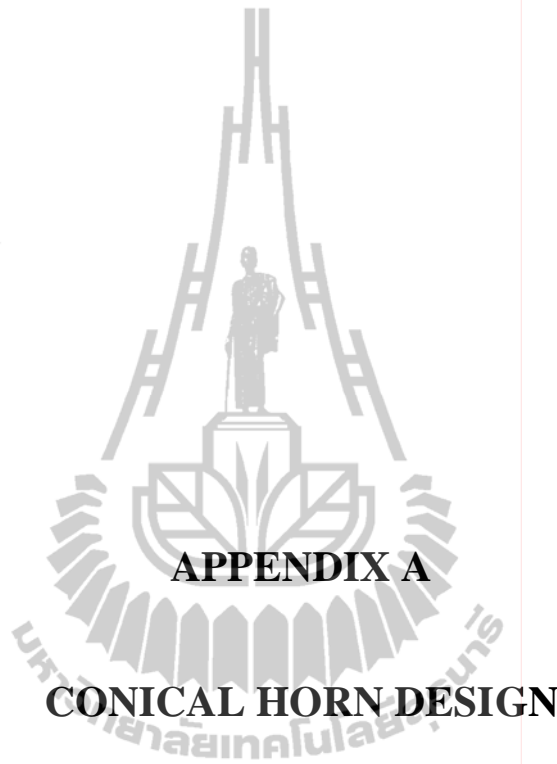
Yerukhimovich, Y. A. (1972). Analysis of Two-Mirror Antennas of General Type.

Telecommunication Radio Engineering. 27(2): 97–103.

Yerukhimovich, Y. A., and Miroshnichenko, A. Y. (1975). Development of double-reflector antennas with a displaced focal axis. **Telecommunication Radio**

Engineering. 30(9): 90-94.





APPENDIX A

CONICAL HORN DESIGN

A.1 The Conical Horn

Another very practical microwave antenna is the conical horn as shown in Figure A.1. The geometry of conical horn antenna consists of circular waveguide and conical horn. The formulations for circular waveguide and conical horn antenna are summarized in Table A.1 and Table A.2, respectively.

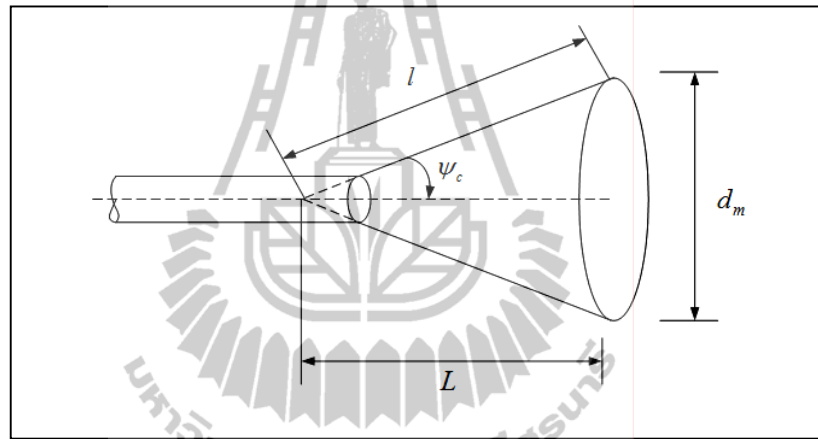


Figure A.1 The conical horn antenna.

Table A.1 Formulations for circular waveguide

Parameters	TE_{11} mode
Free space wavelength	$\lambda_0 = \frac{c}{f}$ where $c = 3 \times 10^8$ m/s, f is operation frequency
Waveguide radius	$a = \frac{\chi'_{mn}}{2\pi} \times \lambda_0$ where $\chi'_{11} = 1.8412$
Cutoff frequency	$(f_c)_{11} = \frac{\chi'_{11}}{2\pi a} \times c$

Table A.1 Formulations for circular waveguide (Continued).

Parameters	TE_{11} mode
Guide wavelength	$(\lambda_g)_{11} = \frac{\lambda_0}{\sqrt{1 - \left(\frac{f_c}{f}\right)^2}}$
Cutoff wavelength	$(\lambda_c)_{11} = \frac{2\pi a}{\chi'_{11}}$

Table A.2 Formulations for conical horn.

Parameters	TE_{11} mode
Directivity	$D_c(dB) = 10 \log \left[\epsilon_{ap} \frac{4\pi}{\lambda^2} (\pi a)^2 \right] = 10 \log \left(\frac{C}{\lambda} \right)^2 - L(s)$
Diameter of horn aperture	$d_m = \frac{10^{\frac{D_c(dB)+L(2)}{20}}}{\pi} \cdot \lambda_0$
Length l	$l = \sqrt{L^2 + \left(\frac{d_m}{2}\right)^2}$, $l = \frac{d_m^2}{3\lambda_0}$
Length L	$L = \sqrt{l^2 - \left(\frac{d_m}{2}\right)^2}$
Angle ψ_c	$\psi_c = \tan^{-1} \left(\frac{d_m}{2L} \right)$ or $\psi_c = \sin^{-1} \left(\frac{d_m}{2l} \right)$

A.1.1 Determination of the Circular Waveguide Dimensions

Waveguide dimensions are function of the frequency which is transmitted into the waveguide. The parameters of circular waveguide can be obtained by

A.1.1.1 Free Space Wavelength (λ_0)

Free space wavelength is described as the wavelength of the wave travels in free space,

$$\lambda_0 = \frac{c}{f}, \quad (\text{A.1})$$

where λ_0 is free space wavelength,

c is light velocity, 3×10^8 m/s,

f is frequency of operation, where the waveguide is designed at 18.75 GHz.

We can obtain free space wavelength as $\lambda_0 = \frac{c}{f} = \frac{3 \times 10^8}{18.75 \times 10^9} = 16$ mm.

A.1.1.2 Inside Radius of the Waveguide (a)

The inside radius of waveguide can be obtained by

$$a = \frac{x'_{mn}}{2\pi} \times \lambda_0. \quad (\text{A.2})$$

The TE_{11} is the dominant mode in a circular waveguide. x'_{mn} is the first several zeros of $J'_n(x)$. The smallest x'_{mn} is $x'_{11} = 1.841$. Hence the inside radius of waveguide for the dominant mode is

$$a = \frac{x'_{mn}}{2\pi} \times \lambda_0 = \frac{1.8412}{2\pi} \times 16 \text{ mm} = 4.6886 \text{ mm.}$$

A.1.1.3 Inside Diameter of the Waveguide (d_{mx})

The inside diameter of the waveguide can be obtained by $2a = 2 \times 4.6886 \text{ mm} = 9.3772 \text{ mm}$. In designing of the waveguide, usually it will depend on the standard dimension of conducting pipe. Hence the dimension for waveguide is designed by using the inside diameter of the waveguide is 11.75 mm, the outside diameter of the waveguide is 18.78 mm, and the thickness of the waveguide is 3.515 mm

A.1.1.4 Cutoff Frequency (f_c)₁₁ for TE_{11} Mode

The cutoff frequency (f_c)₁₁ is defined as the the lowest frequency that the waves can travel in the waveguide. The cutoff frequency is given by

$$\begin{aligned} (f_c)_{11} &= \frac{x'_{11}}{2\pi a} \times c, \\ &= \frac{1.8412}{2\pi \left(\frac{11.75}{2} \times 10^{-3} \right)} \times 3 \times 10^8 = 14.96 \text{ GHz.} \end{aligned} \tag{A.3}$$

A.1.1.5 Guide Wavelength $(\lambda_g)_{11}$

The guide wavelength is defined as the lowest wavelength that can travel in the waveguide. The guide wavelength is determined by

$$\begin{aligned}
 (\lambda_g)_{11} &= \frac{\lambda_0}{\sqrt{1 - \left(\frac{f_c}{f}\right)^2}}, \\
 &= \frac{0.016}{\sqrt{1 - \left(\frac{14.96 \times 10^9}{18.75 \times 10^9}\right)^2}} = 26.55 \text{ mm.}
 \end{aligned}
 \tag{A.4}$$

We have now designed all the parameters necessary to represent the circular waveguide as summarized in Table A.3.

Table A.3 Dimensions of the circular waveguide.

Parameters	Dimension
Free space wavelength (λ_0)	16.00 mm
Cutoff frequency $(f_c)_{11}$	14.96 GHz
Guide wavelength (λ_g)	26.55 mm
The inside diameter of the waveguide	11.75 mm
The outside diameter of the waveguide	18.78 mm
The thickness of the waveguide	3.515 mm

The waveguide can be excited for operating in the TE_{11} mode as shown in Figure A.2. The simplest coax transition extends the center of the coax as a probe as shown in Figure A.3. The end of the waveguide behind the probe ends is a short circuit with the flat plate. The connector is held by two screws and the dielectric extends through the waveguide wall so that the probe starts at the inside wall of the waveguide. In order to transform the impedance of the waveguide to a desired coaxial impedance, usually 50Ω , the variable dimensions in waveguide transition such as probe diameter, probe length and distance to the backshort are adjusted. In addition, the dielectric is inserted onto the probe for impedance matching.

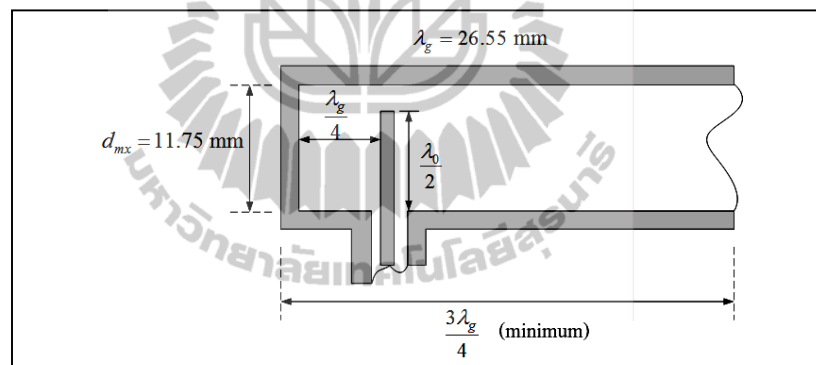


Figure A.2 The exciting of the waveguide for TE_{11} mode.

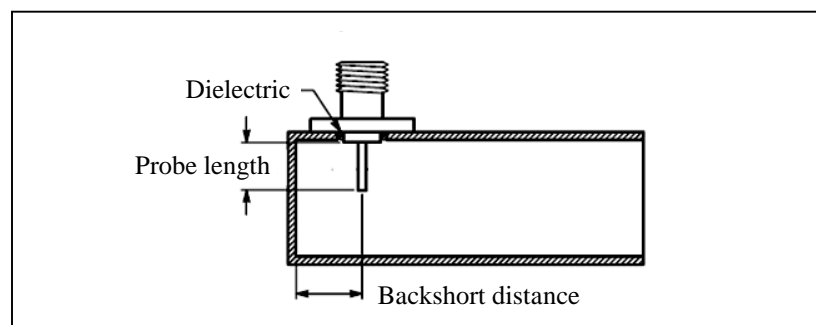


Figure A.3 Coaxial to waveguide transition.

A.1.2 Determination of the Conical Horn Dimensions

In designing the conical horn, we have to know the parameters of the conical horn as shown in Figure A.4.

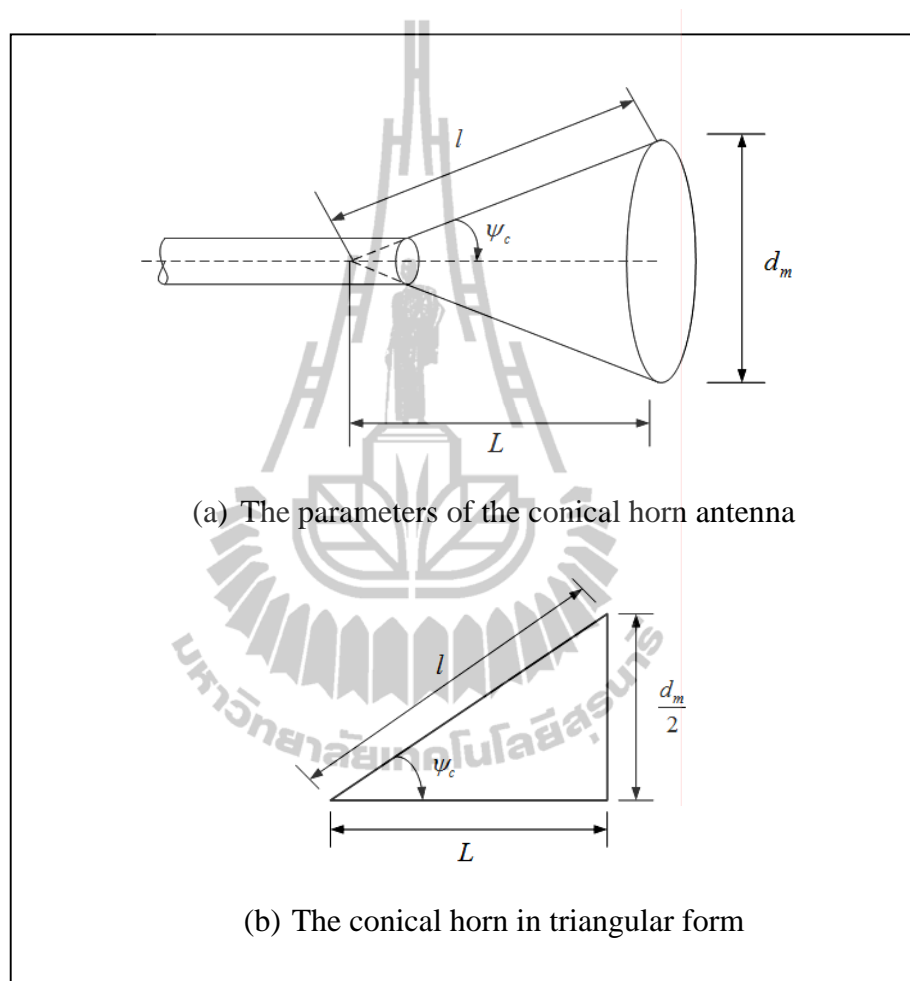


Figure A.4 Conical horn antenna and its parameters.

A.1.2.1 Directivity

The directivity (in decibels) of a conical horn, with an aperture efficiency ε_{ap} and aperture circumference C , can be computed using

$$\begin{aligned}
D_c(dB) &= 10\log_{10} \left[\varepsilon_{ap} \frac{4\pi}{\lambda_0^2} (\pi a)^2 \right] = 10\log_{10} \left(\frac{C}{\lambda_0} \right)^2 - L(s) \\
&= 10\log_{10} \left(\frac{2\pi a}{\lambda_0} \right)^2 - L(s) \\
&= 10\log_{10} \left(\frac{d_m \pi}{\lambda_0} \right)^2 - L(s),
\end{aligned} \tag{A.5}$$

where a is the radius of the horn at the aperture,

d_m is the diameter of the horn at the aperture,

λ_0 is free space wavelength and

$$L(s) = -10\log_{10} \varepsilon_{ap}. \tag{A.6}$$

The first term in (A.5) represents the directivity of a uniform circular aperture while the second term which is represented by (A.6), is a correction figure to account for the loss in directivity due to the aperture efficiency. Usually the term in (A.6) is referred to as the loss figure, which can be computed in decibels using (Balanis, 2005)

$$L(S) \approx (0.8 - 1.71S + 26.25S^2 - 17.79S^3), \tag{A.7}$$

where S is the maximum phase deviation (in number of wavelength), and it is given by

$$S = \frac{d_m^2}{8\lambda l}. \tag{A.8}$$

The gain of a conical horn is optimum when its diameter is equal to

$$d_m \approx \sqrt{3l\lambda_0}, \quad (\text{A.9})$$

which corresponds to a maximum aperture phase deviation of $S = 3/8$ (wavelengths) and a loss figure of about 2.912 dB (or an aperture efficiency of about 51 percent).

Hence the directivity of a conical horn can be obtained by

$$D_c(\text{dB}) = 10 \log \left(\frac{d_m \pi}{\lambda_0} \right)^2 - 2.912. \quad (\text{A.10})$$

A.1.2.2 Diameter of Conical Horn (d_m)

The conical horn antenna is designed at frequency of 18.75 GHz. In designing an optimum directivity conical horn, we have used (A.10), where directivity is defined as 17 dB. The diameter of conical horn for an optimum directivity of 17 dB is determined by

$$\begin{aligned} D_c(\text{dB}) &= 10 \log \left(\frac{d_m \pi}{\lambda_0} \right)^2 - 2.912 \\ 17 &= 10 \log \left(\frac{d_m \pi}{\lambda_0} \right)^2 - 2.912 \\ 19.912 &= 10 \log \left(\frac{d_m \pi}{\lambda_0} \right)^2 \\ d_m^2 &= \frac{97.9941 \lambda_0^2}{\pi^2} \\ d_m &= \sqrt{\frac{97.9941 \lambda_0^2}{\pi^2}} = \sqrt{\frac{97.9941 \times 16 \text{ mm}}{\pi^2}} \\ d_m &= 50.405 \text{ mm.} \end{aligned}$$

A.1.2.3 Length l

The length l can be obtained by

$$l = \frac{d_m^2}{3\lambda_0} = \frac{(50.405 \text{ mm})^2}{3 \times 16 \text{ mm}} = 52.93 \text{ mm.} \quad (\text{A.11})$$

A.1.2.4 Length L

The length L can be obtained by

$$L = \sqrt{l^2 - \left(\frac{d_m}{2}\right)^2} = \sqrt{(52.93)^2 - \left(\frac{50.405}{2}\right)^2} = 46.545 \text{ mm.} \quad (\text{A.12})$$

A.1.2.5 Angle ψ_c

The angle ψ_c can be obtained by

$$\psi_c = \tan^{-1}\left(\frac{d_m}{2L}\right) = \tan^{-1}\left(\frac{50.405 \text{ mm}}{2 \times 46.545 \text{ mm}}\right) = 28.43^\circ. \quad (\text{A.13})$$

A.1.2.6 Length L_x

The length of the waveguide which is inserted into conical horn is shown in Figure A.5. The length L_x can be obtain by using the theory of similar triangle by

$$\frac{L_x}{L} = \frac{\frac{d_{mx}}{2}}{\frac{d_m}{2}} = \frac{l_x}{l}. \quad (\text{A.14})$$

Hence the length L_x is equal to

$$L_x = \frac{\frac{11.75}{2} \text{ mm}}{\frac{50.405}{2} \text{ mm}} \times 46.545 \text{ mm} = 10.85 \text{ mm},$$

and the length l_x is equal to

$$l_x = \sqrt{L_x^2 + \left(\frac{d_{mx}}{2}\right)^2} = \sqrt{(10.85)^2 + \left(\frac{11.75}{2}\right)^2} = 12.339 \text{ mm}.$$

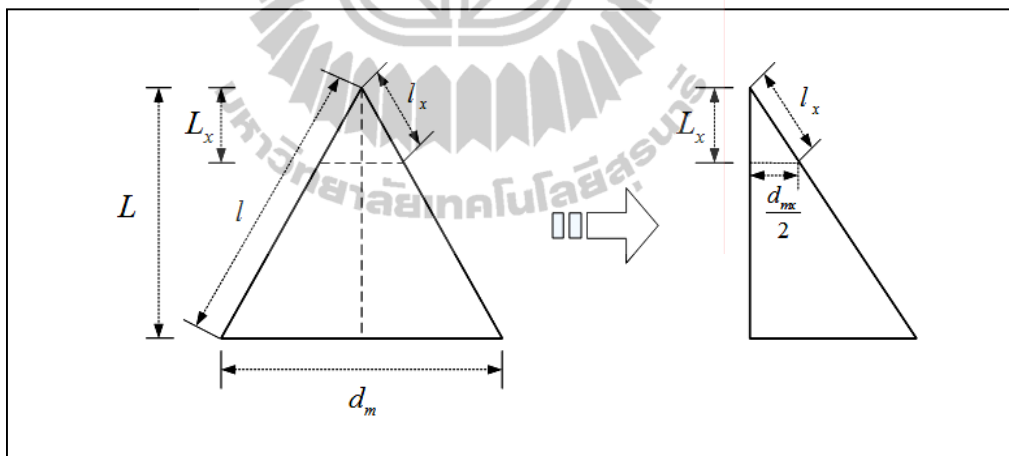


Figure A.5 The length of waveguide which is inserted into conical horn.

We have designed the parameters of conical horn antenna at 18.75 GHz. The parameters necessary to represent conical antenna are summarized in Table A.4.

Table A.4 Dimensions of the conical horn antenna.

Parameters	Dimension
Diameter of conical horn, d_m	50.405 mm
Length l	52.930 mm
Length L	46.545 mm
Angle ψ_c	28.43°
Length L_x	10.850 mm
Length l_x	12.339 mm
Length $\frac{d_{mx}}{2}$	5.875 mm

A.2 Analysis of the Conical Horn: the Aperture Field Method

In order to accurately predict the far field of conical horn, the aperture field method will be described in this section. In the aperture field method, the amplitude of the aperture field of the horn is approximated by that of the TE_{11} mode. In the case of the circular conical horn, the phase distortion is spherical, centered on the single apex of the cone. The equivalent electric and magnetic sources are then constructed from the assumed aperture fields, and aperture integrations are performed to determine the fields radiated by these equivalent sources. These steps are detailed in the following.

For the conical horn, the field components in the aperture plane are approximated by

$$\vec{E}_\rho^a = \frac{k_0 n}{k_{\rho nm} \rho} J_n(k_{\rho nm} \rho) \times (A_p \cos(n\phi) + B_p \sin(n\phi)), \quad (\text{A.15})$$

$$\vec{E}_\phi^a = k_{z nm} J_n'(k_{\rho nm} \rho) \times (B_p \cos(n\phi) - A_p \sin(n\phi)). \quad (\text{A.16})$$

The TE mode currents for a conical horn can be found by using the zero of the derivative of the Bessel function $J_n'(k_{\rho nm} R)$ to find the radial propagation constant,

$$k_{\rho nm} = x'_{nm} / \text{Radius}. \quad (\text{A.17})$$

The equivalent electric and magnetic currents can be constructed by

$$\vec{J}_a(r'_a) = \hat{n} \times \vec{H}^a, \quad \vec{M}_a(r'_a) = -\hat{n} \times \vec{E}^a, \quad (\text{A.18})$$

with $\hat{n} = \hat{z}$ is normal unit vector pointing out along the normal of the aperture and r'_a is position of source point on horn aperture.

The aperture sampling of the conical horn and the aperture electric and magnetic current are shown in Figure A.6. With the assumed sources (A.18), one may construct the radiation integrals for the electric and magnetic fields, which is performed over the horn aperture as

$$\begin{aligned} \vec{E}(\vec{r}) = & \frac{Z_0}{4\pi} \iint_S (\vec{J}_a(r'_a) \left(-\frac{j}{kR} - \frac{1}{k^2 R^2} + \frac{j}{k^3 R^3} \right) \\ & + (\vec{J}_a(r'_a) \cdot \hat{R}) \hat{R} \left(\frac{j}{kR} + \frac{3}{k^2 R^2} - \frac{3j}{k^3 R^3} \right)) e^{-jkR} k^2 ds'_a \\ & - \frac{1}{4\pi} \iint_S \vec{M}_a(r'_a) \times \hat{R} \frac{1}{k^2 R^2} (1 + jkR) e^{-jkR} k^2 ds'_a, \end{aligned} \quad (\text{A.19})$$

$$\begin{aligned}
\bar{H}(\bar{r}) = & \frac{1}{4\pi} \iint_S \bar{J}_a(r'_a) \times \hat{R} \frac{1}{k^2 R^2} (1 + jkR) e^{-jkR} k^2 ds'_a \\
& + \frac{1}{4\pi Z_0} \iint_S (\bar{M}_a(r'_a) \left(-\frac{j}{kR} - \frac{1}{k^2 R^2} + \frac{j}{k^3 R^3} \right) \\
& + (\bar{M}_a(r'_a) \cdot \hat{R}) \hat{R} \left(\frac{j}{kR} + \frac{3}{k^2 R^2} + \frac{j}{k^3 R^3} \right)) e^{-jkR} k^2 ds'_a,
\end{aligned} \tag{A.20}$$

where $R = |\bar{r} - \bar{r}'_a|$ is distance between source points on horn aperture and observation points and $\hat{R} = \frac{\bar{r} - \bar{r}'_a}{|\bar{r} - \bar{r}'_a|}$.

Notice that (A.19) and (A.20) are exact up to the assumptions made in the sources; both near and far field can be computed using these formulas.

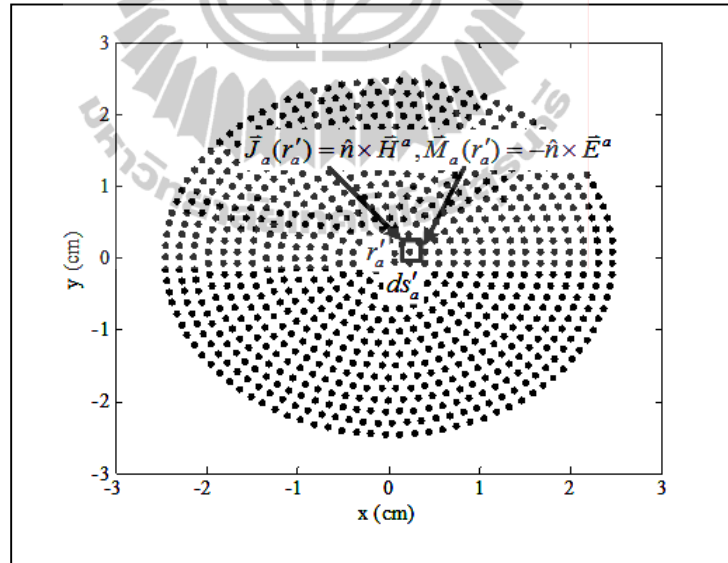


Figure A.6 Aperture sampling of conical horn.

The radiation pattern of conical horn antenna by using aperture field integration method is shown in Figure A.7. It is found that the conical horn can provides directivity about 17.26 dBi.

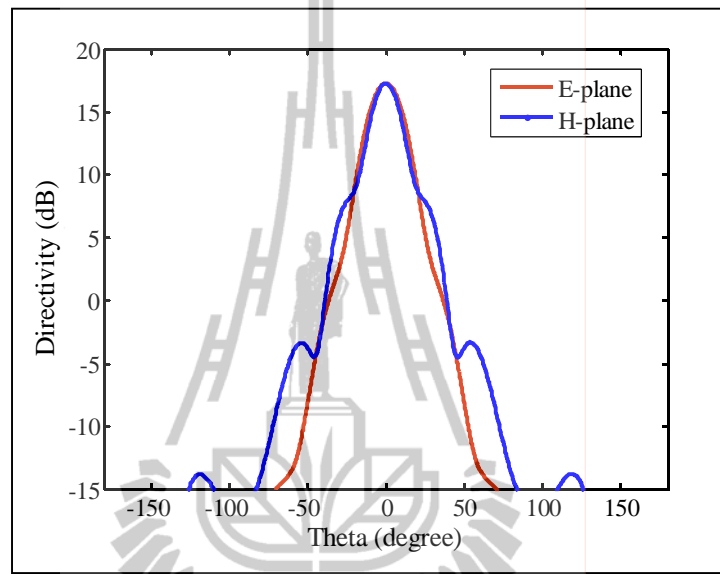


Figure A.7 Radiation pattern of conical horn antenna.



APPENDIX B

LIST OF PUBLICATIONS

International Journal Paper

Thaiviro, V., Krachodnok, P., and Wongsan, R. (2008). **Radiation Pattern Synthesis from Various Shaped Reflectors Base on PO and PTD Methods for Point-to-Multipoint Applications.** WSEAS Transactions on Communications. 7: 531-540.

Thaiviro, W., Wongsan, R., and Krairiksh, M. (2010). **Analysis and Design of a Gaussian Backscatter Antenna with Ring Focus Feed.** Progress in Electromagnetic Research C. 17: 229-244.

International Conference Papers

Thaiviro, V., and Wongsan, R. (2007). **Diffraction Analysis of a Quadratic Backscatter Reflector Antenna using Physical Optics and Physical Theory of Diffraction.** The 2007 International Symposium on Antennas and Propagation. 1: 197-200.

Thaiviro, V., and Wongsan, R. (2007). **Analysis and Experimental Verification of a Quadratic-Shaped Reflector Antenna.** 2007 Asia-Pacific Microwave Conference. 1: 1999-2002.

Thaiviro, V., Krachodnok, P., and Wongsan, R. (2008). **The Numerical and Experimental Study of Radiation Pattern from Various Shaped Reflectors Base on PO and PTD Method.** 7th WSEAS International Conference on Applied Computer and Applied Computational Science. 1: 54-59.

- Thaiwirot, V., and Wongsan, R. (2008). **Performance Improvement of Broad-Beam Quadratic Reflector Antenna**. The Fifth International Conference in Electrical Engineering/Electronics, Computer, Telecommunications and Information Technology. 1: 301-304.
- Thaiwirot, W., Wongsan, R., and Krairiksh, M. (2009). **A Simple Procedure for the Design of Quadratic Backscatter Antenna with Ring Focus Feed**. Proceedings of Thailand-Japan Joint Symposium on Microwave 2009. 1: 95-98.
- Thaiwirot, W., Wongsan, R., and Krairiksh, M. (2009). **Design of a Quadratic Backscatter Antenna with Ring Focus Feed**. The 2009 International Symposium on Antennas and Propagation (ISAP2009). 1: 815-818.
- Thaiwirot, W., Wongsan, R., and Krairiksh, M. (2010). **Design of a Gaussian Backscatter Antenna with Ring Focus Feed**. Proceeding of Progress in Electromagnetics Research Symposium. 1: 836-839.
- Thaiwirot, W., Wongsan, R., and Krairiksh, M. (2010). **A Quadratic Backscatter Antenna with Ring Focus Feed**. The 2010 International Symposium on Antennas and Propagation. 1: 860-863.
- Wongsan, R., Thaiwirot, W., and Krairiksh, M. (2010). **Performance Improvement of a Gaussian Backscatter Antenna with Ring Focus Feed**. The 2010 International Symposium on Antennas and Propagation. 1: 864-867.

BIOGRAPHY

Miss Wanwisa Thaiwirot was born on May 7th, 1982 in Burirum Province, Thailand. She graduated with the Bachelor Degree of Engineering in Telecommunication Engineering (First Class Honor) in 2004 from Suranaree University of Technology, Nakhon Ratchasima Province, Thailand. She then attended Suranaree University of Technology and received a Master's Degree in Telecommunication Engineering in 2007. After that she received scholarship from the Office of the Higher Education Commission under the program Strategic Scholarships for Frontier Research Network for the Joint Ph.D program in Telecommunication Engineering, School of Telecommunication Engineering, Institute of Engineering at Suranaree University of Technology. She worked for her research at Ando and Hirokawa Laboratory, Tokyo Institute of Technology, Japan for five months. Her research interests include the electromagnetic wave applications and antenna engineering.